Karlsruhe Institute of Technology

Institut für Theoretische Festkörperphysik

On the Physical Significance of Strong Spatial Dispersion

Zur Erlangung des akademischen Grades eines

DOKTORS DER NATURWISSENSCHAFTEN

(Dr. rer. nat)

von der KIT-Fakultät für Physik

des Karlsruher Instituts für Technologie (KIT)

angenommene Dissertation

von

M.Sc. Ramakrishna Venkitakrishnan

am Institut für Theoretische Festkörperphysik

Datum der mündlichen Prüfung:	12.05.2023
Referent:	Prof. Dr. C. Rockstuhl
Korreferent:	Prof. Dr. M. Plum

Erklärung zur Selbstständigkeit

Ich versichere, dass ich diese Arbeit selbstständig verfasst habe und keine anderen als die angegebenen Quellen und Hilfsmittel benutzt habe, die wörtlich oder inhaltlich übernommenen Stellen als solche kenntlich gemacht und die Satzung des KIT zur Sicherung guter wissenschaftlicher Praxis in der gültigen Fassung vom 24.05.2018 beachtet habe.

Karlsruhe, den 12.05.2023, _____

M.Sc. Ramakrishna Venkitakrishnan

Als Prüfungsexemplar genehmigt von

Karlsruhe, den 12.05.2023, _____

Prof. Dr. C. Rockstuhl

Thesis abstract

Optical metamaterials consist of subwavelength inclusions that possess unconventional optical properties that are unavailable in natural materials. The specific shape, composition, and arrangement of these inclusions determine the optical response of the metamaterials. However, designing them for specific applications with traditional simulations and experimental tests is impractical due to their high degree of complexity. To address this, the effective medium theory provides an efficient approach by linking the actual metamaterial to a homogeneous material with specific constitutive relations, allowing it to interact with light in the same manner.

Local material laws have been frequently used to model metamaterials as a homogeneous medium, assuming that the electromagnetic response at a point depends solely on the fields at that point. However, the accuracy of these models depends on the characteristic length scale of the metamaterial, which is the ratio between the lattice period and the operational wavelength. When this ratio is not much smaller than one, as is the case with optical metamaterials, spatial nonlocality becomes dominant, and the electromagnetic response of a point is influenced by the fields at many other points within the material. As a result, traditional local material laws cannot accurately describe the behavior of optical metamaterials. To address this challenge, we propose a new approach for modeling the behavior of optical metamaterials using nonlocal material laws. Specifically, we use a Taylor expansion in the Fourier space to approximate a general and exact nonlocal response function of the electric field, allowing us to derive a set of effective material parameters. Our approach accurately captures the spatial nonlocality of optical metamaterials and can be used to design novel and unique optical properties for various applications.

In this thesis, firstly, we present two nonlocal models that account for significant spatial dispersion effects and analyze the dispersion behavior of eigenmodes in homogenized

metamaterials. We then derive the interface conditions that facilitate the calculation of reflection and transmission coefficients for a homogeneous slab with an incident field.

Secondly, to conduct the actual homogenization of a MM, we discuss two methods. The first approach treats the metamaterial as a bulk material and utilizes computational parameter retrieval techniques to assign effective material parameters to the bulk. This technique employs a least-square fitting algorithm to determine the optimal values for the effective material parameters by comparing the reflection and transmission coefficients of the bulk with those of the actual metamaterial. Further, we use this method to study three artificial structures with predetermined scattering properties that are quantified in terms of multipole moments they sustain and reveal that the effective permittivity and permeability are linked to the electric and magnetic dipole moments of the scatterers. Additionally, nonlocal material parameters are related to higher-order multipolar moments and their interaction with dipolar terms. By understanding the significance of each material parameter, we can decide the truncation order for the Taylor expansion of the considered constitutive relations for a given metamaterial.

We also investigate the role of the period-to-operational wavelength ratio in homogenizing a metamaterial, specifically an electric dipolar lattice. Surprisingly, we observe a breakdown in homogenization at shorter lattice constants due to near-field interactions among the particles forming the lattice. This suggests that the period should not only be much smaller than the operational wavelength to homogenize a metamaterial but there exists an optimal period for a given inclusion size.

The second method introduced in this thesis is a novel homogenization approach using the "effective transition matrix" or $\mathbf{T}_{\text{eff}}$-matrix, which provides an exact description of the linear interaction between light and the bulk material without the need for any computational retrieval processes. By homogenizing an isotropic 3D metamaterial made of gold nanospheres, we detail the calculation of the corresponding effective material parameters and further obtain the reflection and transmission coefficient for the homogeneous material. The highlight of this approach is the promise to homogenize a 3D metamaterial without requiring a target object as opposed to the case of any parameter retrieval methods.

Finally, we summarize all the analytical and numerical results and discuss possible future research endeavors as an extension of the results obtained in the thesis. Overall, the thesis

contributes to a deeper understanding of the behavior of optical metamaterials at the effective level and offers valuable insights for future research in this field.

Contents

List of Figures xi

List of Tables xiv

1. Introduction 1

1.1. Metamaterials 1

1.2. Effective Medium Theory (EMT) 4

1.3. Structure of the Thesis 11

2. Theoretical Background 13

2.1. Linear Constitutive Relation: Phenomenological Approach 14

2.2. General Response Function and Spatial Dispersion 16

2.3. Derivation of the Special Curl-Based Constitutive Relation 18

2.3.1. Functional Space Definition of the Response Function 19

2.3.2. Introduction to Tensors 25

2.3.3. Series Expansion of Response Function in Tensor Space 26

2.3.4. Tensor Contraction 29

2.3.4.1. Anti-Symmetric Tensors: Exterior Algebra and Hodge Star Decomposition 29

2.3.4.2. Symmetric Tensors: Symmetric Algebra and Symmetric Tensor Decomposition 33

3. Dispersion Relation and Interface Condition 41

3.1. Centrosymmetric Metamaterial 42

3.1.1. Disperion Relation 43

3.1.2. Interface Conditions 46

3.2. Chiral Metamaterial 51
3.2.1. Condon-Tellegen Constitutive Relation 52
3.2.2. Disperion Relation 54
3.2.3. Interface Conditions 54
3.3. Fresnel Equations 55

4. Results and Discussion **57**
4.1. Computational Setup and Simulation 57
4.1.1. Parameter Retrieval Method 58
4.1.2. Numerical Experiment Using the T-Matrix Method 62
4.2. Investigation of Non-Local Isotropic Metamaterials 64
4.2.1. Pure Electric Dipolar Scatterer 66
4.2.2. Pure Electric Quadrupolar Scatterer 69
4.2.3. Spherical Scatterer with a Combination of Multipoles 73
4.2.4. Determining the Lower Limit of Homogenization Methods. 79
4.3. Effective Transition Matrix: $\mathbf{T}_{\text{eff}}$- matrix 85
4.3.1. Gold Spheres in a Cubic Lattice 90

5. Summary **95**

Appendix **99**
A. Expressing Levi-Civita in Terms of the Rotation Matrix 99
B. Centrosymmetric Metamaterial 101
B.1. Energy Flux Associated with the SSD Models: Poynting Vector Formulation 101
B.2. Fresnel Expressions: Calculating Reflection and Transmission Coefficients 104
C. Chiral Metamaterial 108
C.1. Derivation of the General Interface Condition 108
C.2. Field Modelings 112
C.3. Fresnel Expressions: Calculating Reflection and Transmission Coefficients 114
D. Deriving Effective Material Parameters from $\mathbf{T}_{\text{eff}}$-matrix 119

E. Analysis on the Impact of the Number of Multipoles N on the Accuracy of $\mathbf{T}_{\text{eff}}$ 121

Bibliography **123**

Acknowledgement **143**

List of Figures

1.1. Pictorial representation of the homogenization 4

2.1. Distributional function - Bump function and its first three derivatives . . . 20
2.2. Pictorial representation of the Hodge star operator $(*)$ 29

3.1. Isofrequency curves for an isotropic medium using WSD, SSD-γ, and SSD-τ models 45
3.2. Visualizing interfaces between a metamaterial slab and its surrounding medium. 49

4.1. Flow chart optimizing a Maxwell solver for a homogenization model 59
4.2. Pictorial representation of non-local homogenization concept 66
4.3. Polarizability and error function for electric dipole metamaterials. 67
4.4. Effective material parameters for electric dipole metamaterials 68
4.5. Polarizability and error function for electric quadrupole metamaterials . . . 70
4.6. Effective material parameters for electric quadrupole scatterer 71
4.7. Impact of the electric quadrupole on the material parameter τ. 72
4.8. Polarizability and error function for a metamaterial composed of combined multipolar moments. 73
4.9. Effective material parameters for a metamaterial composed of combined multipolar moments. 75
4.10. Absolute reflection coefficient predicted for a metamaterial composed of combined multipolar moments. 76
4.11. Absolute optical coefficient variation with incidence angle for a metamaterial composed of combined multipolar moments. 78
4.12. Absolute optical coefficient variation with lattice constant for electric dipole metamaterial 80

4.13. Effective material parameters in WSD model for electric dipole metamaterials varying with lattice constant 81
4.14. Absolute reflection coefficient at three angles using full wave calculation. . . 82
4.15. Error function for electric dipole metamaterial varying with lattice constant. 83
4.16. Sum of error functions for electric dipole metamaterial. 84
4.17. Homogenization of gold nanosphere metamaterial using $\mathbf{T}_{\text{eff}}$ method. 91
4.18. Reconstructing a spherical lattice from a homogeneous slab 92

A.1. Action of rotation matrix on a cartesian coordinate system 99
B.2. Half space problem: Interface between two media 104
C.3. Half space problem: Interface between chiral - achiral mediums. 109
C.4. Pictorial representation of the spherical polar coordinate system 113
C.5. Interface between chiral and achiral media with incident circularly polarized plane wave 115
E.6. Impact of multipole count on $\mathbf{T}_{\text{eff}}$ accuracy. 121

List of Tables

4.1. The lists of relevant material parameters 61

Publications

Peer-reviewed journal articles

Publications presented within this thesis are highlighted in bold letters.

[1] **Venkitakrishnan, R., Augenstein, Y., Zerulla, B., Goffi, F. Z., Plum, M., & Rockstuhl, C. (2023). On the physical significance of non-local material parameters in optical metamaterials. New Journal of Physics, 25(12), 123014.**

[2] **Zerulla, B*., Venkitakrishnan, R*., Beutel, D*., Krstić, M., Holzer, C., Rockstuhl, C., & Fernandez-Corbaton, I. (2022). AT-Matrix Based Approach to Homogenize Artificial Materials. Advanced Optical Materials, 11, 2201564.**

[3] **Venkitakrishnan, R., Höß, T., Repän, T., Goffi, F. Z., Plum, M., & Rockstuhl, C. (2021). Lower limits for the homogenization of periodic metamaterials made from electric dipolar scatterers. Physical Review B, 103(19), 195425.**

[4] Repän, T., Venkitakrishnan, R., & Rockstuhl, C. (2021). Artificial neural networks used to retrieve effective properties of metamaterials. Optics Express, 29(22), 36072-36085.

[5] Goffi, F. Z., Khrabustovskyi, A., Venkitakrishnan, R., Rockstuhl, C., & Plum, M. (2021). Higher order constitutive relations and interface conditions for metamaterials with strong spatial dispersion. Physics Letters A, 412, 127570.

Journal articles under preparation

[1] **Venkitakrishnan, R., Goffi, F. Z., Plum, M., & Rockstuhl, C. (2023). Tensorial Derivation of Constitutive Relations for Strongly Dispersive Metamaterials. Unpublished manuscript [Manuscript Under Preparation].**

*denotes an equal contribution by the authors

*denotes an equal contribution by the authors

Conference contributions

Conference presentations by myself are highlighted in bold letters.

[1] Goffi, F. Z., Venkitakrishnan, R., Rockstuhl, C., & Plum, M. (2023, February 5 -10). Homogenization of strongly dispersive materials [Oral presentation]. Women in Nonlinear Dispersive PDEs, BIRS, Banff, Canada

[2] Zerulla, B., Venkitakrishnan, R., Beutel, D., Krstić, M., Holzer, C., Rockstuhl, C., & Fernandez-Corbaton, I. (2022, Septermber 12-17). A T-matrix Based Approach to Homogenize Materials and Metamaterials [Oral presentation]. The sixteenth international congress on artificial materials for novel wave phenomena-Metamaterials, Siena, Italy

[3] **Venkitakrishnan, R., Zerulla, B., Goffi, F. Z., Plum, M., & Rockstuhl, C. (2022, Septermber 12-17). On the physical significance of non-local material parameters [Poster presentation]. The sixteenth international congress on artificial materials for novel wave phenomena-Metamaterials, Siena, Italy**

[4] Goffi, F. Z., Venkitakrishnan, R., Rockstuhl, C., & Plum, M. (2022, June 5-9). Nonlocal material parameters describing metamaterials at the effective level [Oral presentation]. ECCOMAS Congress, Oslo, Norway

[5] Augenstein, Y., T., Repän, Venkitakrishnan, R., Kuhn,L., Garcia-Santiago, X., & Rockstuhl, C., (2021, November 1-3). Solving Inverse Problems in the Field of Computational Nanophotonics [Invited talk], IEEE COMCAS, Tel Aviv, Israel

[6] **Venkitakrishnan, R., Höß, T., Repän, T., Goffi, F. Z., Plum, M., & Rockstuhl, C. (2021, September 20-25). Lower limits for the homogenization of periodic metamaterials [Oral presentation]. The fifteenth international congress on artificial materials for novel wave phenomena-Metamaterials, Virtual Conference**

[7] Goffi, F. Z., Khrabustovskyi, A., Venkitakrishnan, R., Rockstuhl, C., & Plum, M. (2021, September 20-25). Higher order constitutive relations and interface conditions for metamaterials with strong spatial dispersion [Oral presentation]. The fourteenth international congress on artificial materials for novel wave phenomena- Metamaterials, Virtual Conference

1. Introduction

1.1. Metamaterials

The introduction of artificial materials, or metamaterials (MM), into the field of optics aims to attain unconventional properties that are not present in natural materials. Initially, this pertains to non-traditional properties of light propagation, but strictly speaking, it refers to non-conventional material properties. Generally, metamaterials consist of a dense arrangement of meta-atoms, which serve as the basic building block. The average electromagnetic response of a MM, in its lowest-order approximation, is derived from the optical response of these individual meta-atoms. Thus, research efforts in the context of MM involve the careful design of these meta-atoms to control and predictively manipulate electric and magnetic fields. Several design strategies have enabled the use of MM to achieve groundbreaking applications at optical frequencies. These include non-linear optics, graphene-based applications, perfect lenses, digital metamaterials, and coding metamaterials, among others [1–12].

The exciting properties in a MM often emerge from the resonant behavior of the structural organization of the meta-atom and their arrangement. The interplay of the shape of the inclusion (e.g., a sub-wavelength unit cell), the composition of the constituent materials, and the periodicity of the meta-atom arrangement [13–16] are a few parameters worth mentioning. Unlike natural materials, which mostly lack magnetic properties at optical frequencies (with a relative magnetic permeability term $\mu(\omega) = 1$), metamaterials offer a frequency-dependent effective permeability, $\mu(\omega)$, determined by a non-vanishing magnetic susceptibility $\chi_m(\omega) = \mu(\omega) - 1$. Advances in fabrication technologies have made it increasingly possible to achieve sophisticated and complex optical designs at nanoscales. This, combined with the ability to respond to both electric and magnetic fields of light at optical frequencies, has enabled metamaterials to achieve groundbreaking applications.

To point out some of the major applications, the introduction of the perfect lens by Victor Veselago in 1968 [1] enabled the development of flat optics and miniaturized lenses, which have been a priority for centuries. The perfect lens offered improved optical performance and the ability to miniaturize conventional curved lenses. Veselago's seminal work revealed that the medium has dramatically different light propagation characteristics, stemming from the negative phase velocity absent in conventional materials. Special design strategies such as the metallic wire medium, the split-ring resonator, and chiral metamaterials have further led to surprising effects like the reversal of both the Doppler shift and Cherenkov radiation, and anomalous refraction [3, 5, 16–18]. In addition to these exotic examples, MM designs have allowed general-purpose applications like the perfect absorber in solar cell devices and found use in light sail systems, controlled holography, and other applications [8, 19–36].

In addition to having a specific design for the meta-atoms, the consequence of connecting them in a lattice creates a complex optical response that is otherwise not accessible by the scattering response of a single nanoparticle [37]. Typically, to simplify the theoretical analysis and characterization of metamaterials, it is preferred to arrange the meta-atoms periodically [38–41]. The reason is that in a periodic arrangement of meta-atoms, the collective response of the entire lattice can be tuned and extracted, rather than just the response of a single meta-atom in the far field. The periodicity of a metamaterial lattice, as in the case of an array made from all-dielectric nano-particles, usually dictates the wavelength at which resonance takes place. Additionally, by controlling the spacing of the meta-atoms within a fixed volume of the metamaterial, it is possible to tune the interaction among the meta-atoms. This leads to a complex interference of multiple scattering modes among the particles, which can give rise to new physics and effects in the metamaterial. [42, 43]. To put it differently, periodicity provides an extra level of flexibility to manipulate the electric and magnetic response of the metamaterial to external fields. [44–46].

At this point, we come to the idea of using a dimensionless quantity called the characteristic length defined as $\frac{\Lambda}{\lambda}$, the ratio between the periodicity Λ and the operating wavelength λ of the incoming wave. This ratio describes to which extent the propagating wave experiences the periodicity. Therefore, at a given wavelength, the choice of periodicity highly influences the far-field response of the considered MM. Exemplarily is the case of photonic crystals that support, if suitably designed, a photonic stop band. For frequencies inside this stop

band, the waves are exponentially decaying (*evanescent*), which requires a period close to half the wavelength, $\frac{\Lambda}{\lambda} \approx \frac{1}{2}$ [47].

To this end, intentionally linking the geometrical aspects of a system with the optical degrees of freedom has become a principal goal of contemporary photonics research. For many high-frequency optical applications, it is imperative that $\frac{\Lambda}{\lambda} < 1$ is essential owing to the requirement for subwavelength design. The recent development of three-dimensional LASER printing techniques has enabled the fabrication of sub-micrometer and nanometer scale features [48–51]thus enhancing its prominence in commercial optical design. This pertains to having closely packed meta-atoms (small periodicity Λ) operating at shorter wavelengths λ. In the theoretical domain, it is crucial to efficiently simulate the electromagnetic response of such nano-scale designs for interpreting experimental results and designing new materials and devices. Therefore, to fully benefit from these advancements, theoretical tools and nanofabrication techniques must develop in parallel.

Of course, any full-wave numerical simulations allows for an accurate and reliable computation of both the wave propagation and the scattering aspects of any structure. specifically, some tools such as the Fourier model method (FMM) [52], Finite element methods (FEM) [53], and Finite-Difference-Time-Domain method (FDTD) [54] provide exact field information including the transient, at any point within the simulation domain. In spite of the merits, the viability of these tools demands a heavy load on computational resources and requires additional post-processing to reveal the underlying physics. Moreover, any change in the geometry of the unit cell calls for a complete re-run of the numerical simulation even if the same materials are used. To circumvent most of these issues, we could shift our focus from the discrete nature of the material array to a more continuous and averaged picture. In other words, we can consider the entire material as a single entity with an overall far-field response and minimizing the importance of its specific geometrical features. This approach significantly simplifies the granular details associated with the infinite arrangement of discrete unit cell structures and instead emphasizes the significant collective effects. As a result, there is less of a need for meshing and the required memory space is reduced. This process of replacing the subwavelength periodic structure with its homogeneous equivalent medium is known as homogenization, which is governed by the effective medium theory (EMT). [5, 55–57]. A pictorial representation of the general idea behind homogenization is given in Fig. 1.1.

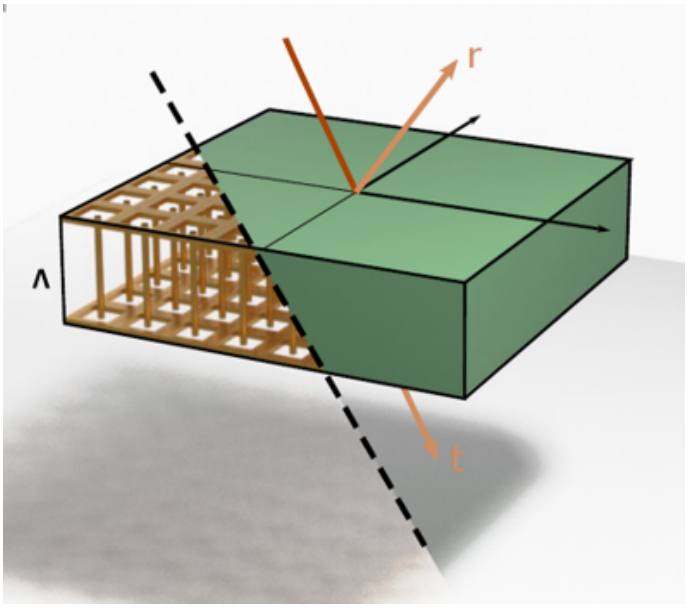

Figure 1.1.: The figure illustrates the homogenization problem. The left panel shows a cut of the metamaterial structure, while the right panel shows the equivalent homogeneous slab. By homogenizing a MM, we seek to find an equivalent homogeneous slab that can reproduce the reflection and transmission properties of an inhomogeneous metamaterial structure under plane wave illumination.

.

After homogenization, the overall response of the metamaterial can be represented by a set of frequency-dependent, complex-valued parameters known as the effective material parameters. These parameters are purely material-specific and do not contain any geometrical information. Consequently, if the homogenization process is deemed valid, it needs to be performed only once to predict the optical response of the material for a given geometry, as well as for changes in thickness.

1.2. Effective Medium Theory (EMT)

Traditionally, the study of light propagation through matter has been approached using macroscopic theories, which combine Maxwell's equations with an appropriate constitutive relation. The macroscopic Maxwell equations involve the four macroscopic fields: electric field **E**, magnetic field **H**, electric displacement **D**, and magnetic induction **B**. The constitutive relations describe the relationship between these fields, allowing the electric displacement and magnetic induction to be derived from the electric and magnetic fields, respectively.

In general, the constitutive relation can be written as,

$$\mathbf{D}(\mathbf{r}, k_0) = \varepsilon(k_0)\mathbf{E}(\mathbf{r}, k_0)$$

$$\mathbf{B}(\mathbf{r}, k_0) = \mu(k_0)\mathbf{H}(\mathbf{r}, k_0) \tag{1.1}$$

In this relation, the electric permittivity tensor is denoted by ε and the magnetic permeability tensor is denoted by μ. All quantities depend on the frequency ω or, alternatively, on the free space wavenumber $k_0 = \frac{\omega}{c}$, where $c = \frac{1}{\sqrt{\varepsilon_0 \mu_0}}$ is the speed of light in vacuum. Throughout this thesis, we use a normalized system with natural constants $\varepsilon_0 = 1$ and $\mu_0 = 1$ giving $\omega = k_0$, as stated in [58].

It is important to note that the constitutive relation depends on the properties of the medium, which can vary depending on many factors such as temperature, pressure, and the presence of other materials, to name a few. Therefore, the constitutive relation must be determined through theoretical models that take these factors into account.

Homogenization is a method used to derive constitutive relations for complex materials by approximating their behavior with that of an equivalent homogeneous material. This approach is typically based on the assumption that the material structure exhibits a periodicity that is smaller than half of the operating wavelength ($\frac{\Lambda}{\lambda} < \frac{1}{2}$), which is usually the case for metamaterials. The homogenization technique is often used in a phenomenological manner and offers a simplified approach to describing the behavior of complex materials [56]. The effective medium theory (EMT) is the theoretical framework that governs the homogenization technique.

The real advantage of using effective medium theory is to describe the material's response in terms of the *effective material parameters*). Ideally, after homogenization, these effective material parameters are sufficient to compute the electromagnetic response of a target object of any shape. Consequently, constructing and analyzing new geometries is a straightforward process by employing these effective material parameters.

Occasionally, it is useful to condense all of the material parameter tensors onto the displacement vector $\mathbf{D}(\mathbf{r}, k_0)$ using an arbitrary but differentiable gauge field $\mathbf{Q}(\mathbf{r}, k_0)$. This is possible because the displacement vector by definition is not uniquely formulated. In fact,

the Maxwell equations are invariant under the transformation [59]:

$$\mathbf{D}'(\mathbf{r}, k_0) = \mathbf{D}(\mathbf{r}, k_0) + \nabla \times \mathbf{Q}(\mathbf{r}, k_0), \quad \mathbf{H}'(\mathbf{r}, k_0) = \mathbf{H}(\mathbf{r}, k_0) - \mathrm{i}k_0\mathbf{Q}(\mathbf{r}, k_0). \tag{1.2}$$

On choosing $\mathbf{Q}(\mathbf{r}, k_0) = \alpha(k_0)\nabla \times \mathbf{E}(\mathbf{r}, k_0)$ and by setting $\left(k_0^2\alpha + \mu^{-1}\right) = \mathbb{1}$, *w.r.t* normalized units, we have the new form of constitutive relation as

$$\mathbf{D}(\mathbf{r}, k_0) = \varepsilon(k_0)\mathbf{E}(\mathbf{r}, k_0) + \nabla \times \alpha(k_0)\nabla \times \mathbf{E}(\mathbf{r}, k_0)$$

with

$$\mathbf{B}(\mathbf{r}, k_0) = \mathbf{H}(\mathbf{r}, k_0). \tag{1.3}$$

Notice that the effective magnetic permeability becomes an implicit quantity now described as a consequence of the second-order gradient of the electric field.with its components written as

$$\mu_{ij}(k_0) = \frac{1}{1 - k_0^2\alpha_{ij}(k_0)}.$$

The constitutive relation in its transformed form has proven to be effective in describing the impact of artificial optical magnetism in structures composed of materials that are not inherently magnetic. Specifically, certain designs involving sub-wavelength inclusions, such as those discussed in [4, 60–63] are known to carry signatures of induced magnetic effects. Investigating the microscopic current multipoles, this inclusion reveal a circular displacement currents within the unit cell particles. These currents act like a point source generating localized magnetic fields. A dense arrangement of such unit cell structures can be tuned to resonate at optical frequencies thereby manifesting a stronger optical magnetism. In the context of effective medium theory, the constitutive relation given in Eq. (1.3) shows a non-unity value for the magnetic permeability tensor $\mu(k_0)$, thereby revealing the existence of an induced local magnetic field in the optical structure.

For a Constitutive relation as in Eq. (1.1) to be valid, it is necessary that the characteristic length scale is $\frac{\Lambda}{\lambda} << 1$. This necessarily suggests that the wavelength of incoming light sees a dense arrangement of the unit cell particles, thereby capitalizing only on the average optical response. One of the first successful homogenization models dates back to the work of Maxwell-Garnett [64]. This approach is particularly applicable to systems with a

dilute concentration of unit cell particles immersed in a matrix medium with large volumes. In other words, operating the metamaterial in a quasi-static regime, where the spatial variation of the field across the period, Λ is negligible. Therefore the necessary but not sufficient condition of $\frac{\Lambda}{\lambda} << 1$ is met [65].

In the course of time, further extensions to the Maxwell-Garnett models were made to unravel new physics [66–68]. For instance, additional terms were introduced in the constitutive relations by Condon and Tellegen to accommodate optical activities in crystals [69, 70]. This effect is a consequence of the lack of mirror symmetry in the geometry of the unit cell structure. The Condon-Tellegen form of the constitutive relation is written as

$$\begin{aligned} \mathbf{D}(\mathbf{r}, k_0) &= \varepsilon(k_0)\mathbf{E}(\mathbf{r}, k_0) + \mathrm{i}\kappa(k_0)\mathbf{H}(\mathbf{r}, k_0) \\ \mathbf{B}(\mathbf{r}, k_0) &= \mu(k_0)\mathbf{H}(\mathbf{r}, k_0) - \mathrm{i}\kappa(k_0)\mathbf{E}(\mathbf{r}, k_0) \end{aligned} \tag{1.4}$$

where the additional term, the chirality tensor, given here as $\kappa(k_0)$, collects the natural coupling among the electric and magnetic fields. This coupling is generally referred to as the magnetoelectric effect and is the consequence of any mirror-asymmetry in the material. These materials are classified as chiral materials and are a very important class of materials. Conveniently, a transformation similar to Eq. (1.3) can be defined for the chirality parameter, thereby condensing once again all the material tensors onto the displacement field. Further discussions and application of the same are continued in detail in Section 3.2.

All the benefits of these analytical triumphs can be fully harvested only if the complete set of material parameterss is known a-priori to substitute the actual material. This indeed is not true for many MM and thus requires a means to assign the right set of material parameters that can completely describe the optics of the actual MM. This process of mapping effective material parameters with the optical response of the actual optical structure is called homogenization. Generally, a thin film made up of the desired material system is subjected to an incident beam of specific polarization (known state). Then, the interaction between the thin film and the incident light beam is quantified in terms of complex reflection and transmission coefficient which is then compared to the predictions from the homogenization models. A broad database containing the frequency-dependent material tensors is already in place for many metal and dielectric materials [71].

In the case of composite or artificial materials, experimental determination exists but is

not always viable [72–74]. Especially at optical and infrared frequencies, the fabrication of deterministic unit cell designs is challenging due to their very small unit cell sizes. However, recent advances in fabrication technology do offer improved means to tackle some of these shortcomings. Alternatively, computational optimization or retrieval methods have been put forward to carry out homogenization. In this technique, numerical experiments substitute for a lab environment [75, 76] and consequently, the simulated optical coefficients are then compared with the predictions out of the theoretical model. One such reliable approach is the S-parameter retrieval method [77]. In this approach, material parameters are extracted by inverting the scattering matrix calculated from bi-periodic slabs, periodic in two dimensions, and with a finite thickness in the third dimension, made from the considered MM unit cell.

Although retrieval methods are lucrative, they often encounter the non-uniqueness challenge in optimization problems.This challenge emerges when several sets of parameters can yield closely similar optimal outcomes. The issue is deeply rooted in the complexity of the optimization problem and the existence of numerous local optima, leading to ambiguity when selecting the most optimal solutions. Nevertheless, several strategies can be deployed to address this issue, such as including additional constraints or regularization terms or employing stochasticoptimization methods that sample from the solution space [78, 79], to mention a few.

In recent years, thanks to the computational prowess of modern computers, artificial neural networks (ANN) have emerged as a valuable tool for parameter retrieval. ANN offers a distinctive advantage in the realm of metamaterials, as the retrieval algorithm remains agnostic to unit cell design, thereby facilitating the simultaneous evaluation of multiple designs within a single simulation [80, 81].

On the theoretical front, significant efforts have been devoted to formulating fully analytical homogenization approaches, as it was done for the wire medium [82, 83], multi-layered structures [84–86], and certain resonator-based design [87–89]. Although these analytical approaches are very promising, the structural dependency of these approaches limits their usability.

Another noteworthy challenge in homogenization pertains to handling partial differential equations with highly oscillating coefficients. Asymptotic homogenization mitigates this

problem by studying the behavior of the response function from the homogenized medium ϕ_Λ as $\Lambda \to 0$ assuming the approximation $\phi_\Lambda \approx \phi$ holds, where ϕ is the actual response function [90–94]. Conversely, there are semi-analytical approaches grounded in field averaging techniques [95–97]. In these methods, numerical calculations are employed to determine the fields within the material domain, while the homogenization process itself remains entirely analytical. Additionally, a segment of mathematical asymptotic analysis delves into analytical homogenization methods [98–101].

All these approaches reveal that homogenization is a strong endeavor that allows one to discuss large systems with different components at the same physical level as any other natural material. In the limit of $\frac{\Lambda}{\lambda} << 1$ (negligibly small), the mesoscopic details remain relaxed and so the physical response of any material/metamaterial can be fully approximated by only a few material parameters. But when the $\frac{\Lambda}{\lambda}$ is not negligible, but still smaller than one, the light fields start to probe the heterogeneities of the unit cell and, therefore, the spatial dynamics become important. Many important applications, such as flat optics seek to boost and leverage these spatial dynamics to probe exciting qualities previously inaccessible [7, 102–104].

To not deviate from the focus of this thesis, we will limit our discussion to periodic metamaterials for which homogenization remains valid but when operated at a larger length scale, $\frac{\Lambda}{\lambda} < 1$. These materials are characterized by structural features that are designed on the order of the wavelength of the electromagnetic waves they interact with. As a result, when the wavelength of the incoming light is comparable to the size of these structural features, the electromagnetic response of the material to electromagnetic excitation extends beyond a single point in space and incorporates the field values in the vicinity. This response is called the non-local response and is highly exploited in the development of advanced technologies.

In the quasi-static limit ($\frac{\Lambda}{\lambda} << 1$), where the wavelength is much longer than the period, Λ, non-locality is present but negligible. Therefore, it is important to keep the characteristic length scale in mind when studying metamaterials.

To appreciate the practical benefits of non-locality, it is helpful to consider reciprocal space or Fourier space, where fields can be expanded as plane waves. In this space, the transfer function becomes a function of both the spatial frequency, represented by the wave vector

$\mathbf{k}$, and the temporal frequency, represented by k_0. The resulting function, denoted by $\mathbf{R}(\mathbf{k}, k_0)$, varies with $\mathbf{k}$, which is characteristic of non-locality. This property provides an additional degree of freedom that has a wide range of applications [105–107].

Composite media, such as MM with non-negligible $\frac{\Lambda}{\lambda}$, have a non-local response and thus spatial dispersion [108–111]. At this point, it is important to distinguish between *weak spatial dispersion* (WSD) and *strong spatial dispersion* (SSD). We do so in the context of effective medium theory. The zeroth order spatial dispersion effect or the natural impulse type response in a material is the electric permittivity ε. This is usually a basic electric response owing to the dipole polarization fields in a medium. Next, the first-order spatial dispersion effect $\left(\frac{\Lambda}{\lambda}\right)^1$, given by the chirality parameter κ. This parameter is the consequence of lack of reflection symmetry for the unit cell structure. Thus, for a unit cell design of high-symmetry, this effect vanishes. Further moving on to the second order spatial dispersion effects, $\left(\frac{\Lambda}{\lambda}\right)^2$, captured by the magnetic permeability tensor μ as in Eq. (1.3). This is an important effect because μ also accounts for any induced magnetic response, *i.e.,* an artificial magnetization in an otherwise non-magnetic unit cell structure. At optical frequencies, natural material shows very negligible values for $\left(\frac{\Lambda}{\lambda}\right)^2$. This explains the absence of any magnetic response in natural materials. Both the first and second-order spatial dispersion effects are categorized under the *weak spatial dispersion* (WSD). The model is called *weak* because it is possible to re-write both chirality and the magnetic permeability tensors in terms of magnetic induction $\mathbf{B}$, a local field similar to the electric field $\mathbf{E}$, such that no spatial derivatives are involved. This sets in the definition for the *strong spatial dispersion* (SSD) model. The quantities in a constitutive relation that cannot be reduced to a local model and thus have to retain spatial derivatives, usually, third order parameter, $\left(\frac{\Lambda}{\lambda}\right)^3$ and further higher orders, are categorized under the SSD models. Consequently, the existence of non-zero spatial derivatives assumes great importance in capturing non-local effects. Therefore, in efforts to capture these non-negligible spatial interactions and to record their impact on the response function, additional material parameters are introduced into the constitutive relation plus the additional interface conditions. Now, it becomes necessary that we develop tools to effectively characterize such non-local MM and study them on a similar footing to that of natural materials. This is the central idea of this thesis.

1.3. Structure of the Thesis

In this thesis, we explore a promising approach for investigating bulk optical metamaterials. A general-purpose constitutive relation is used to describe the linear relationship between the induction vector $\mathbf{D}$ and the incident vector fields $\mathbf{E}$ through a generalized response function $\mathbf{R}$. This response function is formally defined as an entity of the space of distributions $\mathcal{D}'$ across the spatial domain, where the derivatives of the distribution functions form a complete set. Conveniently, the distribution is decomposed into a sequence comprising material coefficients and their corresponding spatial derivatives. Describing the response function in $\mathcal{D}'$ also provides a built-in definition of the functions at surface boundaries, which can be leveraged to solve the interface problem and establish continuity among the additional transverse propagating modes excited within the material volume, indicating the non-locality experienced by the medium. A detailed derivation of the same can be found in the works of Prof. Dr. Michael Plum and Dr. Andrii Khrabustovskyi [112] and a further extension of the applicability of the interface conditions up to an arbitrary order can be found in the work from Dr. Fatima. Z. Goffi [113] from the Institute of Analysis (IANA) at the Karlsruhe Institute of Technology (KIT), all the credits to the mathematical rigor go to them.

In chapter 2, we develop the core theoretical background required by this thesis. We start by discussing the phenomenological approach to the derivation of the macroscopic constitutive relation. This forms the basis for our discussions later on the physical origin of non-locality in metamaterial systems. To have a formal definition of the response function and to facilitate the derivation of the associated interface condition, we provide a brief overview of selected topics from distribution theory and functional analysis, with a focus on the weak formulation. At this stage, we would be equipped with the necessary response function but in an abstract form. After laying this groundwork, we move on to discuss the linear constitutive relation and present a detailed derivation of the curl-based non-local constitutive relation from a geometrical group theory perspective. This involves expanding the response function as an infinite series of tensor components, each of which contains a spatial derivative term acting on the field vector and associated tensor coefficients. We show that these tensor components can be reduced to matrices, whose elements carry the spatially independent effective material parameters. More importantly, deriving the curl-based formulation also contributes to understanding the underlying constraints obeyed

by the constitutive relations as a consequence of their mathematical definitions.

In chapter 3, we present two nonlocal models that incorporate significant spatial dispersion effects. Alongside the local WSD approach, we derive dispersion relations to analyze the behavior of electromagnetic waves within homogenized metamaterials. Subsequently, we obtain interface conditions for each model that enable the reconstruction of the Fresnel matrix, thereby facilitating the calculation of reflection and transmission coefficients for a homogeneous slab subjected to an incident wave.

Chapter 4 of this thesis delves into two different methods for achieving efficient homogenization of complex optical metamaterials. The first method involves treating the metamaterial as a bulk material and using efficient parameter retrieval techniques to assign effective material parameters. This methodology is primarily applied to artificial structures with predetermined scattering properties, allowing for a systematic study of homogenization models and leading to insightful conclusions, which are discussed in detail in this chapter.

The second method introduced in this chapter aims to capture the exact response of a material composed of a 3D lattice of electromagnetic scatterers. The key concept behind this novel homogenization approach is the "effective transition matrix" or the $\mathbf{T}_{\text{eff}}$-matrix, which is a linear operator that provides an exact description of the linear interaction between light and the bulk material, i.e., the infinite 3D lattice of scatterers. This approach offers an attractive incentive, namely the ability to provide an exact effective material parameter without the need for any computational retrieval processes.

Finally, in chapter 5, we summarize all the analytical and numerical results of this thesis and discuss possible future research endeavors as an extension of the results obtained in this thesis.

2. Theoretical Background

This chapter aims to establish the fundamental physical principles of electrodynamics in continuous media. Our first focus is on deriving the general constitutive relation, which we will use to study the propagation of light within a medium. To achieve this, we adopt a phenomenological approach that involves solving the Maxwell equations while considering the macroscopic behavior of materials under different electromagnetic conditions, such as their response to electric and magnetic fields. While the final fields obtained from this phenomenological approach provide us with useful information, it is only part of the picture. In this thesis, we are also interested in exploring the underlying material properties that contribute to the observed behavior of the medium. This study requires the introduction of a general response function $\mathbf{R}$, which is a function of both space and frequency, to redefine the constitutive relation in an abstract form, where the displacement vector $\mathbf{D}(\mathbf{r}, k_0)$ is expressed as a convolution of the response function $\mathbf{R}(\mathbf{r}, \mathbf{r}', k_0)$ and the exciting electric field $\mathbf{E}(\mathbf{r}', k_0)$. As a reminder, we are using the normalized units with $\varepsilon_0 = 1$ and $\mu_0 = 1$ making $\omega = k_0$. Furthermore, throughout this thesis, we consistently employ the plane wave ansatz for all the fields under consideration. Specifically, for the monochromatic case with frequency k_0 for some field $\mathbf{U}(\mathbf{r}, t)$, the field is given by $\mathbf{U}(\mathbf{r}, \mathbf{t}) = \mathbf{U}_0 e^{\mathrm{i}(\mathbf{k}\cdot\mathbf{r} - k_0 t)}$, where $\mathbf{U}_0$ represents the complex amplitude of the wave, and its real part corresponds to the physical field [*subsection 9.2.2*, [114]].

To obtain a more practical form of the constitutive relation, we express it in Fourier space and expand the response function as a sequence. The moment coefficient of this sequence contains the material parameter in its tensor form. And for the associated differential operator, We then delve into tensor algebra to arrive at the "curl" based constitutive relation that we will use in the following chapter to calculate the dispersion relation and the interface conditions. In the latter part of the derivation, we attempt to provide justification

for the choice of the "curl" operator-based form for the constitutive relation.

2.1. Linear Constitutive Relation: Phenomenological Approach

When a medium is exposed to an external electromagnetic field, the medium becomes polarized in response to the field. This polarization characterizes the medium's response to the applied electric and magnetic fields. Two primary quantities used to describe the polarization response of a homogeneous medium are the electric and magnetic polarization fields $\mathscr{P}[\mathbf{E},\mathbf{B}]$ and $\mathscr{M}[\mathbf{E},\mathbf{B}]$, respectively. In the most general case of absence of any centrosymmetry, both quantities are induced by the macroscopic electric field $\mathbf{E}$ and the magnetic induction $\mathbf{B}$ [*section 1.4*, [115]], [116]. These quantities contain the actual response of the material. It is not possible within the realm of electrodynamics to get access to the exact functionality of the polarization/magnetization on the fields, this requires a microscopic/multipolar treatment [*Chapter 1,* [117]].

The concept of non-locality or spatial dispersion arises when the values of the polarization fields at any point in the medium depend not only on the local fields but also on the electric and magnetic fields at distant points in the same medium. This means that the polarization response at any given point is influenced not only by the local fields but also by the fields at other locations in the medium, and this influence is conveyed by the spatial derivatives of the electric and magnetic fields [58]. This notion will be justified in the following.

When an electric field is applied to a medium, it can induce a separation of charges and create a polarization within the material. This polarization results in the accumulation of bound charge density ρ_b, which gives us the net charge per unit volume of the material. This ρ_b proportional to the strength of the electric field. Consequently, induced charge densities arise as the applied field induces slight shifts or distortions in the bound charge density. This effect is specifically significant in metamaterials with characteristic lengths only slightly smaller than the wavelength of light. In such cases, spatially non-uniform electromagnetic fields across the material's unit cell need to be taken into consideration.

Broadly speaking, the motion of the bound charge density can be divided into two induced charge densities [*Chapter 4*, [114]]. The electric polarization field is characterized in a phenomenological manner by the induced charge density [*Section 4.3*, [115]]

$$\rho^{\mathrm{e}}_{\mathrm{ind}}(\mathbf{r},k_0) = -\nabla.\mathscr{P}(\mathbf{r},k_0) \quad , \tag{2.1}$$

Which gives the induced current density, a consequence of the transnational motion of the induced charge density whence obeying the continuity equation

$$\nabla.(\mathbf{J}^{\mathrm{e}}_{\mathrm{ind}}(\mathbf{r}, k_0) + \mathrm{i}k_0\mathscr{P}(\mathbf{r}, k_0)) = 0 \quad . \tag{2.2}$$

Here, both $\rho^{\mathrm{e}}_{\mathrm{ind}}(\mathbf{r}, k_0)$ and $\mathbf{J}^{\mathrm{e}}_{\mathrm{ind}}(\mathbf{r}, k_0)$ refers to the amount of charge that is redistributed within the material due to the applied electric field.

The complementary quantity the magnetic charge density $\rho^{\mathrm{m}}_{\mathrm{ind}}$ is a quantity, when excited by an incident field moves along a closed loop. This motion generates a divergence-free magnetic polarization field, giving rise to a faint magnetic current density, written as

$$\mathbf{J}^{\mathrm{m}}_{\mathrm{ind}}(\mathbf{r}, k_0) = \nabla \times \mathscr{M}(\mathbf{r}, k_0) \quad , \tag{2.3}$$

Reciprocal systems, defined by the Casimir-Onsager relations, do not allow induced polarization from magnetic current elements unless introduced externally. In such systems, it is meaningless to separate the induced currents into electric or magnetic components. However, the presence of magnetic polarization fields $\mathscr{M}$ is not invalidated, and artificial magnetization effects are associated with it due to spatial dispersion effects. Similarly, if the unit cell geometries of the material lack central symmetry, the overall material shows significant first-order spatial dispersion effects further contributing to $\mathscr{M}$. The total current density throughout the entire material volume can be written as

$$\mathbf{J}(\mathbf{r}, k_0) = -\mathrm{i}k_0\nabla.\mathscr{P}(\mathbf{r}, k_0) + \nabla \times \mathscr{M}(\mathbf{r}, k_0) \quad . \tag{2.4}$$

This total current density in the medium can be used to express the electric displacement and magnetic induction fields [*chapter 4*, [115]], given as

$$\mathbf{D}(\mathbf{r}, k_0) = \mathbf{E}(\mathbf{r}, k_0) - \tfrac{\mathbf{J}(\mathbf{r}, k_0)}{ik_0}, \qquad \mathbf{B}(\mathbf{r}, k_0) \quad = \mathbf{H}(\mathbf{r}, k_0) \quad , \tag{2.5}$$

and therefore rewriting them w.r.t Eq. (2.4), we arrive at the desired form of the constitutive

relation

$$\mathbf{D}(\mathbf{r}, k_0) = \mathbf{E}(\mathbf{r}, k_0) + \mathscr{P}(\mathbf{r}, k_0) + \nabla \times \mathscr{M}(\mathbf{r}, k_0),$$

$$\mathbf{B}(\mathbf{r}, k_0) = \mathbf{H}(\mathbf{r}, k_0) \quad . \tag{2.6}$$

This form for the $\mathbf{D}(\mathbf{r}, k_0)$ and $\mathbf{B}(\mathbf{r}, k_0)$ fields is fundamental as they can be used to reproduce all of the Maxwell equations for the given medium [*Section 4.3*, [115]].

In conclusion, we have obtained the constitutive relation using a phenomenological approach, which involved utilizing polarization fields to calculate the displacement field for a given electric field. While this approach offers valuable insights into the fields present in the medium, it offers only a limited perspective on the material's characteristics. To gain a more complete understanding of the material properties, it is necessary to derive the constitutive relation in terms of a response function, which we will investigate in upcoming sections.

2.2. General Response Function and Spatial Dispersion

If we assume that metamaterials (MMs) are inherently non-magnetic, we can express the linear relationship between the magnetic induction and the magnetic field as $\mathbf{H}(\mathbf{r}, k_0) = \mathbf{B}(\mathbf{r}, k_0)$. Additionally, for mesoscopic MMs where $\frac{\Lambda}{\lambda} < 1$, the response tensors linking the electric field to the electric displacement exhibit non-local effects. Specifically, the response of MMs to an electric field at a particular point $\mathbf{r}$ is influenced not only by the electric field at that point but also at distant points $\mathbf{r}'$ within a specified spatial domain surrounding the observation point $\mathbf{r}$. This results in a constitutive relation given by [113]:

$$\mathbf{D}(\mathbf{r}, k_0) = \int \mathbf{R}(\mathbf{r}, \mathbf{r}', k_0)\mathbf{E}(\mathbf{r}', k_0)\mathrm{d}\mathbf{r}' \quad . \tag{2.7}$$

where k_0 represents the frequency dispersion of the medium, accounting for temporal retardation in real space. The explicit dependence of the response function on both $\mathbf{r}$ and $\mathbf{r}'$ reflects the spatial non-locality.

At the effective level, non-local homogenization theory simplifies the response function to only depend on the Euclidean distance between the observation point $\mathbf{r}$ and distant points

$\mathbf{r}'$. This is expressed by the general constitutive relation:

$$\mathbf{D}(\mathbf{r}, k_0) = \int \mathbf{R}(\mathbf{r} - \mathbf{r}', k_0)\mathbf{E}(\mathbf{r}', k_0)dr' \quad . \tag{2.8}$$

where the non-local response kernel $\mathbf{R}(\mathbf{r} - \mathbf{r}', k_0)$ is defined as [*Section 3.2.2*, [118]]:

$$\mathbf{R}(\mathbf{r} - \mathbf{r}', k_0) = \mathbb{1}\delta(\mathbf{r} - \mathbf{r}') + \chi(\mathbf{r} - \mathbf{r}', k_0). \tag{2.9}$$

By introducing the macroscopic susceptibility function $\chi(\mathbf{r} - \mathbf{r}', k_0)$, all spatial dispersion effects, including both weak and strong ones, can be accounted for at the effective level. The susceptibility function is not restricted to the long wavelength approximation and incorporates information from higher-order gradients of the electric field. Additionally, a direct relationship between the response kernel and the polarization fields is apparent when comparing this definition of the response kernel with Eq. (2.6).

$$\mathscr{P}(\mathbf{r}, k_0) = \int \chi(\mathbf{r} - \mathbf{r}', k_0)\mathbf{E}(\mathbf{r}', k_0)\mathrm{d}\mathbf{r}' \quad . \tag{2.10}$$

It is worth noting that we assume $\mathscr{M}$ to be zero in our material since it is intrinsically non-magnetic. This assumption is reasonable as artificial magnetization in optical metamaterials arises from spatial dispersion effects, which can be fully captured by the susceptibility function $\chi(\mathbf{r} - \mathbf{r}', k_0)$.

Performing a Fourier transform on the positional difference $\mathbf{r} - \mathbf{r}'$ and transforming it to reciprocal space $\mathbf{k}$ corresponds to spatial dispersion. The spatial frequency $\mathbf{k}$ is a vector representing inverse length units, and the Fourier transforms simplifies convolution into algebraic products, giving Eq. (2.8) as

$$\hat{\mathbf{D}}(\mathbf{k}, k_0) = \hat{\mathbf{R}}(\mathbf{k}, k_0)\hat{\mathbf{E}}(\mathbf{k}, k_0) \tag{2.11}$$

The response function strictly follows the Casimir-Onsager relation as it satisfies all the restrictions imposed by Maxwell's equations. For any arbitrary $\mathbf{k} = \{k_x, k_y, k_z\}$ and k_0, we have

$$\hat{R}_{ij}(\mathbf{k}, k_0) = \hat{R}_{ji}(-\mathbf{k}, k_0) \tag{2.12}$$

In the special case where the unit cell of the material lacks central symmetry, the material is categorized as non-gyrotropic to ensure a reflection symmetry. This gives the response function an additional symmetry:

$$\hat{R}_{ij}(\mathbf{k}, k_0) = \hat{R}_{ji}(\mathbf{k}, k_0). \tag{2.13}$$

Such symmetry for the response function is later exploited to simplify the analytic expressions, and therefore, expedite the homogenization process.

Please note in this thesis, we work only with harmonic fields. so it's simpler to work with reciprocal space for all fields and associated functions. To enhance readability, we omit the extra $\hat{}$ symbol on Fourier space quantities.

2.3. Derivation of the Special Curl-Based Constitutive Relation

The main objective of this thesis is to develop a response function that can effectively describe the physics of metamaterials. However, the expressions presented in equations Eq. (2.8) or Eq. (2.11) are only applicable to infinitely extended homogeneous media. Since the material is actually confined to a finite volume, which must be significantly larger than the wavelength ($V >> \lambda^3$), we need to formulate the response function in a way that can describe a finite medium. Specifically, the homogeneous material with volume V is embedded in a homogeneous host medium, typically a local medium defined by electric permittivity and permeability, which leads to an interface problem. In other words, there is an interface between a local and a non-local medium, necessitating the derivation of new interface conditions. This, in turn, requires both fields to be in the real space notation.

Previously, [59] proposed an asymptotic method for converting the response function $\mathbf{R}(\mathbf{k}, k_0)$ from the reciprocal space notation to the real space notation. The approach involves taking a three-dimensional Taylor series of the response function as $|\mathbf{k}|$ approaches zero. By doing so, convolution integrals can be avoided, and lower orders of field gradients can be retained. If we keep up to the second-order derivatives, the expression becomes [59]:

$$\begin{aligned}\mathbf{R}(\mathbf{k}, k_0) &\approx \mathbf{R}_{ij}(\mathbf{k}=0, k_0) + \left.\frac{\partial \mathbf{R}_{ij}(\mathbf{k}, k_0)}{\partial k_k}\right|_{\mathbf{k}=\mathbf{0}} k_k + \frac{1}{2}\left.\frac{\partial \mathbf{R}_{ij}(\mathbf{k}, k_0)}{\partial^2 k_k \partial k_l}\right|_{\mathbf{k}=\mathbf{0}} k_k k_l \\ &= \frac{1}{\mathrm{i}\, k_0}[a_{ij}(k_0) + b_{ijk}(k_0)k_k + c_{ijkl}(k_0)k_k k_l]\end{aligned} \tag{2.14}$$

The i k_0 factor is collected from the derivatives and the tensor indices are assumed to follow Einstein summation.

The first term in the expansion describes the local response of the material when $|\mathbf{k}| = 0$. This constant term in reciprocal space does not depend on the components of the wave vector, and as a result, the constitutive relation in real space (given in Eq. (2.8)) considers only the response at the point $\mathbf{r}$. However, as the average field variations across the material volume become significant, higher-order gradients of $\mathbf{k}$ become important. In Eq. (2.14), these gradients are considered up to the second order. The initial assumption, which holds for $|\mathbf{k}| \to 0$ (i.e., $\lambda \to \infty$), requires the unit cell dimensions (Λ) to be small or for the concentration to be very dilute, for the ratio $\frac{\Lambda}{\lambda}$ to be finite. This implies weak interaction among the unit cell structures and limits the analysis to the WSD limit. Additionally, as $|\mathbf{k}| \to 0$, the quality of the approximation of $\mathbf{R}$ worsens as $\frac{1}{|\mathbf{k}|}$, making this model unsuitable for analyzing non-local metamaterials.

2.3.1. Functional Space Definition of the Response Function

In order to clarify the mathematical operations involved with the response function and the general non-local constitutive relation introduced in Eq. (2.8), it is necessary to provide a detailed mathematical definition. This is particularly important because in Eq. (2.9), it is apparent that the response function is a distribution. Additionally, in the later parts of the thesis, the wave propagation inside a medium is studied by solving the dispersion relation using a plane wave ansatz for the eigenmodes excited in the homogeneous medium. It is worth noting that the electric field is only locally integrable mathematically, and therefore, their Fourier transform must be introduced carefully. With this in mind, this section aims to clarify the mathematical foundation of the response function and the definition of the general non-local constitutive relation.

We refer to the alternate definition of the response kernel from the work of K.Mnasri in [118]. Here, the response function is defined as a linear combination of Dirac $\delta-$distribution and their partial derivatives *w.r.t.* spatial quantity $\mathbf{r}$. In equation form, we write

$$\mathbf{R}(\mathbf{r}-\mathbf{r}', k_0) = \sum_{n\in\mathbb{N}^3, |n|\leq 3} \mathrm{C}_n(k_0) D^n \delta(\mathbf{r}-\mathbf{r}') \quad , \tag{2.15}$$

with $\mathrm{N} \in \mathbb{N}$ the truncation order, $\mathrm{C}_n \in \mathbb{C}^{3\times 3}$ are the coefficients associated with the power

series expansion: called the effective material parameters, and $D^n = \nabla_{n1}, \nabla_{n2}, \nabla_{n3}$. As a consequence of homogenization, this definition ensures the effective material parameters C_n are spatially independent and show only a temporal dispersion across the given frequency k_0.

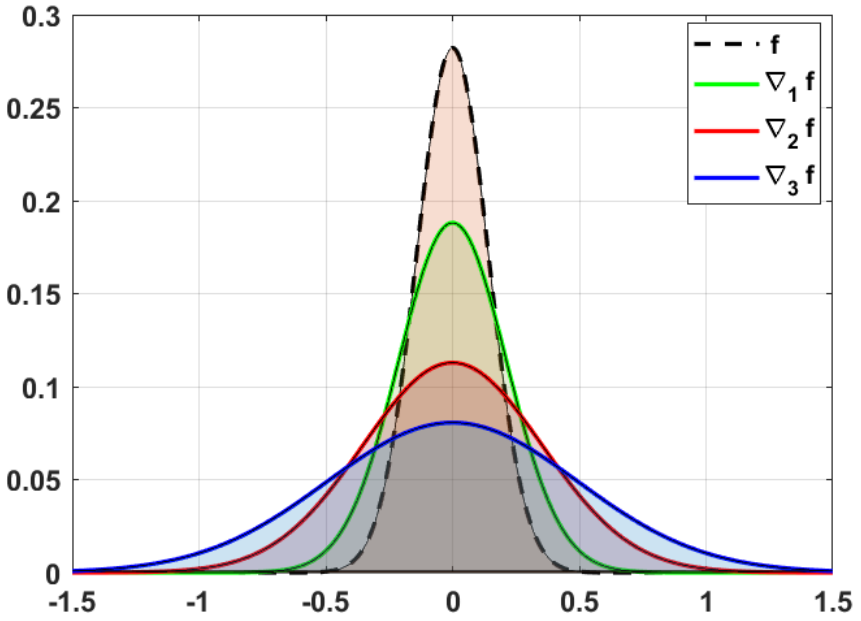

Figure 2.1.: Illustration of a distributional function $f = \frac{1}{\epsilon} e^{\frac{-x^2}{\epsilon^2}}$ and its first three derivatives, $\nabla_1 f, \nabla_2 f, \nabla_3 f$ representing the inclusion of long-range interactions.

Before we move ahead, some remarks are necessary. The non-locality in the medium is encrypted in the derivatives of the $\delta-$distribution. Additionally, In mathematical terms, this treatment comes with strict restrictions on the response function. Furthermore, the Dirac $\delta-$distribution and its derivatives are categorized as a special type of function called a "*generalized function*" or a "*distribution*" that acts on infinitely differentiable complex-valued functions $\boldsymbol{\phi} \in \mathcal{C}^\infty$ vanishing at infinity, *i.e.,* having a *compact support*. Usually, the space of $\mathcal{C}^\infty$ functions is called the space of test function in a material domain Ω. This notion of compact support ensures the test function $\boldsymbol{\phi}$ is a slowly varying function that vanishes as we approach the boundary enclosing the material domain Ω of volume $|\Omega| = V$. Thereby compensating for the boundary problem *w.r.t.* response $\mathbf{R}$. In a more formal mathematical definition [*Chapter 2*, [119], [118]],

Definition 2.3.1 *The space of distributions, denoted with $\mathcal{D}'(\Omega)$ on a domain $\Omega \subset \mathbb{R}^n$, is defined as the space of linear functionals acting on the space of infinitely differentiable functions, $\mathcal{C}^\infty$ with compact support, denoting this space by $\mathcal{D}(\Omega)$.*

Therefore, the distribution $\mathcal{D}'(\Omega)$ is the dual space of $\mathcal{D}(\Omega)$. This definition allows one to further define the Dirac $\delta-$distribution, $\delta \in \mathcal{D}'(\mathbb{R})$ as a linear continuous map *:

$$\langle \delta(\mathbf{r}-\mathbf{r_0}), \boldsymbol{\phi}(\mathbf{r}) \rangle = \int_{\omega} \delta(\mathbf{r}-\mathbf{r_0})\ \boldsymbol{\phi}(\mathbf{r})\ \mathrm{d}\mathbf{r} = \boldsymbol{\phi}(\mathbf{r_0})\ \forall\ \boldsymbol{\phi}\ \in\ \mathcal{D}(\omega). \tag{2.16}$$

where, $\langle ., . \rangle$ represents the duality pairing for the spaces $\mathcal{D}(\Omega)$ and $\mathcal{D}'(\Omega)$.

The derivative of a distribution $\Theta \in \mathcal{D}'(\Omega)$ is defined in a weak sense, meaning for a test function $\boldsymbol{\phi} \in \mathcal{D}(\Omega)$, we have,

$$\langle D^{\alpha}\Theta, \boldsymbol{\phi} \rangle_{\Omega} = (-1)^{|\alpha|} \langle \Theta, D^{\alpha}\boldsymbol{\phi} \rangle_{\Omega} \quad . \tag{2.17}$$

The aim of the general discussion is to address the interface problem between a non-local and a local medium [113, 116]. In this context, "the interface problem" refers to the challenge of reconciling the different behaviors of a local material and a non-local material at their interface. This is accomplished by obtaining the weak form of the response function, which involves multiplying the strong form (i.e., the partial differential equation with no reduction in the order of derivatives) by a test function $\boldsymbol{\phi}$. This allows us to perform a partial integration operation at the interface Γ, where the response function is otherwise discontinuous and any continuous operators are not well-defined. This allows for a smooth transition between the local and non-local regions and ensures that any continuous operators are well-defined.

Furthermore, it is important to note another significant benefit of defining the response as an element of the space of generalized functions. This approach enables the independent treatment of the Fourier transform of the response function and the Fourier transform of both the Delta distribution and its derivative [Chapter 9, [119]], [120].

1. To elaborate, we first describe the distribution and its derivatives, defining the response function, to be a *slowly* growing functional. When interpreted mathematically, This allows one to define a distribution $\mathbf{T}$ and its derivatives $D^{\alpha}\mathbf{T}$ as an element of the space $\mathcal{S}'(\Omega) \subset \mathcal{D}'(\Omega)$. The space $\mathcal{S}'(\Omega)$ is called the space of tempered distribution and is very restrictive compared to $\mathcal{D}'(\Omega)$. Such a definition of the response function

*We would like to draw the reader's attention to a minor but yet important mathematical detail: since Dirac $\delta-$distribution is not a *actual* function in a strict mathematical language, writing an integral is not correct. To overcome this, it is understood that, the function $\mathrm{F}(\mathbf{r})$ holding the relation $\mathrm{F}(\mathbf{r}) = \delta(\mathbf{r}-\mathbf{r_0})\ \boldsymbol{\phi}(\mathbf{r}) = \lim_{\triangle \mathbf{r} \to 0} \mathrm{F}(\mathbf{r})$ has a point-wise convergence outside of singular point $\mathbf{r_0}$.

in terms of the space $\mathcal{S}'(\Omega)$ further allows finer gradients (higher order derivatives) of the response function to be significant therefore enabling one to consider further long-range interactions. Nevertheless, in this setting, the definition of the test function must also be revised. To ensure a finite value for the response function, the test function $\boldsymbol{\phi}$ is an element of the *rapidly decreasing* infinitely differentiable functions are defined in the less restrictive space $\mathcal{S}(\Omega)$. As it is obvious, $\mathcal{S}'(\Omega)$ is the dual space for the space $\mathcal{S}(\Omega)$.

Therefore, the Fourier transform of the tempered distribution function is defined in a weak sense, (a corollary of Parseval's identity), as

Definition 2.3.2 *The Fourier transform,* $\mathscr{F}[\mathbf{T}]$ *for any* $\mathbf{T} \in \mathcal{S}'(\Omega)$ *and any* $\boldsymbol{\phi} \in \mathcal{S}(\Omega)$*,*

$$\langle \mathscr{F}[\mathbf{T}], \boldsymbol{\phi} \rangle \coloneqq \langle \mathbf{T}, \mathscr{F}[\boldsymbol{\phi}] \rangle \quad . \tag{2.18}$$

Using this definition, the Fourier transform of the $\delta-$distribution is read as,

$$\langle \mathscr{F}[\delta], \boldsymbol{\phi} \rangle \coloneqq \langle \delta, \mathscr{F}[\boldsymbol{\phi}] \rangle = \int_{\Omega} \hat{\boldsymbol{\phi}}(\mathbf{r}) \, \mathrm{d}\mathbf{r} = \hat{\boldsymbol{\phi}}(0) \implies \langle 1, \boldsymbol{\phi} \rangle \quad . \tag{2.19}$$

2. With respect to the Fourier transform of the derivatives. For all the slowly decreasing functions, $|f(\mathbf{r})| \to 0, \forall |\mathbf{r}| \to 0$ in $\mathbf{L}^2(\mathbb{R}^n)$ and for all the dense subset of $\mathbf{L}^2(\mathbb{R}^n)$ (e.g $\mathcal{S}(\Omega)$) , the Fourier transform over a variable $\mathbf{r}$ follows,

$$\mathscr{F}[D^{\alpha} f](\mathbf{r}) = \mathrm{i}^{|\alpha|} \mathbf{r}^{\alpha} \mathscr{F}[f](\mathbf{r}) \quad , \tag{2.20}$$

implying that, the derivative simply reduces to an algebraic product with the variable $\mathbf{r}$

$$D^{\alpha} \to \mathrm{i}^{|\alpha|} \mathbf{r}^{\alpha} \quad , \tag{2.21}$$

Thereby representing the 3-dimensional spatial derivative, $\boldsymbol{\nabla}$, and the time derivative operator in Fourier space as,

$$\boldsymbol{\nabla}_{x,y,z} = (\partial_x, \partial_y, \partial_z) \longleftrightarrow \mathrm{i}(k_x, k_y, k_z)$$

$$\nabla_t = \partial_t \longleftrightarrow -\mathrm{i}\, \omega \approx -i\, k_0|_{\mathbf{c=1}} \tag{2.22}$$

Next, we move ahead to define the fields defining the material system and thus the constitutive relation in the functional space setting.

When studying theoretical electrodynamics, we constantly encounter 4 major vectors: **E**, **H**, **D** and **B**. These vectors are convenient to handle because of their definition in the Hilbert space of square-integrable functions (L^2), resulting in a well-defined norm $\|.\|$. Additionally, Maxwell equations relates all these four quantities through simple partial differential equations (PDE), which conveniently fetch the solution for these vector fields in a medium with well-defined energy operator [*Section 1.3*, [121]].

Definition 2.3.3 *Let $\mathcal{V}$ be a vector space with a scalar product $(\ .\ ,\ .\ )_{\mathcal{V}}$. If $\mathcal{V}$ is complete* w.r.t. *the norm $\|.\|_{\mathcal{V}}$ it is called a* ***Hilbert space****.*

Here, the scalar product on $\mathcal{V}$ is a map $(\ .\ ,\ .\ )_{\mathcal{V}} : \mathcal{V} \times \mathcal{V} \to \mathbb{C}$ such that it satisfies the following properties:

1. for all $(u, v) \in \mathcal{V}$, the map is symmetric in (u, v) as $(u, v))\mathcal{V} = (v, y)_{\mathcal{V}}$
2. for all vectors u, the map is positive definite: $(u, u)_{\mathcal{V}} \geq 0$ and $(u, u)_{\mathcal{V}} = 0$ only if $u = 0$
3. it is linear with respect to the scalar α, β as

$$(\alpha u + \beta v, w) = \alpha(u, w) + \beta(v, w)$$

   for all $u, v, w \in \mathcal{V}$
4. and the associated norm is given as

$$\|u\|_{\mathcal{V}}^2 = (u, u)_{\mathcal{V}} \tag{2.23}$$

We have placed significant emphasis on the formal definitions of these functions, as they hold great importance. Specifically, defining these functions in a Hilbert space with an L^2-norm is highly attractive in physics, as all physical observables, such as energy, are defined in the space of square-integrable functions. Additionally, the L^2 space conveniently connects with the Fourier domain.

Furthermore, spatial derivatives in real space are equivalent to polynomial multiplication of $\mathbf{k}$ in reciprocal space. As a result, the constitutive relation can be expressed in its complete form as follows.

$$\mathbf{D}(\mathbf{k}, k_0) = \mathbf{R}(\mathbf{k}, k_0)\mathbf{E}(\mathbf{k}, k_0) = \sum_{n\in\mathbb{N}, |n|\leq \mathrm{N}} \mathrm{C}_n(k_0)\mathbf{k}^n\mathbf{E}(\mathbf{k}, k_0) \tag{2.24}$$

The zeroth order coefficient, C_0 is the standard electric permittivity tensor $\varepsilon_{ij}(k_0)$, which captures the local electric response of the medium. Consequently, we can map the coefficient C_1 to a magnetoelectric effect owing to its association to the first-order gradient of the $\nabla_1\mathbf{E}$ field, and then the coefficient C_2 to the artificial magnetism due to its association with the second order gradient $\nabla_1\nabla_2\mathbf{E}$ field. The further higher-order gradient terms and the associated coefficients represent the additional non-local material parameters.

In this regard, the i^{th} component D_i of the displacement field up to an arbitrary number of terms can be read as,

$$D_i = a_{ij}E_j + b_{ijk}\ k_kE_j + c_{ijkl}k_kk_lE_j + d_{ijklm}\ k_kk_lk_mE_j + \text{H.O.T.} \tag{2.25}$$

Each tensorial coefficient in this context possesses dimensions of both lengths and inverse time [58, 59]. As a result, each tensor coefficient is an element of the tangent space, denoted as $T_{i...r} \in T_p$, with $T_{i...r}$ serving as a placeholder for each tensor coefficient. These coefficients contain frequency-dependent material parameters, requiring a suitable means of decoding to obtain effective material parameters for effective medium theory. Further discussion on this topic is presented in the subsequent subsection.

Since the response function R_{ij} itself abides by the Casimer-Onsager relations as written in Eq. (2.12) and Eq. (2.13), the tensor components also inherit the symmetry properties, thereby reducing the number of independent coefficients:

$$a_{ij} = a_{ji} \quad b_{ijk} = -b_{\sigma(jik)\neq(ijk)} \quad c_{ijkl} = c_{\sigma(ijkl)} \tag{2.26}$$

where the permutation operator $\sigma \in \mathscr{G}$ is used from the symmetric group of all permutations $\mathscr{G}$.

2.3.2. Introduction to Tensors

In this particular section of the thesis, the focus is on deriving the special "curl" form of the constitutive relation. Although this form has been previously utilized in both the WSD and SSD models, the reason for choosing a curl-based formulation is to match the divergence-free nature of the homogeneous Maxwell equations. By using abstract mathematical concepts and calculus, the aim is to understand the origin of this derivation and comprehend the fundamental constraints that govern our general constitutive relations.

The starting point of the derivation is to express the response function $\mathbf{R}(\mathbf{k}, k_0)$ in terms of tensors living in a 3-dimensional Euclidean space. This approach facilitates the representation of the constitutive relation in a convenient form, which helps us to uncover its underlying properties and limitations. Through this process, we explore how the curl form of the constitutive relation emerges and the reasons why it is of particular significance in certain physical applications.

A mathematical vector is an element of the vector space $\mathcal{V}$, which has a dimension of d over a field $\mathbb{K}$ that can be either $\mathbb{R}^n$ or $\mathbb{C}^n$. The dual vector space, denoted as $\mathcal{V}^*$, is the space of linear functional mappings from $\mathcal{V}$ to $\mathbb{K}$.

When a basis $\{e_i\} \in \mathcal{V}$ is chosen, the vector $\mathbf{v}$ can be viewed as having components v^i in the co-variant basis. This selects $\{e^i\}$ as the choice for the contravariant basis, and the vector $\mathbf{v}^* \in \mathcal{V}^*$ is the vector components in the dual space.

This formalism allows us to define a scalar-valued multi-linear function with variables in either $\mathcal{V}$ or $\mathcal{V}^*$ called a *tensor* over $\mathcal{V}$ and the space of tensors called a *tensor space* $\mathcal{T}$ over $\mathcal{V}$. A tensor $\mathbf{T}^r_s \in \mathcal{T}$ is typically represented as,

$$\mathbf{T}^r_s = \underbrace{\mathbf{v}^* \otimes \ldots \mathbf{v}^* \otimes}_{\text{r times}} \underbrace{\mathbf{v} \otimes \ldots \mathbf{v}}_{\text{s times}} \quad , \tag{2.27}$$

where, $\mathbf{v} \in \mathcal{V}$ and $\mathbf{v} \in \mathcal{V}^*$ are the *d-dimensional* vectors in their respective spaces. In this representation, the *degree* of the tensors $\mathbf{T}^r_s$ is written as (r, s) and denotes r the number of vector contributions from the *contra-variant* vector space $\mathcal{V}^*$ and s the contribution from *co-variant* vector space $\mathcal{V}$. As a corollary, we can also conclude that the dimension of the tensor $\mathbf{T}^r_s$ is $d^n(r+s)$ where d is the dimension of each vector. For instance, $(2, 0)$ is a purely contra-variant tensor of degree 2 written as $\mathbf{T}^2_0(V) = \mathbf{v}^* \otimes \mathbf{v}^*$, $(0, 2)$ denotes a

purely co-variant tensor of degree 2 written as $\mathbf{T}_2^0(V) = \mathbf{v}^* \otimes \mathbf{v}^*$ and a mixed form of degree $(1,1)$ written as $\mathbf{T}_1^1 = \mathbf{v}^* \otimes \mathbf{v}$.

In the interest of reducing complexities, it is wise to briefly discuss the lowering and raising operation on the tensors. In reality, when dealing with a tensor defined on a vector space of spatial coordinates, it is safe to assert that the co-variant and contra-variant contribution to the construction of the tensor is less relevant. The metric tensor g can be employed as an isomorphism between the vector space and their dual, therefore allowing one to express a co-variant index of a tensor as a contra-variant index linearly scaled by the metric tensor $\mathbf{g}$.

To formally introduce the metric tensor: $\mathbf{g} : \mathcal{V} \times \mathcal{V} \to \mathbb{K}$ is a bi-linear form that allows defining the distance and angle between any two vectors in $\mathcal{V}$. The action of the metric tensor can be written as $\mathbf{g}(v_i, v_j) = g_{ij}$ forming an $n \times n$ symmetric matrix. Additionally, $\mathbf{g}$ assumes a non-degenerate value, meaning $\mathbf{g}(\mathbf{u}, \mathbf{v}) = 0$, only if $\mathbf{u} = \mathbf{v} \; \forall \; \mathbf{u}, \mathbf{v} \; \neq 0 \in \mathcal{V}$. This guarantees the inverse metric tensor g^{ij} also exists [*Section 0.2.2, 2.13*, [122]].

Then, for tensors of order $(0, s)$, the raising of the tensor indices can be generally written as [*Chapter 2*, [122]][*chapter 2*, [123]]

$$g^{j_1 i_1} g^{j_2 i_2} \dots g^{j_s i_s} T_{i_1 \dots i_s} = T^{j_1 \dots j_s} \tag{2.28}$$

and for tensors of order $(r, 0)$, the lowering of the tensor indices can be written as

$$g_{j_1 i_1} g_{j_2 i_2} \dots g_{j_r i_r} T^{i_1 \dots i_r} = T_{j_1 \dots j_r}. \tag{2.29}$$

Therefore, the contribution from the co-variant and the contra-variant vector space to the construction of tensors can be assumed to be invariant under the raising and lowering operator.

2.3.3. Series Expansion of Response Function in Tensor Space

In the previous section, we discussed the functional space representation of the non-local response function $\mathbf{R}(\mathbf{k}, k_0)$ in reciprocal space and the potential for non-uniqueness of the auxiliary fields. To characterize the homogeneous medium, it is essential to determine the dispersion relation and the corresponding interface condition. This involves approximating the constitutive relation up to an arbitrary order as in Eq. (2.25) and subsequently

recalculating the effective material parameters, We can write the i^{th} component of the displacement field D as $\mathbf{D}(\mathbf{k}, k_0)$

$$D_i = a_{ij}E_j + b_{ijk}\ k_k E_j + c_{ijkl}k_k k_l E_j + d_{ijklm}\ k_k k_l k_m E_j + \text{H.O.T.} \tag{2.30}$$

It is crucial that the coefficient tensors are associated with an Euclidean space $\mathbb{R}^3$, where each tensor index is represented as a 3-dimensional vector. When using an orthogonal basis, each tensor component belongs to either a complete co-variant tensor space or, through isomorphism, to a contra-variant tensor space that is scaled by the metric tensor $\mathbb{g}$. For example, the first term (a_{ij}) in Eq. (2.30) can be deconstructed in the contra-variant tensor space as $a_{ij} : v^* \otimes v^*$. Similarly, the second term can be represented as $b_{ijk} : v^* \otimes v^* \otimes v^*$, and so on. The purity of the coefficient tensor is crucial for it to remain invariant under all linear transformations. This means that the tensor coefficients must not be a mixed type of (r, s) tensors [*Problem 2.15.1*, [124]].

From a general perspective, each of these tensors can be further described as a sum of their symmetric and anti-symmetric constituents[Chapter 2, [124]], [125] .

Theorem 2.3.1 *A tensor* $\mathbf{T} \in \mathcal{T}$ *is said to be symmetric in its* p^{th} *and* q^{th} *contra-variant indices if the components with respect to the basis remain unchanged when the* p^{th} *and* q^{th} *indices are inter-changed [124].*

Let's take the instance of a tensor of type $(0, 2)$. If T_{pq} is given, it is deemed symmetric if it satisfies the following condition:

$$T_{\sigma(pq)} = T_{pq} \quad . \tag{2.31}$$

Here, σ is a permutation operator chosen from the symmetric group $\mathscr{G}$, which comprises all possible permutations.

Conversely, for the skew-symmetric counterpart, we have the definition:

Theorem 2.3.2 *A tensor* $\mathbf{T} \in \mathcal{T}$ *is anti-symmetric in its* p^{th} *and* q^{th} *contra-variant indices if the components with respect to the basis are scaled by* (-1) *when the* p^{th} *and* q^{th} *indices are inter-changed,* i.e.,

$$T_{\sigma(pq)\ \neq\ pq} = -T_{pq} \quad . \tag{2.32}$$

Both the symmetric and the anti-symmetric tensors are elements of a vector space themselves. Therefore, we can further split the terms in Eq. (2.30) as a sum of their symmetric and anti-symmetric constituents, (written up to $n = 4$ order tensors for readability),

$$R_{ij} = \left(\frac{a_{ij}^{\text{sym}} + a_{ij}^{\text{A-sym}}}{2!} \right) + \left(\frac{b_{ijk}^{\text{sym}} + b_{ijk}^{\text{A-sym}}}{3!} \right) k_k + \left(\frac{c_{ijkl}^{\text{sym}} + c_{ijkl}^{\text{A-sym}}}{4!} \right) k_k k_l \quad , \tag{2.33}$$

which consequently describes the i^{th} component of the $\mathbf{D}$ field as

$$D_i = \left(\frac{a_{ij}^{\text{sym}} + a_{ij}^{\text{A-sym}}}{2!} \right) E_j + \left(\frac{b_{ijk}^{\text{sym}} + b_{ijk}^{\text{A-sym}}}{3!} \right) k_k E_j + \left(\frac{c_{ijkl}^{\text{sym}} + c_{ijkl}^{\text{A-sym}}}{4!} \right) k_k k_l E_j \quad . \tag{2.34}$$

Here, the factor $\frac{1}{n!}$ is the consequence of the symmetrizing/anti-symmetrizing operator that respects the permutation order of the tensor indices [*section 2.16,2.18*, [124]].

According to Casimer-Onsager relations for a reciprocal media, we require that, in the most general sense, the response function satisfies the transposition $R_{ij}(\mathbf{k}, k_0) = R_{ji}(\text{-}\mathbf{k}, k_0)$, for any arbitrary $\mathbf{k}$ and k_0. Additionally, a material that possesses a mirror reflection symmetry along either of its quadrant also restricts the symmetry of the response function, $R_{ij}(\mathbf{k}, k_0) = R_{ji}(\mathbf{k}, k_0)$. This additionally implies the tensor coefficients also follow the symmetries [*Chapter 3*, [58]]

$$\begin{gathered} a_{ij} : symmetric \\ b_{ijk} : Anti - symmetric \\ c_{ijkl} : symmetric \\ d_{ijklm} : Anti - symmetric \end{gathered} \tag{2.35}$$

and analogously for higher-order terms.

Therefore, we can finally reduce Eq. (2.34) into

$$D_i = \frac{1}{2!}\, a_{ij}^{\text{sym}} E_j + \frac{1}{3!}\, b_{ijk}^{\text{A-sym}}\, k_k E_j + \frac{1}{4!}\, c_{ijkl}^{\text{sym}}\, k_k k_l E_j + \ldots \tag{2.36}$$

2.3.4. Tensor Contraction

Before we move into the discussion on the tenor reduction methods, it's important to explain why such a detailed discussion of tensor calculus is necessary [124, 126–128].

Here, our objective is to convert tensors of arbitrary order into their corresponding matrix representations. To achieve this, we must first consider how to handle symmetric and anti-symmetric tensors separately. This is necessary because tensor contraction involves a linear transformation between different basis sets, which may involve adding or removing elements depending on the basis transformation, without changing the tensor rank. In either case, we must ensure that the matrix rank remains unchanged, as its elements are linearly independent, and discarding any of them would result in the loss of information.

2.3.4.1. Anti-Symmetric Tensors: Exterior Algebra and Hodge Star Decomposition

We first define the exterior algebra and the associated Hodge start operator to deal with all the anti-symmetric parts of the tensor coefficient [124, 126, 128] and then later move to describe their symmetric counterpart.

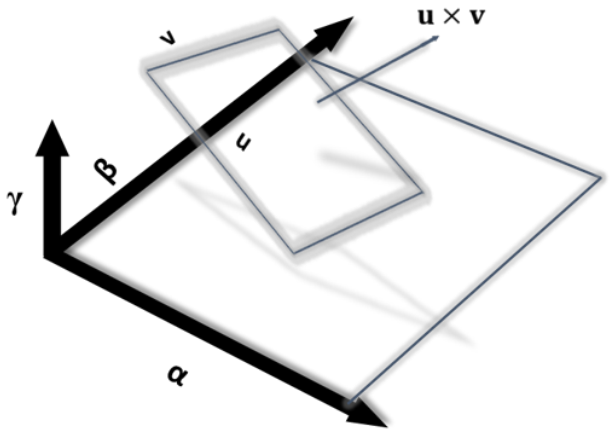

Figure 2.2.: This diagram demonstrates that a flat surface in three-dimensional space ($\mathbb{R}^3$) can be expressed using either two directional vectors (represented as α and β) or a single vector perpendicular to the surface (represented as γ). Essentially, any information that is conveyed by a two-dimensional measure, such as the area of a parallelogram formed by projecting vectors $\mathbf{u}$ and $\mathbf{v}$ onto the surface, can be simplified and represented using a one-dimensional measure given by the cross product of $\mathbf{u}$ and $\mathbf{v}$ with the normal vector γ (i.e., $\gamma(u \times v) = \alpha \wedge \beta(u, v)$).

The set of all anti-symmetric tensors of order $(r, 0)$ (or $(0, s)$) is contained within a subspace called the *exterior algebra*, denoted as $\mathcal{A}$. Subspace constaining the pure tensors are

represented by $\mathcal{A}^r \subset \mathcal{A}$ or $\mathcal{A}_s \subset \mathcal{A}$ resepctively. The algebra that is associated with $\mathcal{A}$ is known as the exterior algebra and is typically denoted by the wedge operator $\wedge$. As a result, the space of anti-symmetric tensors of order $(r, 0)$ is alternatively expressed as $\wedge^r\mathcal{V}$, whereas the anti-symmetric space for $(0, s)$ is written as $\wedge_s\mathcal{V}$. Here, $\mathcal{V}$ refers to the corresponding vector space.

Now that we have established the necessary background, it is appropriate to proceed with the discussion on tensor contraction.

Theorem 2.3.3 *The dimension of $\wedge^r\mathcal{V}$ is the permutation*

$$\binom{d}{r} = \frac{d!}{r!(d-r)!}, \tag{2.37}$$

where $d = \dim(\mathcal{V})$.

For instance, in the case of a $\wedge^2\mathcal{V}$ tensor with indices $\{i, j\}$, we can conclude that even transpositions such as $(1, 2), (1, 3)$, and $(2, 3)$ have even permutation with a positive sign, while odd permutations such as $(2, 1), (3, 1)$, and $(3, 2)$ have the same information as their even permutation but with a negative sign.

Moreover, based on this theorem, it is straightforward to argue that for a 3-dimensional vector space, $\dim(\wedge^0\mathcal{V}) = \dim(\wedge^3\mathcal{V})$, $\dim(\wedge^1\mathcal{V}) = \dim(\wedge^2\mathcal{V})$ and *vice-versa*. This follows from the equivalence relation of

$$\binom{d}{r} = \binom{d}{d-r} \quad , \tag{2.38}$$

expressed by the Hodge star operator ($*$), which is an isomorphism between two spaces of equal dimension [126, 129]:

$$* : \wedge^r\mathcal{V} \to \wedge^{d-r}\mathcal{V} \tag{2.39}$$

The Hodge star operator denoted by "$*$" is a function that maps r vector indices of an anti-symmetric tensor $\wedge^r\mathcal{V}$ to $d - r$ vector indices without changing the dimension of the tensor. This operator defines a one-to-one correspondence between the two spaces, where the original space is referred to as the domain space and the resulting space is called the

Hodge Dual space. Fig. 2.2 depicts an example of the Hodge star operator acting on a space in $\mathbb{R}^3$.

In the special case of having the vector space to be attached with an orthonormal basis set, this Hodge operator additionally forms an isometry, meaning the volume or the determinant action $\langle ., . \rangle$ is also preserved.

Hence, it is possible to conclude that the first-order coefficient of the anti-symmetric tensor, $b_{ijk} \in \wedge^3 V$, can be contracted into a pseudovector $\beta_{il} \in \wedge^0 V$. In other words, we have

$$b_{ijk} \rightarrow \beta_{il}$$

where b and β belong to the 3-D vector space $\mathcal{V}$. It should be noted that β_{il} is a matrix representation of the pseudovector with dummy indices (i, l).

In order to fully apply this knowledge to extract material properties from the tensor coefficients of the response function's series expansion, it is necessary to understand the action of the Hodge operator on a tensor defined in the tangent space $\mathcal{T}_p$ around a point p of the relevant tensor space. This is important because, as mentioned earlier in the constitutive relation for the tensor, the tensor coefficients in Eq. (2.30) have units of length and frequency since they are part of the response function $\mathbf{R}(\mathbf{k}, k_0)$.

Definition 2.3.4 *Given a tanget vector space* T_p *at some point* p*, let us define* $\mathcal{F}^\infty \subset \mathcal{T}_p$ *as the space of linear operator* t *that act on any collection of* $\mathcal{C}^\infty$ *function:*

$$t : \mathcal{F}^\infty \rightarrow \mathbb{R}^n \quad , \tag{2.40}$$

such that for any $f, g \in \mathbf{F}^\infty$ and $a, b \in \mathbb{R}$,

- t is linear: $t(af + bg) = atf + btf$
- t satisfy the product rule, $t(fg) = (tf)g + f(tg)$.

In Euclidean d-space, a tangent vector is simply a set of all derivatives within an orthogonal basis set $\left\{ \frac{\partial}{\partial x_i} \dots \frac{\partial}{\partial x_d} \right\}$, along with their metric tensor $g_{ij} = \left(\langle \frac{\partial}{\partial x_i}, \frac{\partial}{\partial x_j} \rangle \right)$. These quantities are defined for a general d-dimensional vector space $\mathcal{V} = \mathcal{T}_p$ and its dual $\{\mathrm{d}x_i \dots \mathrm{d}x_n\}$, with an inverse metric tensor $g^*_{ij} = \langle \mathrm{d}x_i \, , \mathrm{d}x_j \rangle$ on the dual vector space $\mathcal{V}^* = \mathcal{T}^*_p$.

In this setting, any differential decomposable form $\boldsymbol{\alpha}(\mathrm{d}x_i \dots \mathrm{d}x_r) \in \wedge^{r*}V$ can be expressed as

$$\boldsymbol{\alpha} = \alpha_{i_1 \dots i_r} \mathrm{d}x^{i_1} \wedge \mathrm{d}x^{i_r}$$

Furthermore, the Hodge star operator can be applied to α to obtain a differential form of $(d-r)$ vectors.

$$*(\boldsymbol{\alpha}) = *\Big(\alpha_{i_1 \dots i_r} \mathrm{d}\ x^i \wedge \mathrm{d}x^r\Big) = \frac{\sqrt{|\det[g_{ij}]|}}{r!}\ \alpha^{i_{r+1} \dots i_n} \epsilon_{i_1 \dots i_n} \tag{2.41}$$

It should be noted that the Levi-Civita symbol $\epsilon_{1 \dots d}$ sums over all the vector space and performs a contraction over the repeated indices of the $(d-r)$ terms of the tensor α. While it is possible to apply this tensor contraction, as described in Eq. (2.41), to any tensor α regardless of its permutation symmetry, the resulting tensor is always anti-symmetric. This is due to the Levi-Civita symbol canceling out all but the anti-symmetric part of the tensor. In a 3D Euclidean vector space, the term $|\det[g_{ij}]| = 1$, and can thus be ignored.

Alternatively, the Hodge star operator can also be defined using the inner product of the Hodge dual operator [126]:

Definition 2.3.5 *A Hodge dual of a tensor $\boldsymbol{\zeta} \in \mathcal{T}_p$ whose dual space tensor elements are $*(\boldsymbol{\zeta}) \in \mathcal{T}_p^*$ exist if there exists a real-valued function for some $\boldsymbol{\eta} \in \mathcal{T}_p$ such that,*

$$\boldsymbol{\xi} \wedge *(\boldsymbol{\zeta}) = \langle \boldsymbol{\xi}, \boldsymbol{\zeta} \rangle v \quad , \tag{2.42}$$

where $v = \sqrt{|\det[g_{ij}]|}\ \mathrm{d}x^1 \wedge \dots \wedge \mathrm{d}x^d$ is the unit volume. Integrating this over the whole volume Ω yields an $\mathbf{L}^2$ square integrable inner product form,

$$\int_\Omega \boldsymbol{\xi} \wedge *(\boldsymbol{\zeta}) = \int_\Omega \langle \boldsymbol{\xi} \wedge \boldsymbol{\zeta} \rangle v \quad . \tag{2.43}$$

Now, we can finally reduce our 3rd-order tensor coefficient associated with the first-order field derivative in the series Eq. (2.30), as

$$b_{ijk} k_k E_j = \frac{1}{3!}\ \epsilon_{ljk}\ \beta_{il}\ k_k\ E_j \quad , \tag{2.44}$$

According to Eq. (2.38) the material parameter $\beta_{il} \in \wedge^0 \mathcal{V}$ connects the displacement

field with the first-order gradient of the electric field **E** and is commonly referred to as the chirality term. In the literature, it is represented by the symbol iκ. To simplify the notation, we express the product of the 3$^{\text{rd}}$ order Levi-Civita tensor ϵ_{ljk} and the wave vector component k_k as a curl operator: $\epsilon_{ljk}k_kE_j = (\mathbf{k}\times\mathbf{E})_l = i\omega\mu_0 H_l$. Here we have used the Maxwell's third law corresponding to the Faraday's law of induction.

Based on equation Eq. (2.39), we can make an important observation regarding the application of the Hodge star operator. The relationship between the dimensions d and r is described by equation Eq. (2.38). For instance, in a 3D Euclidean space where $d = 3$, it is not possible to have tensors $T_{i_1\ldots i_r}$ with $r > 3$. In other words, the maximum order of any anti-symmetric tensor in a 3D Euclidean space is limited to three, and tensors of higher order may be either redundant parameters that can be reduced to the chirality term or have no meaningful interpretation. However, to validate this claim, a robust physical explanation is necessary, and this issue remains open for further exploration.

Under the assumption that the second-order gradients are negligible, the i^{th} component of the **D** field can be expressed as:

$$D_i = \varepsilon_{ij}E_j + \left(\frac{1}{3!}\right)\left(\frac{1}{3!}\epsilon_{lkj}\beta_{il}k_kE_j\right) \tag{2.45}$$

with the coefficient of the zeroth order gradient of the electric field mapped to the electric permittivity tensor ε_{ij} and the coefficient of the first order gradient mapped to the chirality β_{il}.

2.3.4.2. Symmetric Tensors: Symmetric Algebra and Symmetric Tensor Decomposition

Symmetric tensor of type $(r, 0)$ (or $(0, s)$) form a subspace $\mathcal{S}$. Subspace constaining the pure tensors are represented by $\mathcal{S}^r \subset \mathcal{S}$ and $\mathcal{S}_s \subset \mathcal{S}$ resepctively. Defining further a symmetrization operation whose action on some tensor **A** of type $(r, 0)$ $\mathbf{A} \to \mathbf{A}_{\text{sym}}$

$$\mathbf{A}_{\text{sym}}(v*,\ldots v*) = \frac{1}{r!}\sum_{i_1,\ldots i_r}\mathbf{A}(v*,\ldots v*) \quad . \tag{2.46}$$

The factor $\frac{1}{r!}$ avoids repetition of symmetric elements in the following equation. Additionally, the dimension of the space of all symmetric tensors $\mathcal{S}$ of type $(r, 0)$ defined over a vector

space $\mathcal{V}^d$ is given by [124],

$$\dim(\mathbf{S}^r) \quad = \begin{pmatrix} d+r-1 \\ r \end{pmatrix}, \text{ and } \quad \dim(\mathbf{S}_s) \quad = \begin{pmatrix} d+s-1 \\ s \end{pmatrix} \quad . \tag{2.47}$$

The aim of this section here is to decompose the symmetric tensor coefficient in Eq. (2.30) into our special curl-based form. To do so, we approach this problem by defining the symmetric rank.

To appreciate the notion of symmetric rank, let us first define a general rank of a tensor. The concept of rank is central to understanding tensors. For a given tensor $\mathbf{A}$ of order r, the rank represents the minimum number of rank-1 tensors that are needed to construct it. The rank of a tensor can be mathematically expressed as

$$\text{rank}(\mathbf{A}) \coloneqq \min\left\{ r | \mathbf{A} = \sum_{i=1}^{r} u_i \otimes y_i \cdots \otimes w_i \right\} \tag{2.48}$$

This rank($\mathbf{A}$), can go higher than the dimension d for orders $r > 2$ [130]. However, for symmetric tensors, a more specialized notion of rank, known as symmetric rank, is used.

Symmetric Rank

Symmetric tensors of order $(r, 0)$ in a basis of $\mathcal{V}^d$ are bijectively mapped to their dual basis in $\mathcal{V}^d$, expressed as a homogeneous polynomial form of degree r and d variables

$$F(x) = \sum_j a_j X^{\mathbf{p}}(j) \quad , \tag{2.49}$$

where $\mathbf{A}_{\text{sym}} = a_{j_i \ldots j_r}$ is the symmetric tensor and $F(x) \in \mathbb{C}[\, x_1 \ldots x_n]$ is a polynomial function on variables $[x]$ in some arbitrary basis in $\mathcal{V}^*$. The multiplicity $\mathbf{p}(j)$ is a non-negative integer counting the symmetric elements in the tensor, with $|\mathbf{p}(j)| = r$. [130, 131]

We focus on the corollary for our analysis. The space of symmetric tensors $\mathcal{S}^r$ and its dual space of polynomials $F(x) \in \mathbb{C}[x_1 \ldots x_n]$ allow the representation of a symmetric tensor as a symmetric outer product of r non-zero rank-1 tensors $v_i \in V$ and weights λ_i where $i = \{1 \ldots r\}$. This is expressed as [132, 133]:

$$\text{rank}_s(\mathbf{A}) \coloneqq \min\left\{ r | \mathbf{A}_{\text{sym}} = \sum_{i=1}^{r} \lambda_i \; v_i \otimes v_i \right\} \quad . \tag{2.50}$$

The symmetric rank of a tensor $\mathbf{A}$ is the minimum number r of linearly independent v_i vectors, where $1 \leq i \leq r$, required to completely decompose $\mathbf{A}_{\text{sym}}$ into a symmetric outer product. In contrast to the generic rank definition, the rank-1 tensors constructing $\mathbf{A}_{\text{sym}}$ must satisfy the additional condition $u_i = y_i = \cdots = w_i = v_i$ for every i.This condition guarantees that $\mathbf{A}_{\text{sym}}$ can be expressed as a symmetric outer product. This is expressed mathematically as

$$\mathbf{A}_{\text{sym}} = \sum_{i=1}^{r} \lambda_i \; v_i \otimes v_i \quad , \tag{2.51}$$

yielding a symmetric rank r.

Moreover, the symmetric rank must strictly follow the condition $\text{rank}_s(\mathbf{A}) = \min(r) < d$, where d is the dimension of the vector space $\mathcal{V}^d$. The vectors in the minimal expression for $\mathbf{A}_{\text{sym}}$ are the principal axes of the tensor and form an orthogonal basis set in $\mathcal{V}^d$. These vectors can be uniquely decomposed using 1-form notation, as shown in Eq. (2.46).

Additionally, In certain cases, the symmetric decomposition of a symmetric tensor can reveal that its rank and symmetric rank are equal. This is true for any $\mathbf{A} \in \mathcal{S}^r$ with $\text{rank}_s(\mathbf{A}) \leq d$ over a closed complex vector field.

Why is this important? Well, the number of unique solutions offered by the dual space representations depends on the rank of the tensors. Therefore, knowing that the rank and symmetric rank are equal can simplify calculations and provide additional insight into the structure of the tensor.

In fact, in [130], a comprehensive analysis of this phenomenon and all possible closed-form solutions is provided. Based on this analysis, it has been shown that when $d = 3$, the upper bound on the generic rank of a symmetric tensor of arbitrary order r is $\text{rank}_s(\mathbf{A}) \leq 3$. This means that any higher-order tensor can be expressed as a polynomial with at most three linearly independent variables.

If the tensor satisfies pairwise linear independence (as in the case of orthonormal basis sets), the restriction becomes even stricter: $\text{rank}_s(\mathbf{A}) = 3$ when $d = 3$. This implies that any higher-order tensors can be expressed as a polynomial with exactly three linearly independent variables.

In summary, this means that for any higher-order tensor, there exists a linear transformation that decomposes the tensor into a matrix.

Using the given information, we can revisit the equation Eq. (2.47), but this time considering r to represent the symmetric rank. Substituting r with the symmetric rank, we get the dimensions of the resulting symmetric tensor as shown below:

$$\binom{d+r-1}{r} = \binom{d+r-1}{d-1} \quad . \tag{2.52}$$

For the case where $d = 3$, this simplifies to

$$\binom{3+r-1}{r} = \binom{2+r}{2} \tag{2.53}$$

which reduces to a new tensor order $r' = d - 1 = 2$ for any symmetric tensor in $d = 3$. This is a significant result, as it implies that any even-ordered symmetric tensor can be reduced to a simple matrix defined in an orthogonal basis set of dimension 2.

Therefore, this new finding provides an avenue to transform even-ordered symmetric tensors into easily manageable matrices defined in a simpler basis set. Next let us discuss the action of a (multi-)linear transformation that facilitates this tensor contraction of the symmetric tensors.

When it comes to symmetric tensors, employing the diagonalization operator is the natural choice. Firstly, diagonalization transforms the tensor $\mathbf{A}$ into a preferred matrix form. This is because the eigenvector associated with the diagonalization operator for a symmetric tensor always forms an orthogonal basis set. And we saw previously that symmetric tensors reduce to their $d - 1$ order when expressed on the orthogonal basis. Thus, the action of the diagonalization operator on a symmetric tensor is equivalent to the tensor contraction as in Eq. (2.52). Also for symmetric matrices, it is possible to choose an orthonormal basis of eigenvectors. This results in the diagonalization being unitary.

Secondly, geometrically, the diagonalization of a symmetric tensor is equivalent to a rotation of the coordinate system in which the tensor is represented. The eigenvectors of the matrix form the new coordinate axes, and the eigenvalues determine the scaling of the new coordinate system along each axis. This geometric interpretation is particularly useful because there is an intrinsic relation between the rotational behaviour of a vector field with the Levi-Civita tensor or the curl operator. See Appendix A for the underlying relation

between Levi-Civita and the rotatio matrix.

Finally, diagonalization is preferred because it results in a diagonal matrix with eigenvalues as the diagonal elements and zero off-diagonal elements, providing a simple and useful representation of the tensor.

Let's clarify the process of diagonalization with the example of a symmetric matrix. In essence, diagonalization involves finding two matrices: a diagonal matrix $\mathbf{D}$ and an invertible matrix $\mathbf{P}$ whose columns are the eigenvectors of the matrix. The diagonal matrix $\mathbf{D}$ contains the corresponding eigenvalues. When we diagonalize a symmetric matrix $\mathbf{B}$ of type $d \times d$, the eigenvectors form an orthonormal basis for the vector space. This implies that the matrix $\mathbf{P}$ is orthogonal, and thus its inverse is simply its transpose, i.e., $\mathbf{P}^{-1} = \mathbf{P}^T$. Therefore, we can write the diagonalization of a symmetric matrix as

$$\mathbf{B} = \mathbf{P}\ \mathbf{D}\ \mathbf{P}^T \quad . \tag{2.54}$$

In the light of *polar decomposition theorem* [*Section 4.2.1*, [134]]: every orthogonal matrix can be written as a product of rotation matrices. Therefore, We can express the diagonalization in terms of rotation operators as

$$\mathbf{B} = \mathbf{P}\ \mathbf{D}\ \mathbf{P}^T = (\mathbf{R}_1 \dots \mathbf{R}_d)\mathbf{D}(\mathbf{R}_1 \dots \mathbf{R}_d)^{\mathrm{T}} \quad . \tag{2.55}$$

As mentioned in the case of anti-symmetric decomposition, in the constitutive relation given by Eq. (2.30), The tensor coefficient in Eq. (2) is a tensor in the tangent space with respect to the orthonormal basis $\left\{\frac{\partial}{\partial x_i} \dots \frac{\partial}{\partial x_d}\right\}$ and the corresponding metric tensor g_{ij}. Similarly, the dual basis $\{\mathrm{d}x_i \dots \mathrm{d}x_d\}$ and the inverse metric tensor g^{ij} are defined on the dual vector space. This tangent basis definition facilitates expressing any linear transformation (basis-transformation) as a combination of Levi-Civita tensors. Thus, attmepting to contract a $(r, 0)$ symmetric tensor $\mathbf{A} \in \mathcal{T}_p$ gives

$$\begin{aligned} &\mathbf{A} = (\mathbf{R}_1 \dots \mathbf{R}_r)\ \boldsymbol{\alpha}\ (\mathbf{R}_1 \dots \mathbf{R}_r)^{\mathrm{T}} \quad , \\ &\quad \updownarrow \\ &\mathbf{A} = (\epsilon_{1\dots r})\ \boldsymbol{\alpha}\ (\epsilon_{1\dots r})^{\mathrm{T}} \quad , \end{aligned} \tag{2.56}$$

At this point, we wish to communicate that the rigorous derivation of the linear transformation, which is represented as a curl operator, remains an unresolved matter and will be a task to tackle in the future.

Through the use of the Levi-Civita symbol and the rotation representation of the linear transformation, we can simplify the expression for the response component associated with the second-order gradient in Euclidean 3-D vector space

$$t_{ijkl}k_k k_l E_j = \epsilon_{nkm}\epsilon_{mlj}\alpha_{in}k_k k_l E_j = k \times \alpha_{in} \times k \tag{2.57}$$

where we have also used the Fourier equivalent form of the definition $\nabla \times \mathbf{E} = (\epsilon_{ijk}\nabla_j E_k)_i$.

A natural extension of the same is possible to higher order tensors as the dimensionality property in Eq. (2.52) holds in general.

It is to be noted that, all these formulations are additionally bound by the Casimer-Onsager relations, and therefore, all even ordered tensor coefficients must hold a *total* symmetry in their indices, meaning [58, 135]:

$$a_{ij} = a_{ji}$$

$$a_{ijkl} = a_{jikl} = a_{ijlk} = a_{klij} = \dots$$

$$\vdots$$

These findings are of significant importance to this thesis for several reasons. Firstly, they provide a new justification for the definition of the curl-based special constitutive relation that was utilized in our prior works [113, 118, 136]. Moreover, each step of this derivation revealed various constraints on both the odd and even ordered tensors. Specifically, both tensors must be an element of the tangent vector space of the orthogonal basis set $\left\{\frac{\partial}{\partial x_i} \dots \frac{\partial}{\partial x_n}\right\}$. This finding further confirms that the tensor coefficients in Equation 2.30 are not dimensionless, as previously speculated [59, 118]. Additionally, by transitioning to the dual space representations of both the symmetric and antisymmetric tensors, these tensor coefficients can be decomposed into dimensionless matrix coefficients representing the effective material parameters, and the Levi-Civita tensors that carry the spatial dimensions (∇_i) in the tangent vector space. While the linear transformation into the dual space

differs in principle for both the symmetric and antisymmetric components, the symmetry arguments, particularly the invariance in the tensor dimension and definition of the inner product among the vectors over the transformations, and the orthogonality of the tangent basis support a well-posed transformation in both cases. It is important to note that the presented derivation is not rigorous; however, the arguments themselves can be proven, which opens up the possibility for further exploration in this area.

Secondly, it is now easy to rewrite the tensor form of the constitutive relations Eq. (2.30) into a more practical form. If we assume a general first-order chiral medium with a non-local correction, then the i^{th} component of the $\mathbf{D}$ field for the response function expanded up to the sixth-order series coefficient can be expressed as:

$$\begin{aligned} D_i =&(\varepsilon_{ij})E_j + \epsilon_{lkj}(\beta_{il})k_k E_j + \epsilon_{nkm}\epsilon_{mlj}(\alpha_{in})k_k k_l E_j + \epsilon_{dkc}\epsilon_{clb}\epsilon_{bma}\epsilon_{anj}(\gamma_{id})k_k k_l k_m k_n E_j \\ &+ \epsilon_{fke}\epsilon_{eld}\epsilon_{dmc}\epsilon_{cnb}\epsilon_{boa}\epsilon_{apj}(\tau_{if})k_k k_l k_m k_n k_o k_p E_j \end{aligned} \tag{2.58}$$

consequently can be written in terms of the respective curl operators in the Fourier domain as

$$\begin{aligned} \mathbf{D}(\mathbf{k}, k_0) = \ & \varepsilon(k_0)\mathbf{E}(\mathbf{k}, k_0) \\ & + \beta(k_0)\ i\ \mathbf{k} \times \mathbf{E}(\mathbf{k}, k_0) \\ & - \mathbf{k} \times \alpha(k_0)\mathbf{k} \times \mathbf{E}(\mathbf{k}, k_0) \\ & + \mathbf{k} \times \mathbf{k} \times \gamma(k_0)\mathbf{k} \times \mathbf{k} \times \mathbf{E}(\mathbf{k}, k_0) \\ & - \mathbf{k} \times \mathbf{k} \times \mathbf{k} \times \tau(k_0)\mathbf{k} \times \mathbf{k} \times \mathbf{k} \times \mathbf{E}(\mathbf{k}, k_0), \end{aligned} \tag{2.59}$$

and as usual $\mathbf{H}(\mathbf{k}, k_0) = \mathbf{B}(\mathbf{k}, k_0)$.

To ease our understanding we have written each term in a dedicated line. The first three terms in this sequence are a consequence of a weak spatial dispersion or weak non-locality. The first term captures the permittivity $\varepsilon(k_0)$ which corresponds to a local electrical response. The second term expresses the magnetoelectric parameter $\beta(k_0)$, a first order $\frac{\Lambda}{\lambda}$ term denoting the coupling between the electric and the magnetic effects in a spatially dispersive medium. An immediate example of non-zero β would be a chiral material. These are material systems that can be engineered by having an array of unit cells that have no

orthogonal mirror symmetries [137–141]. The third term is a magnetic contribution $\alpha(k_0)$, a second order $\left(\frac{\Lambda}{\lambda}\right)^2$ term that carries any form of internal magnetization experienced by the material array. Upon considering the non-uniqueness nature of the displacement field $\mathbf{D}$, a suitable gauge transform can be used to translate the components of α into an effective permeability term:

$$\alpha_{ij}(k_0) = \frac{\mu_{ij}(k_0) - 1}{k_0^2\ \mu_{ij}(k_0)}$$

Finally, here we consider two higher order non-local material parameters $\gamma(k_0)$ from the fourth order spatial dispersion $\left(\frac{\Lambda}{\lambda}\right)^4$ and $\tau(k_0)$ that arise from the sixth order spatial dispersion $\left(\frac{\Lambda}{\lambda}\right)^6$. Care must be taken that the even-ordered tensor coefficients are already diagonalized as a consequence of Eq. (2.57), thus the material parameters ε, μ, γ and τ are diagonal matrices.

With our constitutive relation at hand, we can now proceed to solve the associated dispersion relation and also solve the fields at the interface to obtain the respective optical coefficients for a spatially dispersive homogeneous medium.

3. Dispersion Relation and Interface Condition

In the previous chapter, we explored how non-locality arises in mesoscopic MMs and developed a mathematical expression for it through a phenomenological approach. Our focus was on deriving the unique 'curl' form of the non-local constitutive relation, which is instrumental in describing the optical characteristics of a homogeneous medium. In this chapter, we move forward by discussing the dispersion relation and interface condition for centrosymmetric and chiral MMs. By doing so, we provide a brief overview of the analytical techniques developed to homogenize non-local MMs.

We begin by providing a thorough description of our Maxwell solver. The solver is designed to analyze MMs that have already been homogenized, meaning that their effective material parameters (including frequency dispersion, if applicable) are known. To use our Maxwell solver, one must provide the known effective material parameters (whether local or non-local) as inputs. Once these inputs are provided, the solver uses them to determine the electromagnetic eigenmodes sustained by the given MM by solving the dispersion relations within the homogeneous medium. Furthermore, our Maxwell solver calculates the reflection and transmission coefficient upon illuminating with a plane wave at an interface that separates two half spaces characterized by distinct materials. These optical coefficients play a crucial role in determining the effective properties of the MM.

In this thesis, our focus is on studying the homogenization of MMs, and we consider three different constitutive relations to achieve this. The first is a local model, also known as the weak spatial model (WSD), which is the conventional model containing terms up to the truncation order two in the series defined by Eq. (2.74). This model includes the matrices ϵ, κ, and μ. Moving beyond the WSD model, we consider two strong spatial models (SSD) that incorporate additional non-local parameters. The first is the SSD-γ

model, which adds the non-local parameter γ to the WSD model. The second is the SSD-τ model, which includes the sixth-order non-local material parameter τ in addition to the parameters included in the SSD-γ model.

The solver initiates the study by solving the Helmholtz wave equation in Fourier $\mathbf{k}-$space, utilizing a response $\mathbf{R}(\mathbf{k}, k_0)$ that follows the homogenization model. The Helmholtz wave equation thus reads [*Subsection 4.1*, [118]]

$$\left[\mathbf{k} \times \mathbf{k} \times + \, k_0^2 \mathbf{R}(\mathbf{k}, k_0)\right] \, \mathbf{E}(\mathbf{k}, k_0) = \mathbf{\Phi}(\mathbf{k}, k_0)\mathbf{E}(\mathbf{k}, k_0) = 0, \tag{3.1}$$

which represents the eigenvalue equation whose solutions determine the possible eigenmodes of light excited within the infinitely extended homogeneous medium characterized by the material properties specified in $\mathbf{R}(\mathbf{k}, k_0)$. To ensure non-trivial solutions, the determinant of the wave-operator $\mathbf{\Phi}(\mathbf{k}, k_0)$ is set to zero and the functional dependency of $\mathbf{k}$ and k_0 is found.

Our analysis is focused on two-dimensional scenarios, with the $\hat{\mathrm{z}}$ direction as the principal propagation direction, and the propagation direction is confined to a single plane. The corresponding wave vector component can be $k_y = 0$ or $k_x = 0$, making the wave vector $\mathbf{k} = (k_x, 0, k_z)$ or $\mathbf{k} = (0, k_y, k_z)$, respectively.

Moreover, We concentrate on calculating the dispersion relation solely for the non-local SSD case, as the WSD model can be treated as a special case of the SSD models when the SSD parameters $(\gamma, \tau) \to 0$. We investigate only the fourth order SSD-γ model for the Chiral MM and up to the sixth order SSD-τ model for centrosymmetric MMs. This choice is driven by the increasing polynomial orders of the dispersion relation, leading to higher complexity during solving.

For additional reading, a detailed analysis of the WSD and the SSD-γ models can be found in the references [59, 118].

3.1. Centrosymmetric Metamaterial

Centrosymmetry refers to a point group of material symmetries that exhibits inversion symmetry over every point in the unit cell with respect to some central coordinate [142]. This type of symmetry significantly simplifies the response function, which takes on a symmetric tensor form $R_{ij} = R_{ji}$. As a result, the tensor elements $a_{ij}, b_{ijk}, c_{ijkl}$, and d_{ijklmn} from

the series expansion are also simplified. Furthermore, in the case of centrosymmetry, the optical activity vanishes, i.e., $b_{ijk} = 0$, and this leads to the preservation of the linear polarization of the incident field. Ultimately, the constitutive relations for the SD-τ model, in Fourier spatial domain reads,

$$\begin{aligned}\mathbf{D}(\mathbf{k}, k_0) = \; & \varepsilon(k_0)\mathbf{E}(\mathbf{k}, k_0) - \mathbf{k} \times \alpha(k_0)\mathbf{k} \times \mathbf{E}(\mathbf{k}, k_0) \\ & + \mathbf{k} \times \mathbf{k} \times \gamma(k_0)\mathbf{k} \times \mathbf{k} \times \mathbf{E}(\mathbf{k}, k_0) - \mathbf{k} \times \mathbf{k} \times \mathbf{k} \times \tau(k_0)\mathbf{k} \times \mathbf{k} \times \mathbf{k} \times \mathbf{E}(\mathbf{k}, k_0).\end{aligned} \tag{3.2}$$

All material parameters in the expression above are assumed to be diagonal matrices. In our calculation, we use the matrix form of the curl operator,

$$\mathrm{i}\mathbf{k}\times = \begin{pmatrix} 0 & -k_z & -k_y \\ k_z & 0 & -k_x \\ -k_y & k_x & 0 \end{pmatrix} \tag{3.3}$$

Furthermore, in the subsequent text, all components of the material parameters specified, in general, can vary with frequency. To enhance readability, we exclude the frequency k_0 argument while writing the dispersion relations.

3.1.1. Disperion Relation

When investigating the behavior of waves propagating through a homogeneous medium, the primary objective is to find eigensolutions, which involves conducting a modal analysis. To accomplish this, we need to consider the dispersion relations, which are described by a single equation with three parameters: frequency k_0 and the two components of the wave vector k_x and k_z. However, to solve for the third parameter, usually k_z, we must fix the other two, namely k_0 and k_x. Later when solving the interface problem, we relate the incident field at an incidence angle θ to the dispersion relation of the homogeneous medium through $k_x = k_0 \sin(\theta)$.

When conducting the modal analysis for a medium having inversion symmetry, it is useful to separate the eigenmodes into two distinct categories with well-defined polarization: transverse electric (TE) and transverse magnetic (TM) modes. In the case of TE mode, the electric field is polarized perpendicular to the plane of incidence, while in TM mode the

electric fields are parallel to the plane of incidence. Considering $\hat{z}$ to be the propagation direction for the incident fields,

$$\text{TM}_{(k_x,0,k_z)}\text{-polarization: } \mathbf{E}(\mathbf{k},k_0) = E_x(\mathbf{k},k_0)\,\hat{\text{x}} + E_z(\mathbf{k},k_0)\,\hat{\text{z}} \text{ and } \mathbf{H}(\mathbf{k},k_0) = H_y(\mathbf{k},k_0)\,\hat{\text{y}}$$

$$\text{TE}_{(k_x,0,k_z)}\text{-polarization: } \mathbf{H}(\mathbf{k},k_0) = H_x(\mathbf{k},k_0)\,\hat{\text{x}} + H_z(\mathbf{k},k_0)\,\hat{\text{z}} \text{ and } \mathbf{E}(\mathbf{k},k_0) = E_y(\mathbf{k},k_0)\,\hat{\text{y}}.$$

By introducing the non-local response function $\mathbf{R}(\mathbf{k},k_0)$ from the SSD-τ model into the Helmholtz wave equation Eq. (3.1), the corresponding dispersion relations can be calculated as

$$\begin{aligned}\left[(k_x^2\varepsilon_x + k_z^2\varepsilon_z)\right] - \left[k_0^2\mu_y(k_x^2\gamma_z + k_z^2\gamma_x)(k_x^2\varepsilon_x + k_z^2\varepsilon_z)\right] & \\ -\Big[k_0^2\mu_y(k_x^2+k_z^2)^2\tau_y(k_x^2\varepsilon_x + k_z^2\varepsilon_z)\Big] &= k_0^2\varepsilon_x\varepsilon_z\mu_y, \end{aligned} \tag{3.4}$$

for the $\text{TM}_{(k_x,0,k_y)}$ polarization and,

$$\begin{aligned}\left[(k_x^2\mu_x + k_z^2\mu_z)\right] - \Big[k_0^2\mu_x\mu_z(k_x^2+k_z^2)^2\gamma_y\Big] & \\ -\Big[k_0^2\mu_x\mu_z(k_x^2+k_z^2)^2(k_x^2\tau_z + k_z^2\tau_x)\Big] &= k_0^2\mu_x\mu_z\varepsilon_y, \end{aligned} \tag{3.5}$$

for the $\text{TE}_{(k_x,0,k_y)}$ polarization.

Remark: To enhance clarity, we have organized the terms in the dispersion relation according to their corresponding material parameter. This arrangement makes it easier to perceive the gradual increase in complexity with each homogenization model and better understand the limiting cases. Specifically, the dispersion relation for the SSD-τ model is presented in Equations Eq. (3.4) and Eq. (3.5). As τ approaches zero, the dispersion relation for the fourth order SSD-γ model is obtained as [*Subsection 4.1.3,* [118]]

$$\Big[\Big(k_x^2\varepsilon_x + k_z^2\varepsilon_z\Big)\Big] - \Big[k_0^2\mu_y\Big(k_x^2\gamma_z + k_z^2\gamma_x\Big)\Big(k_x^2\varepsilon_x + k_z^2\varepsilon_z\Big)\Big] = k_0^2\varepsilon_x\varepsilon_z\mu_y, \tag{3.6}$$

$$\Big[\Big(k_x^2\mu_x + k_z^2\mu_z\Big)\Big] - \Big[k_0^2\mu_x\mu_z\Big(k_x^2+k_z^2\Big)^2\gamma_y\Big] = k_0^2\mu_x\mu_z\varepsilon_y, \tag{3.7}$$

for the $\text{TM}_{(k_x,0,k_y)}$ and $\text{TE}_{(k_x,0,k_y)}$ polarizations, respectively. Similarly, assuming both $\gamma,\tau \to 0$ gives the dispersion relation corresponding to the local material laws or the WSD

model:

$$\left(k_x^2\varepsilon_x + k_z^2\varepsilon_z\right) = k_0^2\varepsilon_x\varepsilon_z\mu_y, \tag{3.8}$$

$$\left(k_x^2\mu_x + k_z^2\mu_z\right) = k_0^2\mu_x\mu_z\varepsilon_y, \tag{3.9}$$

for the $\mathrm{TM}_{(k_x,0,k_y)}$ and $\mathrm{TE}_{(k_x,0,k_y)}$ polarizations respectively.

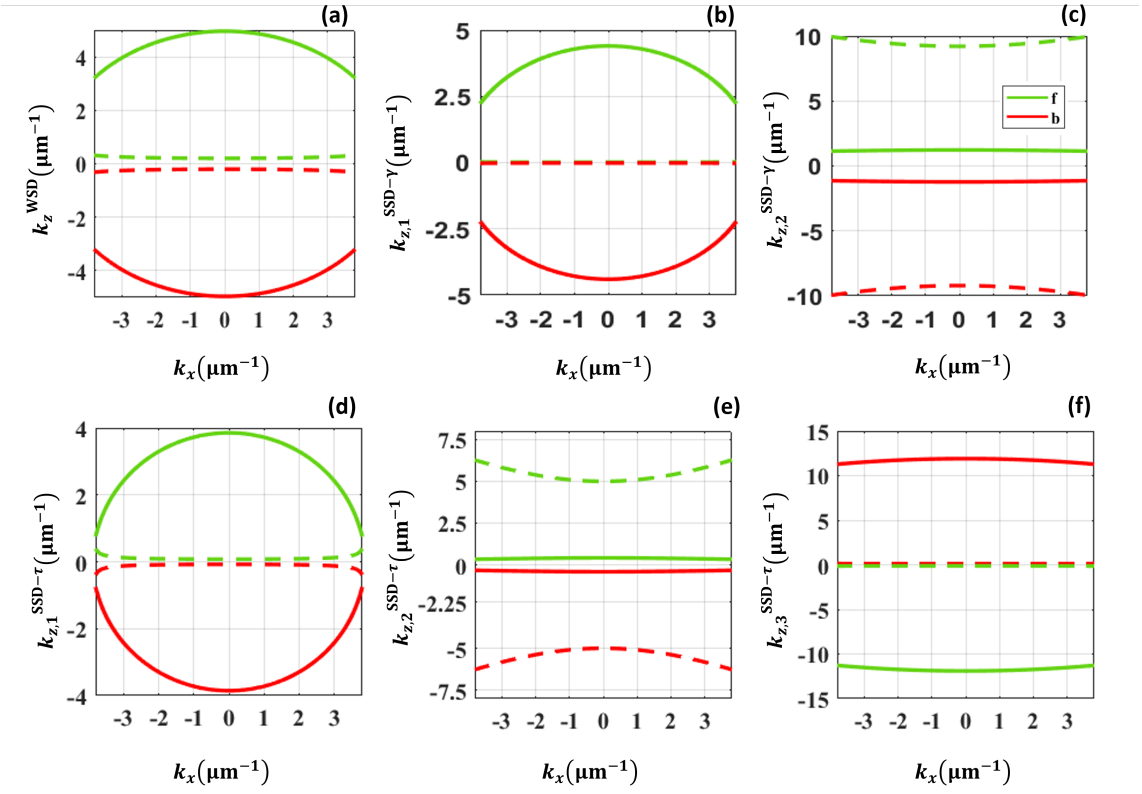

Figure 3.1.: Isofrequency curve depicting the eigenmodes of a specific isotropic homogeneous medium with material parameters $\varepsilon = 1.23 + 0.016\mathrm{i}$, $\mu = 1.26 + 0.118\mathrm{i}$, $\gamma = -0.003 - 0.007\mathrm{i}$, and $\tau = 2.26 \times 10^{-5} + 5.54 \times 10^{-6}\mathrm{i}$. The wave vector k_x takes the range ranging from $-k_0$ to k_0 and the working frequency is $k_0 = 4.2764\,\mu\mathrm{m}^{-1}$. The colors used in the figure represent the forward and backward propagating eigenmodes, which are indicated in the legend. the first sub-figure (a) shows the solution obtained from the WSD model. The solutions from the SSD-γ model are depicted in sub-figures (b) and (c), while sub-figures (d), (e), and (f) represent the solutions from the SSD-τ model.

The dispersion relations written as polynomials show that every order of spatial dispersion in a homogeneous medium excites two extra eigenmodes within the material volume. To ascertain whether the associated eigenmodes are forward or backward propagating, we must analyze the direction of energy flow for each sign of the imaginary part, represented by $\mathrm{Im}\{k_z\}$.

In the WSD model, solving for k_z results in two complex solutions corresponding to forward

or backward propagating modes. Similarly, in the SSD-γ model, solving the fourth-order dispersion relation Eq. (3.6) generates four eigenmodes, two of which propagate forward, and two propagate backward. Additionally, the sixth-order dispersion relation Eq. (3.6) of the SSD-τ model generates six eigenmodes, three of which propagate forward, and three propagate backward. To better understand the eigenmodes supported in a homogeneous medium, we visually represent the eigenvalues (k_z) corresponding to each k_x value calculated for different homogenization models. This representation can be seen in Fig. 3.1.

Care must be taken while solving the dispersion relation as we include higher and higher order non-local terms in Eq. (2.54):

Theorem 3.1.1 *The Abel-Ruffini Theorem: States that there is no radical analytical solution to a general polynomial equation of degree five or higher with arbitrary coefficients [143].*

In other words, there is no general formula for finding the roots of a polynomial equation of degree five or higher that is analogous to the quadratic formula for solving second-degree equations. This is because the solutions to these higher degree equations require taking the square root of negative numbers, such as $\sqrt{-1} = \mathrm{i}$, which cannot be expressed using these operations. As a result, the coefficients of the polynomial equations become indeterminate, and a closed-form solution is not possible.

Therefore, finding analytic roots of the dispersion relations offered by the sixth-order dispersion equation from the SSD-τ model for centrosymmetric systems is limited. Hence, numerical methods are the predominant choice when dealing with higher-order non-local homogenization examples.

For the sake of thoroughness, we have also included in Appendix B.1 the analytical expressions for determining the Poynting vector for both TE and TM polarization. These expressions represent the energy flow in the direction of propagation for both the SSD-γ and SSD-τ models.

3.1.2. Interface Conditions

This section is based on a collaboration with the Institute for Analysis (IANA), Karlsruhe Institute for Technology (KIT), Karlsruhe. Credits for the mathematical rigor and specifically for the generalized formulation of the interface condition that enables one to handle

any number of additional material parameters go to my collaborators Dr. Michael Plum and Dr. Fatima Z. Goffi.

Before we start, we would like to motivate the reader to refer to our previous works [112, 113, 144] for a detailed and rigorous mathematical derivation of the formulation we have borrowed here.

Typically, the continuity of the tangential components of $\mathbf{E}(\mathbf{r}, k_0)$ and $\mathbf{H}(\mathbf{r}, k_0)$ and the normal components of $\mathbf{D}(\mathbf{r}, k_0)$ and $\mathbf{B}(\mathbf{r}, k_0)$ is required at the interface between two local media. This requirement is valid because an equal number of eigenmodes (two for the WSD model) exist on both sides of the interface. However, when spatial dispersion occurs in one of the media, the dispersion relation becomes complicated, and multiple eigenmodes are excited within the non-local material. To maintain balance at the interface, an additional condition is needed.

To establish the additional interface condition, we examine two half-spaces with distinct material properties. Specifically, the upper half-space ($\mathbb{R}^{3,+}$) is a medium subject to the local constitutive law (WSD model) in which the local electric permittivity is $\varepsilon^{\mathrm{loc}}$ and the magnetic permeability is $\mu^{\mathrm{loc}} = 1$. In contrast, the lower half-space ($\mathbb{R}^{3,-}$) is governed by the non-local constitutive law (SSD), characterized by the effective electric permittivity ε and $\mathbb{o}_{n,m}$, which is used to condense all the material parameters that respect spatial dispersion. In this scenario, the constitutive relation in real space can be written up to the $(2N)^{\mathrm{th}}$ order material parameter,

$$\mathbf{D}(\mathbf{r}, k_0) = \begin{cases} \varepsilon^{\mathrm{loc}}\mathbf{E}^{+}(\mathbf{r}, k_0) & \mathbb{R}^{3,+} \\ \varepsilon(k_0)\mathbf{E}^{-}(\mathbf{r}, k_0) + \sum_{n=1}^{N}\sum_{m=0}^{2n}(\nabla\times)^{m}\mathbb{o}_{n,m}(k_0)(\nabla\times)^{(2n-m)}\mathbf{E}^{-}(\mathbf{r}, k_0) & \mathbb{R}^{3,-}. \end{cases} \tag{3.10}$$

By substituting this constitutive relation into the Helmholtz wave equation

$$\nabla \times \nabla \times \mathbf{E}(\mathbf{r}, k_0) - k_0^2\mathbf{D}(\mathbf{r}, k_0), \tag{3.11}$$

the electric field $\mathbf{E}^{\pm} \coloneqq \mathbf{E}\,|_{\mathbb{R}^{3,\pm}}$ can be understood as the generalized solution of the wave

equation when,

$$\nabla \times \nabla \times \mathbf{E}^{+}(\mathbf{r}, k_0) = k_0^2 \varepsilon^{\text{loc}} \mathbf{E}^{+}(\mathbf{r}, k_0) \qquad \mathbb{R}^{3,+},$$

$$\nabla \times \nabla \times \mathbf{E}^{-}(\mathbf{r}, k_0) = k_0^2 \Big(\varepsilon(k_0) + \textstyle\sum_{n=1}^{N} \sum_{m=0}^{2n} (\nabla\times)^m \mathbb{o}_{n,m}(k_0) (\nabla\times)^{(2n-m)} \Big) \mathbf{E}^{-}(\mathbf{r}, k_0) \quad \mathbb{R}^{3,-}. \tag{3.12}$$

Here, the electric fields $\mathbf{E}^{\pm}$ are required to satisfy certain smoothness conditions as discussed in [113].

It is important to note that the non-local constitutive relation governing the second half space $\mathbb{R}^{3,-}$, as expressed in Eq. (3.10), is the most comprehensive representation that includes all possible combinations of the curl operator and the material coefficients, totaling $\{N(N+1)+1\}$ terms.

However, the constitutive relations must adhere to the Casimir-Onsager condition [59, 116].This requires an equal number of Curl operators on each side of the material coefficient $\mathbb{o}_{n,m}$ (as discussed in Section 2.4.2). This simplifies the constitutive relation, reducing the number of terms to only $N+1$, and expresses Eq. (3.10) in the form of Eq. (2.74). To achieve this, we write the constitutive relation for the second half space $\mathbb{R}^{3,-}$ up to the $(2N)^{\text{th}}$ spatial dispersion order as follows:

$$\mathbf{D}(\mathbf{r}, k_0) = \varepsilon(k_0) \mathbf{E}^{-}(\mathbf{r}, k_0) + \Big\{ \textstyle\sum_{n=1}^{N} \sum_{m=0}^{2n} (\nabla\times)^m \mathbb{o}_{n,m}(k_0) (\nabla\times)^{(2n-m)} \delta_{n,m} \Big\} \mathbf{E}^{-}(\mathbf{r}, k_0), \tag{3.13}$$

where $\delta_{m,n}$ is the two variable Kronecker delta ($\delta_{m,n} = 1$ when $m = n$ and 0 otherwise) that facilitates the contraction.

Please note, throughout this section, we assume that all field quantities have the argument $(\mathbf{r}, k_0)$. Therefore for the sake of readability, we omit writing them explicitly in the following.

Generalized Interface Condition

This study considers two half-spaces, as shown in Fig. 3.2. The local medium is represented by $\mathbb{R}^{3,+}$, while the non-local medium is represented by its counter, $\mathbb{R}^{3,-}$. The interface between these two half-spaces is denoted by $\Gamma = \mathbb{R}^{3,+} \cap \mathbb{R}^{3,-}$, and is located at $z = 0$ in the zx plane.

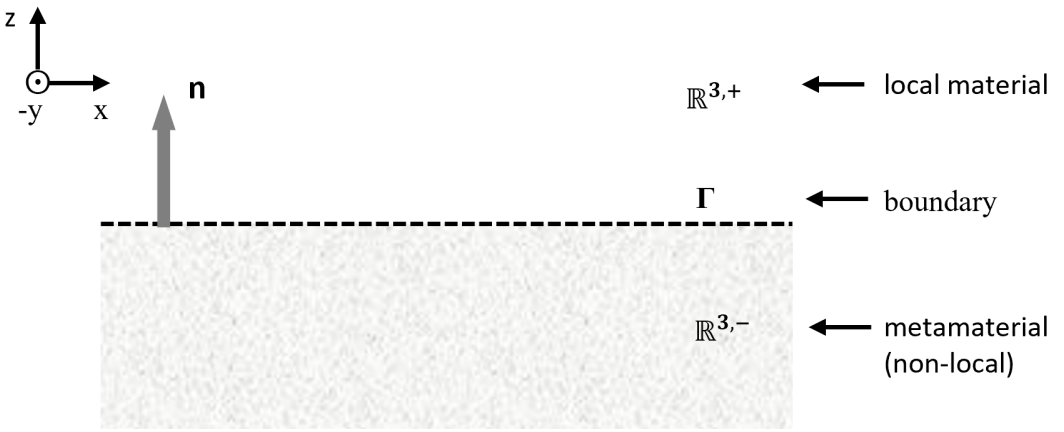

Figure 3.2.: The figure depicts the region in which light propagates, where the upper half-space is filled with a homogeneous local medium and the lower half-space is filled with a metamaterial (MM). The surface that separates the two half-spaces is represented by the symbol Γ. The normal vector $\mathbf{n}$ is directed outward from the homogenized metamaterial.

The interface condition at Γ for the generalized solution $\mathbf{E}$ satisfying Eq. (3.12) can be written in terms of the normal vector $\mathbf{n}$ to Γ, as discussed in [113],

$$\left(\mathbf{E}^{+} - \mathbf{E}^{-}\right) \times \mathbf{n} = 0,$$

$$\delta_{k,0}\left(\nabla \times \mathbf{E}^{+} - \nabla \times \mathbf{E}^{-}\right) \times \mathbf{n} + \mathbb{L}_k \mathbf{E}^{-} \times \mathbf{n} = 0. \tag{3.14}$$

Here, the surface operator $\mathbb{L}_k$ for $k \in \{0, \ldots, 2N-1\}$ is an operator that acts on $\mathbf{E}^{-}$ as

$$\mathbb{L}_k \mathbf{E}^{-} = k_0^2 \sum_{n=\lceil \frac{k+1}{2} \rceil}^{N} \sum_{m=k+1}^{2n} (\nabla\times)^{m-(k+1)} \mathbb{c}_{n,m}(k_0) (\nabla\times)^{2n-m}\, \mathbf{E}^{-}, \tag{3.15}$$

We recall that $\lceil . \rceil$ is the ceiling operator that maps $x \in \mathbb{R}$ to the next integer greater than or equal to x. A general derivation of the expressions in Eq. (3.14) can be found in appendix (C.1).

Some clarifications are needed at this stage. It should be noted that the $2N+1$ equations in Eq. (3.15) may not be entirely independent, as some of them could reduce to $0 = 0$ if certain matrices $\alpha_{m,n}$ are zero. Thus, the total number of independent interface conditions given by Eq. (3.15) is at most $2N+1$. By imposing the constraints from Eq. (2.74) and Eq. (3.13) on the interface conditions, we can reduce the number of independent interface conditions to at most $N+1$, which is less than $2N+1$. Therefore, we can express the

operator $\mathbb{L}_k$ now with the added $\delta_{n,m}$ as.

$$\mathbb{L}_k\mathbf{E}^- = k_0^2 \sum_{n=\lceil\frac{k+1}{2}\rceil}^{N} \sum_{m=k+1}^{2n} (\nabla\times)^{m-(k+1)} \mathbb{o}_{n,m}(k_0)(\nabla\times)^{2n-m}\delta_{n,m}\ \mathbf{E}^- \ , \tag{3.16}$$

for $k \in \{0,\ldots,2N-1\}$. Therefore, we can now set $N=3$ $(2N=6)$ to yield the interface condition relevant for the SSD-τ model,

$$\Big(\mathbf{E}^+ - \mathbf{E}^-\Big)\times\mathbf{n} = 0, \quad \text{(IC 1)}$$

$$\begin{aligned}\Big(\nabla\times\mathbf{E}^+ - \nabla\times\mathbf{E}^-\Big)\times\mathbf{n} + k_0^2(\alpha(k_0)\nabla\times\mathbf{E}^-)\times\mathbf{n} \\ +k_0^2(\nabla\times\gamma(k_0)\nabla\times\nabla\times\mathbf{E}^-)\times\mathbf{n} + k_0^2(\nabla\times\nabla\times\tau(k_0)\nabla\times\nabla\times\nabla\times\mathbf{E}^-)\times\mathbf{n} = 0,\end{aligned} \quad \text{(IC 2)}$$

$$(\gamma(k_0)\nabla\times\nabla\times\mathbf{E}^-)\times\mathbf{n} + (\nabla\times\tau(k_0)\nabla\times\nabla\times\nabla\times\mathbf{E}^-)\times\mathbf{n} = 0, \quad \text{(IC 3)}$$

$$(\tau(k_0)\nabla\times\nabla\times\nabla\times\mathbf{E}^-)\times\mathbf{n} = 0. \quad \text{(IC 4)}$$

This formulation can be interpreted physically. The first interface condition, Eq. (IC 1), expresses the well-known principle that the tangential component of the electric field must be continuous across the interface Γ. The second condition, Eq. (IC 2), reveals the discontinuity in the $\mathbf{H}$ field caused by the spatial dispersion. As γ and τ approach zero, Eq. (IC 2) approaches the standard continuity condition for the tangential component of $\mathbf{H}$,

$$\begin{aligned}\Big(\nabla\times\mathbf{E}^+ - \Big\{\mathbb{1} - k_0^2\alpha(k_0)\Big\}\nabla\times\mathbf{E}^-\Big)\times\mathbf{n} \implies \Big(\mathbf{B}^+ - \mu^{-1}(k_0)\nabla\times\mathbf{B}^-\Big)\times\mathbf{n} = 0 \\ \Big(\mathbf{H}^+ - \mathbf{H}^-\Big)\times\mathbf{n} = 0.\end{aligned} \tag{3.17}$$

Here, we have once again used the transformation $\mu_{ij}(k_0) = \frac{1}{1-k_0^2\ \alpha_{ij}(k_0)}$.

Furthermore, Eq. (IC 3) and Eq. (IC 4) are the additional conditions required by the tangential components of the eigenmodes excited purely by spatial dispersion. Recall that as the order of spatial dispersion increases, one forward and one backward propagating eigenmode are excited in the homogeneous construct of the MM medium. Therefore, the total electric field $\mathbf{E}^-(\mathbf{r},k_0)$ within the homogeneous medium is a superposition of n eigenmodes, where n is an even number representing the spatial dispersion order. considering

each eigenmode has a propagation constant k_{z_i}, we can write

$$\mathbf{E}^{-}(\mathbf{r}, k_0) = \sum_{i}^{n/2} \mathbf{E}^{\mathrm{f}}_{0,i}(\mathbf{r}, k_0) e^{\mathrm{i}\mathbf{k}_i \cdot \mathbf{r}} + \mathbf{E}^{\mathrm{b}}_{0,i}(\mathbf{r}, k_0) e^{-\mathrm{i}\mathbf{k}_i \cdot \mathbf{r}}, \tag{3.18}$$

where $\mathbf{E}^{\mathrm{f/b}}_{0,i}$ is the amplitude vector, the labels {f,b} represent the forward and backward propagating modes corresponding to the sign of the $\mathrm{Im}\{k_z\}$, within the MM. Therefore, for each additional order of spatial dispersion, there is one extra interface condition.

Once again, the interface conditions for the WSD and the SSD-γ models can be immediately studied by simply setting the respective material parameters in Eq. (IC 1)-Eq. (IC 4) to zero. *i.e.,* the interface condition for SSD-γ model is simply Eq. (IC 1)-Eq. (IC 4) with $\tau \to 0$ and the standard interface condition discussed in the literature for the WSD model is the case when $\{\tau, \gamma\} \to 0$.

By utilizing the information obtained from the dispersion relation and associated interface conditions, we can formulate the Fresnel expressions. In the later part of this chapter, we will detail the Fresnel equations, covering their derivation, and finally, calculate the complete set of optical coefficients at an interface. This amounts to calculating the amplitudes of all the transmitted and reflected modes for a given amplitude of some plane wave used to illuminate the interface.

3.2. Chiral Metamaterial

Chirality refers to a geometric property that characterizes the asymmetry in the structure of materials. An object is considered chiral if it cannot be superimposed onto its mirror image, known as its enantiomer, by any translation or rotation. Chirality plays a crucial role in chemistry, specifically in pharmaceuticals because most pharmaceutical molecules are developed as enantiomers and therefore have vastly different biological activities due to differences in their interaction with enzymes and receptors in the body. The challenge in working with chiral molecules lies in their characterization, as both enantiomers have identical physical properties and are difficult to distinguish from each other. Nevertheless, various efficient measuring techniques have been developed over time. [145–148].

This section aims to investigate the possibility of utilizing effective medium theory as a viable technique to characterize the material properties of a medium that contains multiple chiral molecules. This characterization is essential in gaining insight into the medium's

optical response, making it a crucial step in understanding the potential applications of chiral molecules in optical devices. We provide a brief introduction to the Condon-Tellegen constitutive relation, which serves as the weak spatial dispersion model for chiral materials. The dispersion relation resulting from this model can effectively describe the fundamental propagating modes of a chiral metamaterial. Additionally, we extend our model to the non-local scenario by introducing the $\gamma(k_0)$ parameter into the Condon-Tellegen form of the constitutive relation. We discuss the potential variations in the dispersion relation that may arise as a result. We also briefly address the necessary interface conditions for both the WSD and the SSD models.

It is important to note that we present a comprehensive analytical formulation for using effective medium theory on a non-local chiral metamaterial. However, we leave the numerical analysis as an open question for further research.

3.2.1. Condon-Tellegen Constitutive Relation

The Condon-Tellegen form of the constitutive relation discusses the magneto-electric coupling in a material due to spatial dispersion [149]. Considering a reciprocal chiral medium, the constitutive relations read,

$$\begin{aligned}\mathbf{D}(\mathbf{r},k_0) &= \varepsilon(k_0)\mathbf{E}(\mathbf{r},k_0) + \mathrm{i}\kappa(k_0)\mathbf{H}(\mathbf{r},k_0),\\ \mathbf{B}(\mathbf{r},k_0) &= \mu(k_0)\mathbf{H}(\mathbf{r},k_0) - \mathrm{i}\kappa(k_0)\mathbf{E}(\mathbf{r},k_0),\end{aligned} \tag{3.19}$$

where the material parameters ε is the permittivity matrix, κ is the chirality parameter and μ is the magnetic permeability term.

Under weak spatial dispersion, we can set the $\mathbf{Q}$ field as

$$\mathbf{Q} = \frac{\mathrm{i}}{k_0}\Big(\Big(\mathbb{1} - \mu^{-1}(k_0)\Big)\nabla\times\mathbf{E} - \mathrm{i}\kappa(k_0)\ \mu^{-1}(k_0)\mathbf{E}\Big) \quad . \tag{3.20}$$

Using Equation (1.2), we can express all the material tensors on the electric displacement

field, as given by [150],

$$\begin{aligned}\mathbf{D}(\mathbf{r},k_0) &= \tilde{\varepsilon}(k_0)\mathbf{E}(\mathbf{r},k_0) + \mathrm{i}\tilde{\kappa}(k_0)\nabla\times\mathbf{E}(\mathbf{r},k_0)\\ &\quad + \nabla\times\left(\frac{\mu(k_0)-\mathbb{1}}{k_0^2}\right)\,\mu(k_0)^{-1}\nabla\times\mathbf{E}(\mathbf{r},k_0),\ \text{and}\\ \mathbf{B}(\mathbf{r},k_0) &= \mathbf{H}(\mathbf{r},k_0)\quad .\end{aligned} \tag{3.21}$$

Here, the transformed set of material parameters are expressed as

$$\tilde{\varepsilon}(k_0) = \left(\varepsilon(k_0) - \kappa^2(k_0)\;\mu^{-1}(k_0)\right)\ \text{ and }\quad \tilde{\kappa}(k_0) = \left(\tfrac{2}{k_0}\;\kappa(k_0)\;\mu^{-1}(k_0)\right). \tag{3.22}$$

This form of the material parameters significantly simplifies the achiral-chiral interface conditions [70], which will be further discussed in this thesis.

The first approach involves designing the unit cell to have no reflection symmetry, as demonstrated in various studies [151–154]. Alternatively, one can introduce materials that are naturally chiral as the constituting material of the unit cell or the surrounding matrix medium [155–161].

In such chiral metamaterial structures, Optical activity is generally considered to be a first-order effect, proportional to $\frac{\Lambda}{\lambda}$. However, to account for strong spatial dispersion effects beyond the long wavelength limit, the non-local parameter $\gamma(k_0)$ can be added to the constitutive relations given in Eq. (3.21). This results in new constitutive relations that can be expressed up to the fourth order in real-space notation

$$\begin{aligned}\mathbf{D}(\mathbf{r},k_0) =& \tilde{\varepsilon}(k_0)\mathbf{E}(\mathbf{r},k_0) + \mathrm{i}\tilde{\kappa}(k_0)\nabla\times\mathbf{E}(\mathbf{r},k_0) + \nabla\times\left(\frac{\mu(k_0)-\mathbb{1}}{k_0^2}\right)\,\mu(k_0)^{-1}\nabla\times\mathbf{E}(\mathbf{r},k_0)\\ &+ \nabla\times\nabla\times\gamma(k_0)\nabla\times\nabla\times\mathbf{E}(\mathbf{r},k_0),\ \text{and}\\ \mathbf{B}(\mathbf{r},k_0) =& \mathbf{H}(\mathbf{r},k_0)\quad .\end{aligned} \tag{3.23}$$

In the above equations, it is assumed that the homogeneous medium is always aligned along the optical axis, resulting in the effective material tensors being diagonal. Once again to ensure readability, we have chosen to leave out the frequency k_0 argument in the following subsection while presenting the dispersion relations for these material parameters.

3.2.2. Disperion Relation

To find the eigenmodes excited in the non-local chiral MM, we solve the Helmholtz wave equation Eq. (3.1) with the response function making up the non-local constitutive relation Eq. (3.23). The corresponding dispersion relation is an eight-order polynomial equation written explicitly here,

$$\begin{aligned}
&\left\{\left[k_x^2\tilde{\varepsilon}_x + k_z^2\tilde{\varepsilon}_z - k_0^2\tilde{\varepsilon}_x\tilde{\varepsilon}_z\mu_y\right] - \left[k_0^2\mu_y\Big(k_x^2\gamma_z + k_z^2\gamma_x\Big)\Big(k_x^2\tilde{\varepsilon}_x + k_z^2\tilde{\varepsilon}_z\Big)\right]\right\} \\
&\left\{\left[k_x^2\mu_x + k_z^2\mu_z - k_0^2\mu_x\mu_z\tilde{\varepsilon}_y\right] - \left[k_0^2\mu_x\mu_z\Big(k_x^2 + k_z^2\Big)^2\gamma_y\right]\right\} \\
&+ k_0^4\tilde{\kappa}_y\mu_x\mu_y\mu_z\Big(k_z^2\tilde{\varepsilon}_z\tilde{\kappa}_x + k_x^2\tilde{\varepsilon}_x\tilde{\kappa}_z\Big) = 0
\end{aligned} \tag{3.24}$$

Here, once again we stick to the definition of the material tensors from Eq. (3.22). Additionally, we group the terms in a way that, it is easy to distinguish the influence of each material parameter on the polynomial. As of before, the Able-Ruffini theorem suggests that we must rely on a fully numerical method to solve the polynomial since Eq. (3.24) is an eight-order polynomial.

Once again, setting the non-local contribution to a zero function, $\gamma \to 0$, we get back the standard dispersion relation corresponding to Eq. (3.21) for a local-chiral medium,

$$\begin{aligned}
&\Big(k_x^2\tilde{\varepsilon}_x + k_z^2\tilde{\varepsilon}_z - k_0^2\tilde{\varepsilon}_x\tilde{\varepsilon}_z\mu_y\Big)\Big(k_x^2\mu_x + k_z^2\mu_z - k_0^2\mu_x\mu_z\tilde{\varepsilon}_y\Big) \\
&\qquad + k_0^4\tilde{\kappa}_y\mu_x\mu_y\mu_z\Big(k_z^2\tilde{\varepsilon}_z\tilde{\kappa}_x + k_x^2\tilde{\varepsilon}_x\tilde{\kappa}_z\Big) = 0.
\end{aligned} \tag{3.25}$$

It is important to make a brief note of the eigenmodes excited in a chiral medium. The response of a chiral anisotropic medium depends on the handedness of the eigenmodes. As a result, the eigenmodes excited in the homogeneous chiral medium can be classified as right circularly polarized (RCP) for $\tilde{\kappa} > 0$ or left circularly polarized (LCP) for $\tilde{\kappa} < 0$ [162, 163].

3.2.3. Interface Conditions

This section is based on the formulations developed by Elias Kunzweiler in his Bachelor thesis "Homogenization of chiral Metamaterials" at the Institute of Theoretical solid state

physics (TFP), Karlsruhe Institute of Technology. I also would like to thank Dr.Fatima Z. Goffi from the Institute of Analysis (IANA), Karlsruhe Institute of Technology, for her contribution during the derivation of the interface conditions.

From the constitutive relations for a chiral metamaterial in Eq. (3.21) and Eq. (3.23), we can infer that $\tilde{\kappa}$ is a local term and only weakly contributes to the spatial effects. As a result, an interface containing a chiral medium doesn't require any additional interface condition if non-local chirality terms are absent [70]. Thus, with the above information, we can express the interface condition in a general form similar to the centrosymmetric case, as given by Eq. (3.14), but with the inclusion of a chirality term as

$$\begin{aligned} \Big(\mathbf{E}^+ - \mathbf{E}^-\Big) \times \mathrm{n} &= 0, \\ \delta_{k,0}\Big(\nabla \times \mathbf{E}^+ - \nabla \times \mathbf{E}^-\Big) \times \mathrm{n} + \Big(k_0^2\ \mathrm{i}\ \tilde{\kappa}(k_0)\ \mathbf{E}^-\Big) \times \mathrm{n} + \mathbb{L}_k \mathbf{E}^- \times \mathrm{n} &= 0, \end{aligned} \tag{3.26}$$

for $k \in \{0, \ldots, 2N-1\}$.Please refer to Appendix (C.1) for a detailed derivation of these interface conditions.

Assuming the SSD in the MM is governed by the SSD-γ model with $2N = 4$, we can rewrite the interface conditions derived in Section 3.1.2 to include the additional chirality term.

$$\Big(\mathbf{E}^+ - \mathbf{E}^-\Big) \times \mathrm{n} = 0 \quad \text{(c-IC 1)}$$

$$\begin{aligned} \Big(\nabla \times \mathbf{E}^+ - \nabla \times \mathbf{E}^-\Big) \times \mathrm{n} + k_0^2(\mathrm{i}\ \tilde{\kappa}(k_0)\ \mathbf{E}^-) \times \mathrm{n} + k_0^2(\alpha(k_0)\nabla \times \mathbf{E}^-) \times \mathrm{n} & \\ + k_0^2(\nabla \times \gamma(k_0)\nabla \times \nabla \times \mathbf{E}^-) \times \mathrm{n} &= 0 \end{aligned} \quad \text{(c-IC 2)}$$

$$(\gamma(k_0)\nabla \times \nabla \times \mathbf{E}^-) \times \mathrm{n} = 0 \quad \text{(c-IC 3)}$$

Once again the relation $\mu_{ij}(k_0) = \frac{1}{1-k_0^2\ \alpha_{ij}(k_0)}$ has been used.

3.3. Fresnel Equations

When electromagnetic waves move from one material to another, they undergo changes in their amplitude and phase due to differences in the material properties of the two media. If the two materials have different polynomial dispersion relations, the electric and magnetic fields in each medium can be expressed as a combination of eigenmodes with distinct

amplitudes and phases. At the interface between the two materials, the interface conditions determine how to identify the amplitude of each mode that is excited by the incoming wave.

To calculate the amplitudes of the reflected and transmitted waves, it is necessary to match the amplitudes of these modes with those of the incident wave at the interface. This requires solving the interface conditions for the amplitudes of all the involved modes, using the interface conditions described earlier. Once the amplitudes of the modes are known, the power carried by the reflected and transmitted waves can be calculated.

For the derivation of the Fresnel expressions and the corresponding reflection and transmission coefficient for both centrosymmetric and chiral MM, see appendix (B) and appendix (C.1), respectively.

In the following chapter, we will delve into the homogenization process in detail and provide a step-by-step explanation of how to assign effective material parameters to the homogeneous equivalent of a MM. This is a critical step in accurately analyzing the optical properties of the MM and utilizing our Maxwell solver effectively.

4. Results and Discussion

In the preceding chapters, we have proposed models to homogenize non-local metamaterials and discussed the theory of the non-local constitutive relations and the associated interface conditions. Each model prescribes a given set of effective material parameters necessary to capture the strong interaction within the material. The above set of formulation promises to describe the associated wave properties, from the given dispersion relations, and to calculate the accurate reflection and transmission coefficients of plane waves at metamaterial interfaces and entire slabs as a function of frequency and incidence angle. In this chapter, we outline our computations in which we assign effective material parameters to the homogeneous equivalent to the actual structrue. In the course of this chapter, we also introduce a Maxwell solver that takes the mesoscopic spatial distribution of an actual material, as a function of frequency and the lattice constants as input to predict the associated wave properties of the eigenmodes within the material domain.

Furthermore, we also introduce the alternative $\mathbf{T}_{\text{eff}}$-matrix approach that calculates the excited effective material parameters from a complete effective (induced) multipolar description of the entire MM within the homogenizable limit for the considered range of frequencies. As will be discussed, this approach has the ability to isolate the material response from lattice effects. . This promises a clear advantage over other existing methods. To highlight these special features, We show the numerical results for the homogenization of a 3D metamaterial made from gold nanoparticles. Further, we upstep by employing the homogeneous counterpart of the gold nanoparticles to construct a novel lattice that illustrates the practicality of the material's properties for reuse.

4.1. Computational Setup and Simulation

In this section, we describe how the analytical framework for non-local homogenization introduced in the previous chapter is computationally implemented to actually retrieve

effective material parameters of selected metamaterials in following sections. The accuracy of the parameter retrieval method is validated using numerical simulations of the actual MM.

4.1.1. Parameter Retrieval Method

Computational optimization procedures in mathematical analysis rely on numerical approximation as the foundation. The goal is to find approximate solutions that accurately predict the behavior of a system based on an existing quantitative theory. As computational power has advanced, the complexity of mathematical models used in this field has also increased, enabling the development of highly accurate models that have transformed the fields of science and engineering [164, 165].

In the context of homogenization, the focus is on deriving a set of effective material parameters for a given target structure using the models presented in this work, such that the resulting optical response matches the target spectrum. Here, this referential target spectrum is always obtained from a full wave analysis of the actual metamterial. This requires to solve the inverse problem from the perspective of the effective medium. Therefore, instead of calculating the optical response of a structure, e.g. a slab, made from a homogeneous material made from a mateial characterized by a certain set of constitutive parameters, the inverse problem needs to be solved. We are asked to determine the effective constitutive parameters that lead to a particular optical response. Essentially, this requires minimizing the difference between the target spectrum and the one obtained using our models by adjusting the actual material parameters for a given constitutive relation, which can be formulated as a nonlinear least-squares problem.

To compute the target data, computational simulation tools are utilized to conduct numerical experiments actual metamaterial structure. The outgoing field information obtained from these simulations is then compared with a prescribed homogenization model to complete the optical characterization, replacing experimentally measured data. In this thesis, simple geometries with known T-matrices are considered from which complex reflection ($\mathbf{R}^{\mathrm{data}}$) and transmission ($\mathbf{T}^{\mathrm{data}}$) spectra are calculated over a range of incidence angles, serving as the target spectrum for the optimization procedure.

To achieve this goal of numerical homogenization, a two-stage retrieval algorithm has been developed, which comprises a forward Maxwell solver and an optimization engine.

The forward solver is designed to evaluate the general constitutive relations and interface conditions for a material represented by a homogenization model. To operate, the solver requires several input parameters, such as effective material parameters, the thickness of the slab being examined, the frequency spectrum (k_0) relevant to the problem being addressed, and a set of wave vectors specified for the polarization of the incident field. The solver employs this information to compute the dispersion relation Eq (3.1), and the associated eigenmodes for the specified homogenization model.

Assuming the thickness of the homogeneous slab to be one lattice period, the solver obtains information on all excited Bloch modes within the material domain corresponding and the corresponding interface conditions, similar to the procedure explianed in *Subsection* 3.1.2. Using this information, complex reflection ($\mathbf{R}^{\text{model}}$) and transmission ($\mathbf{T}^{\text{model}}$)coefficients are computed as a function of k_0 and the wave vector, k_x. Here, the superscript denotes the type of homogenization model employed. This approach is particularly applicable in the context of a thin film or a 2D MM.

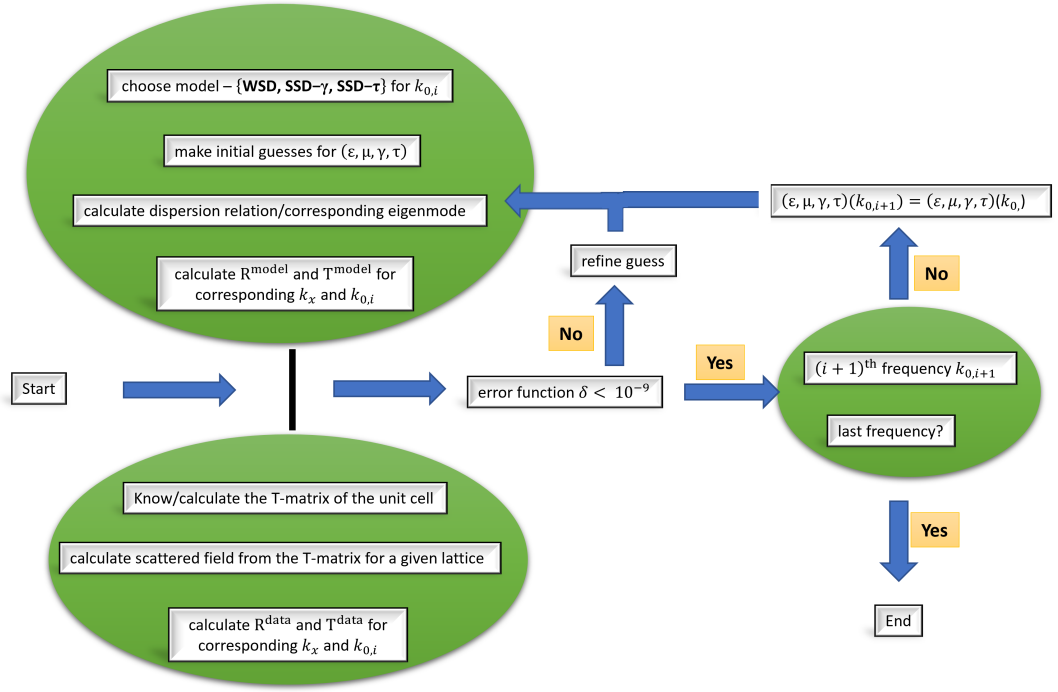

Figure 4.1.: This flow chart depicts the optimization procedure associated with the Maxwell solver, which optimizes the relevant material parameters and calculates the reflection and transmission coefficient as a function of both frequency and incidence angle for the prescribed homogenization model.

Next, the optimization algorithm starts with an initial guess of the model parameters at an initial frequency $k_{0,i}$ and iteratively adjusts them until the distance (loss function: $\mathbb{L}(\mathfrak{e})$)

between the predicted and target values of the reflection and transmission coefficients is minimized. In each iteration of k_0, the algorithm computes the gradient of the loss function with respect to the model parameters, and the corresponding residuals are introduced into a least square solver as implemented in SciPy [166] with a smooth loss function:

$$\mathbb{L}(\mathbb{e}) = 2\left(\sqrt{1+\mathbb{e}} - 1\right), \tag{4.1}$$

whose L^2 norm $\|\mathbb{L}\|_2$ is minimized. In Eq. (4.1) we have the residual vector $\mathbb{e}$ that measures the distance between the observed data and the predicted values at each data point as

$$\begin{aligned}\mathbb{e} = &|\mathbf{R}^{\mathrm{data}}(k_0, k_x) - \mathbf{R}^{\mathrm{model}}(k_0, k_x)|^2 \\ &+ |\mathbf{T}^{\mathrm{data}}(k_0, k_x) - \mathbf{T}^{\mathrm{model}}(k_0, k_x)|^2.\end{aligned} \tag{4.2}$$

Additionally, to measure the overall quality of the fit between the observed data and the model predictions for a given frequency point, we define an error function $\delta(k_0)$:

$$\begin{aligned}\delta(k_0) = \sum_{k_x} \Big(&|\mathbf{R}^{\mathrm{data}}(k_0, k_x) - \mathbf{R}^{\mathrm{model}}(k_0, k_x)|^2 \\ &+ |\mathbf{T}^{\mathrm{data}}(k_0, k_x) - \mathbf{T}^{\mathrm{model}}(k_0, k_x)|^2\Big)\end{aligned} \tag{4.3}$$

that compares the optical coefficients, *i.e.* reflection $\mathbf{R}^{\mathrm{data}}$ and transmission $\mathbf{T}^{\mathrm{data}}$, of the actual MM with the predictions from each model.

The forward solver is implemented using JAX [167] to enable both JIT-compilation as well as automatic differentiation. Automatic differentiation provides fast and precise Jacobians to the optimization, resulting in quick convergence and high-quality results. The algorithm allows for multiple restarts, where the fitting procedure is repeated from different initial guesses until a sufficiently small final error is achieved. However, it is often found that a single trial is sufficient for many problems, and no additional restarts are required.

The optimization process continues until the convergence criteria are satisfied, and the optimal parameters are obtained. Once a set of material parameters for a particular $k_{0,i}$ is found, the optimization proceeds to the next closest $k_{0,i+1}$, depending on the discretization. To ensure a smooth constitutive relation and improve convergence, the optimized material parameters from the previous iteration serve as the initial guess for the current $k_{0,i+1}$. This procedure is repeated for all $k_{0,i}$, resulting in the final constitutive relation for all material

TM-Polarization		TE-Polarization	
$(k_x, 0, k_z)$	$(0, k_y, k_z)$	$(k_x, 0, k_z)$	$(0, k_y, k_z)$
ε_{xx}	ε_{yy}	ε_{yy}	ε_{xx}
ε_{zz}	ε_{zz}	μ_{xx}	μ_{zz}
μ_{yy}	μ_{xx}	μ_{zz}	μ_{zz}
γ_{xx}	γ_{yy}	γ_{yy}	γ_{xx}
γ_{zz}	γ_{zz}	$--$	$--$
τ_{yy}	τ_{xx}	τ_{xx}	τ_{zz}
$--$	$--$	τ_{zz}	τ_{zz}

Table 4.1.: The table lists the relevant material parameters that couple to light based on the polarization and incidence plane

parameters considered. (*i.e.*, the procedure is the same for all models discussed herein). This approach also allows us to optimize and fine-tune the optical response from the models by evaluating the material behavior under different input conditions. The algorithm is represented as a flowchart in Figure 4.1.

In the present context, homogenization can be understood as the optimal mapping between heterogeneous MM and the effective material parameters that can predict the optical properties of the actual heterogeneous medium with minimal deviation.

Although the focus of this thesis is on homogenizing thin films, it is important to note that this methodology can be generalized to effectively homogenize a 3D anisotropic metamaterials. To retrieve all entries of the anisotropic material tensors, it is crucial to consider all possible illumination directions and polarizations. The four combinations of transverse magnetic (TM) and transverse electric (TE) modes and wavevectors (k_x, k_y) have to be analyzed, and the corresponding material parameters for each case are calculated. The corresponding combinations of material parameters are given in Table 4.1. Notably, the nonlocal parameter γ behaves similarly to the permittivity ε, while the parameter τ behaves similarly to the permeability parameter μ.

Now that the retrieval is introduced, we need to know how to numerically obtain the target reflection and transmission coefficients $\mathbf{R}^{\text{data}}$ and $\mathbf{T}^{\text{data}}$ from a periodic metamaterial slab. In this work, we have not access to experimental data.

4.1.2. Numerical Experiment Using the T-Matrix Method

We aim to demonstrate the practicality of our homogenization models by studying a metamaterial (MM) composed of regularly spaced spherical scatterers with a predetermined multipolar response. To analyze the MM, we investigate three different MMs, each consisting of meta-atoms with increasing complexities of supported multipole moments. To design the meta-atoms and compute the electromagnetic response of the MM, we utilize the transition matrix formalism (T-matrix) method. This method describes the scattering properties of the meta-atoms using a matrix known as the T-matrix, which linearly relates the vector containing the expansion coefficient of the incident fields $\mathbf{q}$ (with the coefficients $\mathbf{q}^{\mathrm{e}}$ and q^{m} for the electric and magnetic contributions, respectively) and the vector containing the scattered fields $\mathbf{p}$ (with the coefficients p^{e} and $\mathbf{p}^{\mathrm{m}}$ for the electric and magnetic contributions, respectively). The coefficients contained in $\mathbf{p}$ and $\mathbf{q}$ are a fundamental solution to the vector Helmholtz equations both of which are expanded in a vector spherical harmonic basis. The relationship between the two is expressed as

$$\mathbf{p} = \mathbf{T} \cdot \mathbf{q}. \tag{4.4}$$

By using the T-matrix, the scattered field of the meta-atom can be calculated for any given incident field. The T-matrix approach has been extensively studied in literature [168–170].

To calculate the complete scattering response of a MM, we use the algorithm described in Ref. [171]. This algorithm assumes that the MM is composed of identical copies of a meta-atom with a 2D periodicity, and uses the translational addition theorem to apply the T-matrix to the meta-atom. This approach enables the use of the 2D Ewald summation method, which leads to a rapidly converging solution for determining the scattering response of the MM [172]. The outcome of the algorithm is a set of reflection and transmission coefficients for the MM under a given illumination condition.

The choice of a spherical scatterer in this article is made for convenience, as the T-matrix can describe any unit cell regardless of its shape or material. Spherical particles are also commonly used in Mie theory because they provide a convenient way to describe the scattering behavior of small particles [173, 174]. The Mie coefficients, which describe the scattering of light by a spherical particle, can be calculated analytically for a wide range of particle sizes and frequencies. This makes it relatively easy to model the behavior of a

large number of identical particles, as is often the case in metamaterials.

Mie theory provides a means to express the ratio between the scattered and incident fields using the Mie coefficients a_n and b_n, which correspond to the electric and magnetic contributions, respectively, for a given multipolar order n [174]. Consequently, the T-matrix can also be defined in terms of these Mie coefficients, making this a convenient approach for design. Additionally, this approach allows for the polarizabilities of an isotropic particle to be related to the Mie coefficients [175],

$$a_n = \frac{k^3}{6\pi \mathrm{i}} \alpha_n^{\mathrm{e}}(\omega) \tag{4.5}$$

$$b_n = \frac{k^3}{6\pi \mathrm{i}} \alpha_n^{\mathrm{m}}(\omega). \tag{4.6}$$

Here, $\alpha_n^{\mathrm{e}}(\omega)$ and $\alpha_n^{\mathrm{m}}(\omega)$ are the corresponding polarizabilities for the n^{th} multipolar order.

In addition to spherical symmetry, polarizability in Mie theory calculations is frequently assumed to have a Lorentzian dispersion. Such an assumption on a Lorentzian dispesion provides a relatively simple and accurate way to describe the behavior of small particles in response to electromagnetic fields in spectral proximity to a resonance. Such a resonance can be particle plasmon polariton in the case of a small metallic nanoparticle or any other resonance in the structure. The polarizability is a complex number that describes the response of a particle to an oscillating electric field. It takes into account both the particle's size and its resonance frequency, which determines how easily the particle can be polarized by the electric field.

We can now establish the scattering characteristics of our meta-atom with a polarizability $\alpha_n^{\mathrm{e/m}}$ that is based on a Lorentzian-type oscillator. This can be expressed as:

$$\alpha_n^{\mathrm{e/m}}(\omega) = \frac{\alpha_{0n}^{\mathrm{e/m}}}{(\omega_0^2)_n^{\mathrm{e/m}} - \omega^2 - \mathrm{i}\omega\sigma_{0n}^{\mathrm{e/m}}}, \tag{4.7}$$

where $\omega_0 = k_0$ is the resonance frequency of the oscillator, $\alpha_{0n}^{\mathrm{e/m}}$ is the oscillator strength, and $\sigma_{0n}^{\mathrm{e/m}}$ is the associated Ohmic loss with the dimension of inverse time. The labels $\{\mathrm{e/m}\}$ refer to the electric and magnetic contribution and $n = \{\mathrm{d}, \mathrm{q}, \dots\}$ to the multipolar order.

In this way, we can incorporate pre-determined Lorentzian polarizabilities of individual

nanospheres into the T-matrix that defines the scattering behavior of a single sphere. For example, below is the T-matrix of size 6×6 describing pure electric and magnetic dipolar sphere at some frequency ω:

$$\mathbf{T} = \begin{pmatrix} a_1 & 0 & 0 & 0 & 0 & 0 \\ 0 & a_1 & 0 & 0 & 0 & 0 \\ 0 & 0 & a_1 & 0 & 0 & 0 \\ 0 & 0 & 0 & b_1 & 0 & 0 \\ 0 & 0 & 0 & 0 & b_1 & 0 \\ 0 & 0 & 0 & 0 & 0 & b_1 \end{pmatrix}. \tag{4.8}$$

The choice of spherical symmetry for the meta-atoms further simplifies the T-Matrix to have only diagonal entries. This method can be adapted to include arbitrarily higher multipolar orders – limited only by the available computational resources – by simply adding the corresponding Mie coefficients to the diagonal.

Using the T-matrix approach, we construct a square array of spherical scatterers with a periodicity of Λ. The scatterers are arranged freely, and the corresponding reflection ($\mathbf{R}^{\text{data}}$) and transmission ($\mathbf{T}^{\text{data}}$) coefficients are determined for all frequencies ω when the array is illuminated by a plane wave with a TM polarization. The incident angle of the plane wave is adjusted by modifying the x-component of the wave vector k_x of the incident field. These reflection and transmission coefficients constitute the reference data that is subsequently utilized in the parameter retrieval analysis.

4.2. Investigation of Non-Local Isotropic Metamaterials

In this section of the thesis, we will homogenize an isotropic array of spherical scatterers. The section is divided into four subsections. The first three subsections focus on analyzing metamaterials (MM) made from scatterers that sustain either an electric dipole, electric quadrupole, or both an electric dipole and an electric quadrupole moments, as well as a magnetic dipole moment. We apply local and non-local constitutive relations to homogenize each metamaterial and assess their efficacy by employing the error function described in Eq. (4.3).. Our analysis provides new insights into the physical relevance of effective material parameters and their relationship with the multipolar order of the meta-atom and the periodicity of the lattice. We also determine the optimal order of the Taylor expansion

for the constitutive relation to homogenize a MM composed of scatterers with a complex multipolar response.

In the latter subsection, we conduct a more systematic study to quantify the improvement in the predictions of optical coefficients resulting from a non-local MM. While the benefits of using non-local constitutive relations have been established in prior research, only a limited number of examples have been studied so far [65, 176]. Moreover, accurately determining the improvement resulting from varying the typical length scale relative to the wavelength has proven challenging. Analyzing exact structures like fishnet material or simpler metamaterials such as spheres on a cubical lattice is difficult due to changes in geometry affecting the entire optical response of the unit cell. Therefore, we aim to investigate the possibility of homogenizing the potentially simplest metamaterial [177, 178], electric dipolar lattice, using both local and non-local constitutive relations when the period tends to be comparable to the wavelength.

In addition to the superiority of the SSD models at longer lattice periods, We also observe a surprising breakdown of the ability to homogenize the metamaterial at shorter periodicity. This unexpected failure occurs when energy is transported across the lattice due to a well-pronounced near-field interaction among the particles forming the lattice. This suggests that the period should not just be much smaller than the operational wavelength to homogenize a metamaterial, but for a given size of the inclusion, there is an optimal period.

All the results for the isotropic homogeneous medium are obtained using the parametric fitting procedure outlined in Section 4.1.1 and a suitable homogenization model from *Chapter 3*. Our analysis shows that by examining the homogenized arrays, we can gain insights into their behavior and identify their key properties. Through this analysis, we seek to gain a better understanding of these structure's behavior and advance our knowledge of the relationship between geometry and optical response. The pictorial representation of the general homogenization idea can be found in Fig. 4.2. Nevertheless, it is important to note that the techniques used and the corresponding insights drawn from this study can be applied to any mesoscopic centrosymmetric slab structures, regardless of the scatterer's shape [179–181].

It should be noted that the results presented in this section of the thesis have already been published in Ref. [182]. I would like to express my gratitude to Yannick Augenstein for his

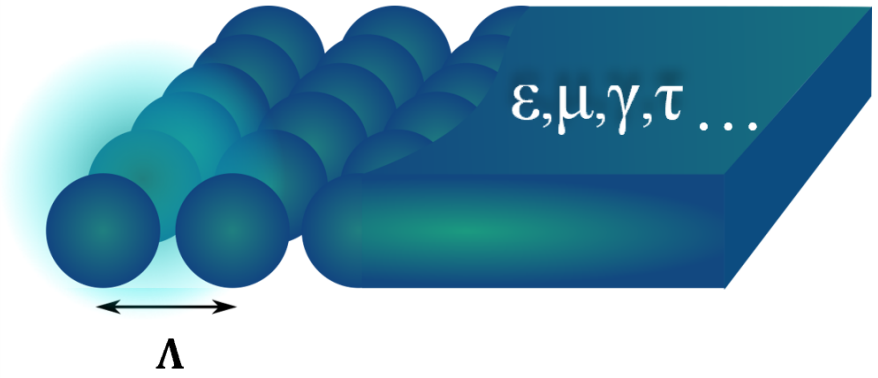

Figure 4.2.: This figure shows the transition from an inhomogeneous metamaterial, of peridicity Λ, to an optically equivalent homogeneous slab described with effective material parameters ε, μ, γ, τ, etc., up to an arbitrary order. An optical excitation, illustrated by the blue-colored cloud, emanates from the spheres but spreads across the entire MM. It is used to indicate a long-range interaction among the constituting scatterers.

.

valuable contributions and discussions that aided in the development of the optimization algorithm utilized in this section of the thesis.

Please note, the findings and insights highlighted in the following three subsections of the thesis have been previously reported in [182]

4.2.1. Pure Electric Dipolar Scatterer

To model the actual metamaterial (MM), we utilized the technique outlined in Section 4.1.2. Our initial example involves a MM constructed from a sphere, modeled as a pure electric dipole in air. The polarizability of this sphere is described by a resonance frequency of $\left(k^e_{0_d}\right)_{\text{iso}} = 6.823\,\mu\text{m}^{-1}$, an oscillator strength of $\alpha_{0^e_q} = 0.5 \times \left(6\pi\sqrt{2}c_0\right)$, and an Ohmic loss factor of $\sigma_{0^e_d} = 0.1\,\text{THz}$. The characteristic polarizability is displayed in Fig. 4.3(a). The MM is made by arranging this sphere periodically along the XY-plane with a periodicity of $\Lambda = 300\,\text{nm}$. After utilizing the approach outlined in Section 4.1.2 to determine the referential optical coefficients $\mathbf{R}^{\text{data}}$ and $\mathbf{T}^{\text{data}}$ as a function of frequency (k_0) and incidence angle (θ), we proceed to initiate the homogenization procedure through implementation of the parameter retrieval technique detailed in Section 4.1.1.

To put it in simpler terms, the objective of this study is to assess the ability of all three homogenization models, WSD,SSD-γ and SSD-τ, to accurately predict the reflection and transmission coefficients as compared to the actual metamaterial. This is done by evaluating the error function Eq. (4.3) as a qualitative measure. *i.e.,* the homogenization model that

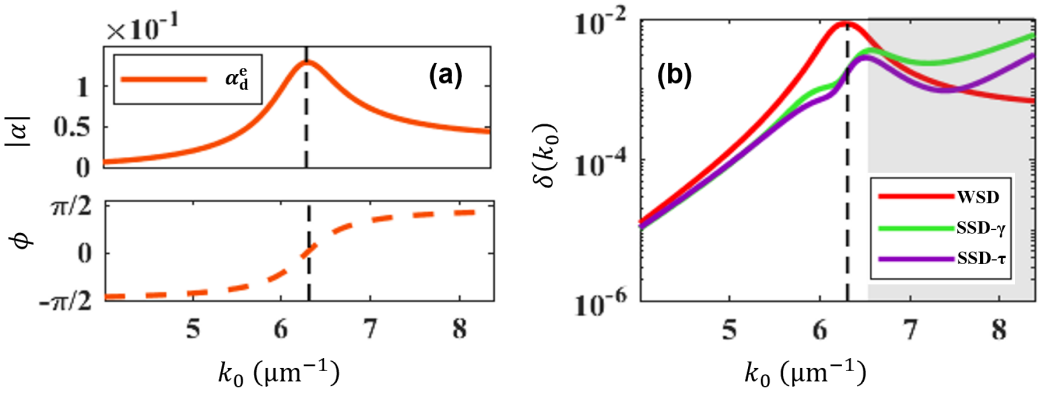

Figure 4.3.: (a) The magnitude and phase of the electric dipolar polarizability are depicted for the first example. (b) The error function is plotted in logarithmic scale and as a function of the frequency that was considered when homogenizing the MM at a lattice with a period of $\Lambda = 300$ nm. Three different models, the WSD model (red), SSD-γ model (green), and SSD-τ model (violet), are used to homogenize the MM. The error function indicates the accuracy of the homogenization. The frequency domain where homogenization may not be entirely reliable due to significant anisotropy is indicated by the shaded gray region. The Lorentzian resonance at frequency $\left(k^e_{0_d}\right)_{\text{iso}} = 6.823\,\mu\text{m}^{-1}$ for the isolated particle is represented by the black dashed line.

produces the smallest error function value is considered to have the most accurate prediction.

Fig. 4.3 (b) gives the corresponding results for the electric dipole example. The dashed line indicates the resonance frequency of the isolated sphere as $\left(k^e_{0_d}\right)_{\text{iso}}$. The shaded region beyond $\left(k^e_{0_d}\right)_{\text{iso}}$ indicates frequencies where the system is less isotropic due to symmetry breaking in the third dimension and thus difficult to homogenize. This is a consequence of using a single-layer mesoscopic metamaterial instead of a stacked version, which causes a significant difference between the effective material parameters in the normal direction and those in the transverse directions. As a precaution, we examine the T-matrix of the complete MM, as discussed in the works [183] and require identical Mie coefficients in the $\{x, y, z\}$ directions across the frequency spectrum k_0 for an expected isotropic structure. If any deviations from isotropy are observed, the corresponding frequencies are excluded from the analysis.

We begin by analyzing the considered MM using the WSD model. The results presented in Fig. 4.3 (b) indicate that the WSD model exhibits larger errors as compared to both SSD models, across all frequencies that permit homogenization. Particularly, as we approach the resonance frequency, we observe a significant increase in the error. This is an anticipated outcome because the resonance leads to a spread of excitation throughout the lattice, indicating a pronounced non-local behavior. The non-local behavior caused by resonance

cannot be captured by a local constitutive relation. Therefore, the SSD model is investigated at the considered frequency range.

As shown in Figure 4.3 (b), homogenizing with either the SSD-γ model (green curve) or the SSD-τ model (violet curve) results in the same value for the error function. This suggests that a fourth-order homogenization model is sufficient for accurately predicting the optical properties of the studied metamaterial, and thus there is no need to use higher-order spatial dispersion.

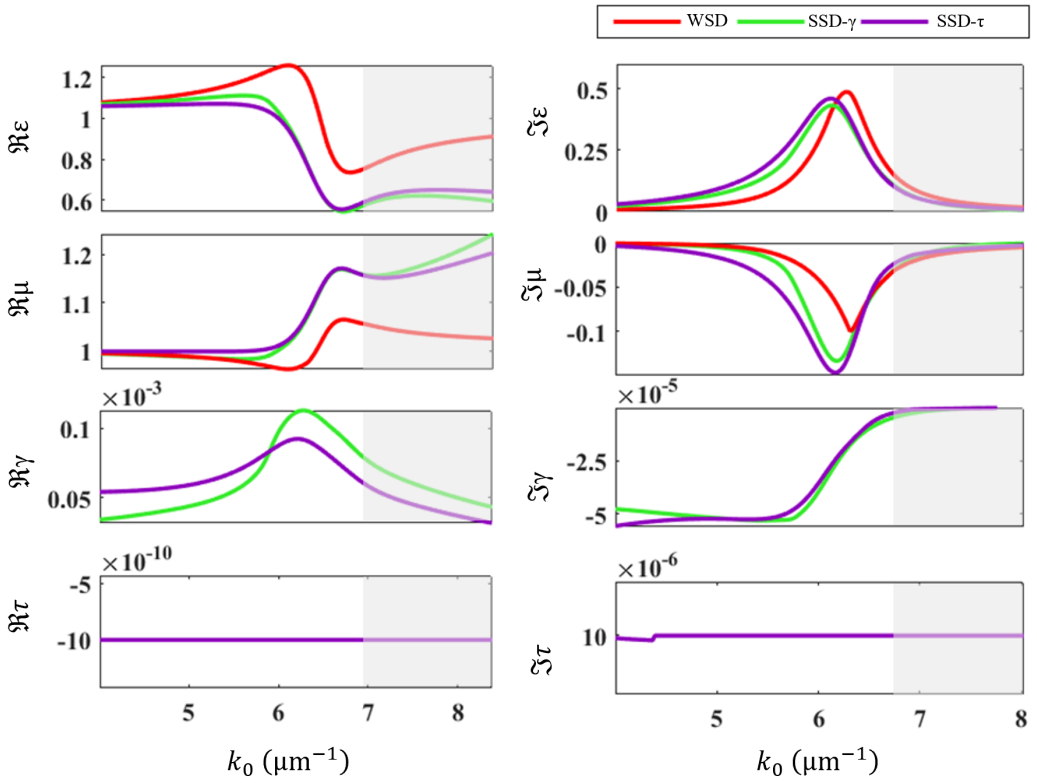

Figure 4.4.: The figure shows the effective material parameters obtained using the WSD-γ model (in red), the SSD-γ model (in green), and the SSD-τ model (in violet) plotted as a function of frequency k_0, for a mesoscopic metamaterial composed of a periodic array of spheres exhibiting an electric dipole response. The gray shaded area corresponds to a frequency range where the homogenization process is not entirely reliable due to the emergence of strong anisotropy in the system.

To delve deeper into this matter, we will examine the real and imaginary components of the effective material parameters, as presented in Fig. 4.4. It's important to note that the parameteric space for $\Im\varepsilon$ was confined to positive real numbers to maintain passivity.

At first glance, we notice that all the three homogenization models exhibit a Lorentzian resonance in the electric permittivity ε. This aligns well with the Lorentzian characteristics of the electric dipolar resonance demonstrated by the meta-atom in Fig. 4.3(a). Additionally,

we also note the presence of a faint anti-resonance in the permeability μ. Despite some variations in magnitude between the WSD and SSD models, the dispersion in these material parameters remains qualitatively consistent across all three constitutive relations.

In addition, we found that adding the non-local terms γ and τ to the constitutive relation has little effect on the local parameters ε and μ. However, as shown in Fig. 4.3(b), employing the SSD models in the homogenization process improves the accuracy of the optical response. This indicates that any non-local effects present in this MM are fully represented only by the additional eigenmodes that are excited in the homogeneous equivalent medium when using a non-local term in the constitutive relation, as discussed in Chapter 3.

Moreover, looking at the material parameters obtained from the SSD-τ model, we can observe an insignificant τ parameter that does not affect the optical coefficients. Despite the algorithmic retrieval procedure resulting in non-zero τ values, there is no observable impact on the reflection and transmssion coefficients, as observed from Fig. 4.3(b). Therefore, the inclusion of the τ parameter is unnecessary, and the SSD-γ model is sufficient for capturing the lattice interactions among the dipolar meta-atoms. This finding is consistent with the results depicted in Fig. 4.3(b), where the SSD-γ model (green curve) and the SSD-τ model (violet curve) perform equally well in homogenizing the metamaterial. The error function is almost identical when the metamaterial is homogenized with either of the two constitutive relations.

To some extent, the results for this simple system are expected. However, to gain deeper insights into the performance of the homogenization models, we need to test their effectiveness on more complex systems. Thus, we will consider individual scatterers with higher multipolar orders to increase the system's complexity and evaluate the effectiveness of the homogenization models.

4.2.2. Pure Electric Quadrupolar Scatterer

To push the limits of the SSD-γ model, we analyze a system consisting solely of electric quadrupolar (EQ) scatterers. Previous research has shown that the magnetic permeability tensor of periodic systems is significantly influenced by an increase in the quadrupolar excitation [184–188]. As a result, higher-order spatial derivatives of the electric field tensor are required for a complete description of the response of the periodic system.

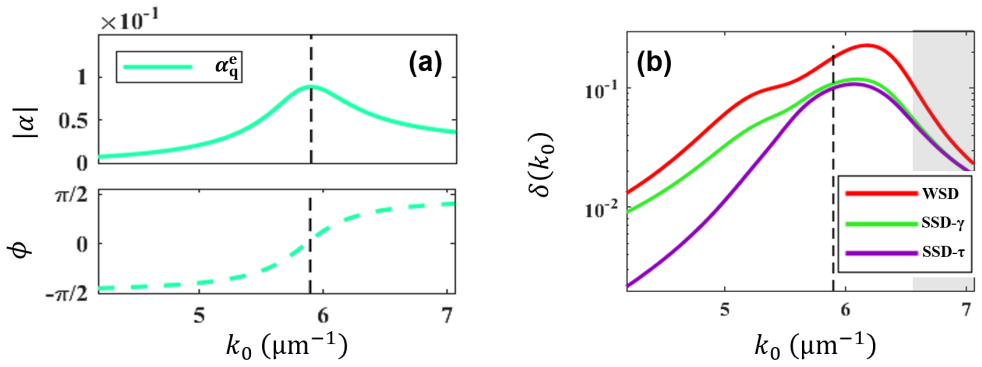

Figure 4.5.: (a) The magnitude and phase of the electric quadrupolar polarizability are depicted (b) The error function is plotted in logarithmic scale and as a function of the frequency that was considered when homogenizing the MM at a lattice with a period of $\Lambda = 300$ nm. The homogenization is performed using the WSD model (red), the SSD-γ model (green), and the SSD-τ model (violet). The frequency domain where homogenization may not be entirely reliable due to significant anisotropy is indicated by the shaded gray region. The Lorentzian resonance at frequency $\left(k^e_{0_q}\right)_{\text{iso}} = 5.89\,\mu\text{m}^{-1}$ for the isolated particle is represented by the black dashed line.

To explore this scenario, we consider a spherical scatterer as before with a polarizability (α^e_q) having a resonant frequency at $\left(k^e_{0_q}\right)_{\text{iso}} = 5.89\,\mu\text{m}^{-1}$, oscillator strength of $\alpha^e_{0_q} = 0.35 \times \left(6\pi\sqrt{2}c_0\right)$, and an Ohmic loss factor of $\sigma^e_{0_q} = 0.1\,\text{THz}$. The characteristic polarizability is displayed in Fig. 4.5 (a). To describe the polarizability of the isolated particle, we create the T-matrix using the angular momentum basis. The Mie coefficients (a_q) that correspond to α^e_q can be found in the matrix components with angular momentum $j = 2$, while the dipolar components $(j = 1)$ are excluded by setting them to zero. The corresponding MM has a periodicity of $\Lambda = 300\,\text{nm}$.

In Fig. 4.5 (b), we have plotted the error function as a function of frequency on a logarithmic scale. Our discussion now focuses on the performance of the WSD model. It is evident that the WSD model performs poorly compared to the SSD models. Comparing to the previously discsussed electric dipole example, the error for the WSD model is one order of magnitude higher across the entire frequency range. The poor performance of the WSD model can be attributed to the high amplitude of the pure EQ contribution to the overall system response, which is much higher compared to the induced quadrupolar moments in the ED example. Therefore, the WSD model is not suitable for accurately describing the response of a MM composed of EQ scatterers at a homogeneous level.

Upon examining the SSD models, we notice a significant improvement in the accuracy

of predicting the optical coefficients when using the SSD-τ model as compared to the SSD-γ model, particularly at lower frequencies $k_0 < k_{0_{\text{iso}}}$ (longer wavelengths). On the other hand, closer to $k_{0_{\text{iso}}}$, both SSD models present identical values for the error function. This strongly suggests that the inclusion of τ in the constitutive relation leads to a better representation of long-range lattice interactions.

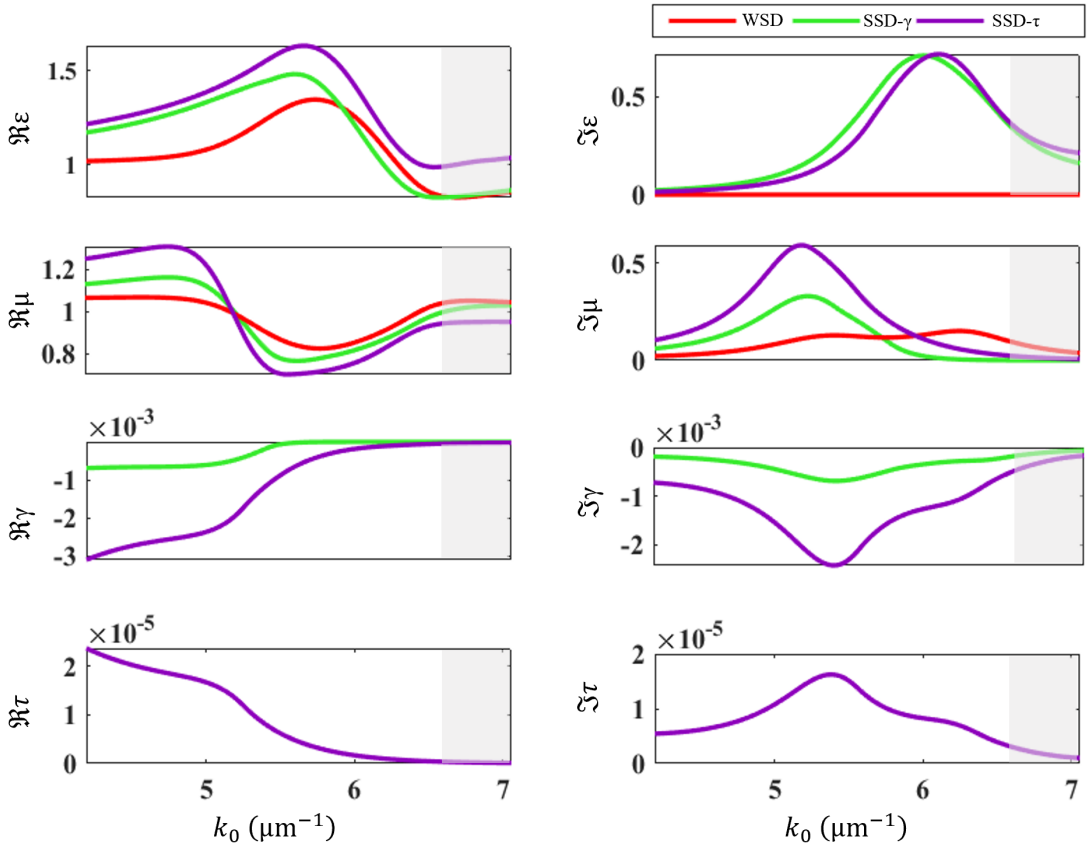

Figure 4.6.: Effective material parameters for a MM made from a periodic arrangement of spheres characterized by an electric quadrupolar response retrieved within the WSD-γ model (red), the SSD-γ model (green), and the SSD-τ model (violet) as a function of the frequency k_0. The gray shaded area marks the frequency domain where the homogenization is not entirely reliable because of an emerging strong anisotropy.

To quantitatively judge the impact of these additional material parameters, it is necessary to examine the retrieved effective material parameters. In Fig. 4.6, the real and imaginary parts of the effective material parameters for all the three models are shown as a function of frequency. The figure legend dictate the curve representing each models.

After examining the material properties retrieved with the WSD model is incapable of giving a precise fit for the imaginary component of electric permittivity while adhering to the passivity condition of $\Im\varepsilon > 0$. The model appears to saturate near zero, rendering

it impossible to draw any significant insights about the material. On the other hand, when analyzing the results obtained from the SSD models, it is observed that the SSD-τ model significantly re-normalizes the non-local parameter γ, while ε and μ remain relatively unchanged. This contrast in the γ value can be attributed to the improvement observed in the error function depicted in Fig. 4.5 (b). Therefore, employing the SSD-τ model leads to a renormalization of the γ parameter, resulting in a better representation of long-range lattice interactions.

To further investigate the long-range effects observed in the MM and its impact on the τ parameter, we systematically modify the oscillator strength $\alpha^e_{0_q}$ and homogenize the MM made of these scatterers. The amplitude $|\alpha^e_{0_q}|$ of the EQ is varied while maintaining the polarizability phase ϕ and consistency with all other parameters for the scatterers in the MM as shown in Fig. 4.5.

Subsequently, we evaluate the absolute values of τ in the homogenized MM and plot the results in Fig. 4.7(b). The plots clearly indicate that $|\tau|$ increases as the EQ's contribution increases. Hence, for an effective description of this MM that carry a strong EQ, it is essential to incorporate τ in the constitutive relation, at a minimum.

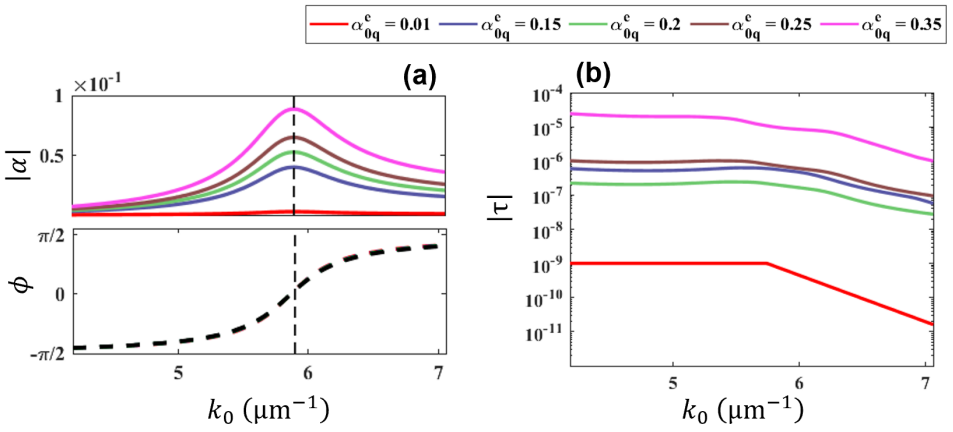

Figure 4.7.: (a) Amplitude and phase of the electric quadrupolar polarizability of the sphere considered in the second example but with a modified oscillator strength $\alpha^e_{0_q}$. The black dashed vertical line represents Lorentzian resonance at frequency $\left(k^e_{0_d}\right)_{\text{iso}} = 5.89\,\mu\text{m}^{-1}$ for the isolated particle. Please, note the phase is the same in all examples, hence there is only a single line for the phase. (b) The absolute value of the effective material parameter τd from the retrieval as a function of the oscillator strength $\alpha^e_{0_q}$ in the considered frequency range.

In conclusion, both the pure electric dipole and the pure electric quadrupole examples highlight how crucial it is to carefully choose a homogenization model that is appropriate for the multipolar order of the MM in question.

4.2.3. Spherical Scatterer with a Combination of Multipoles

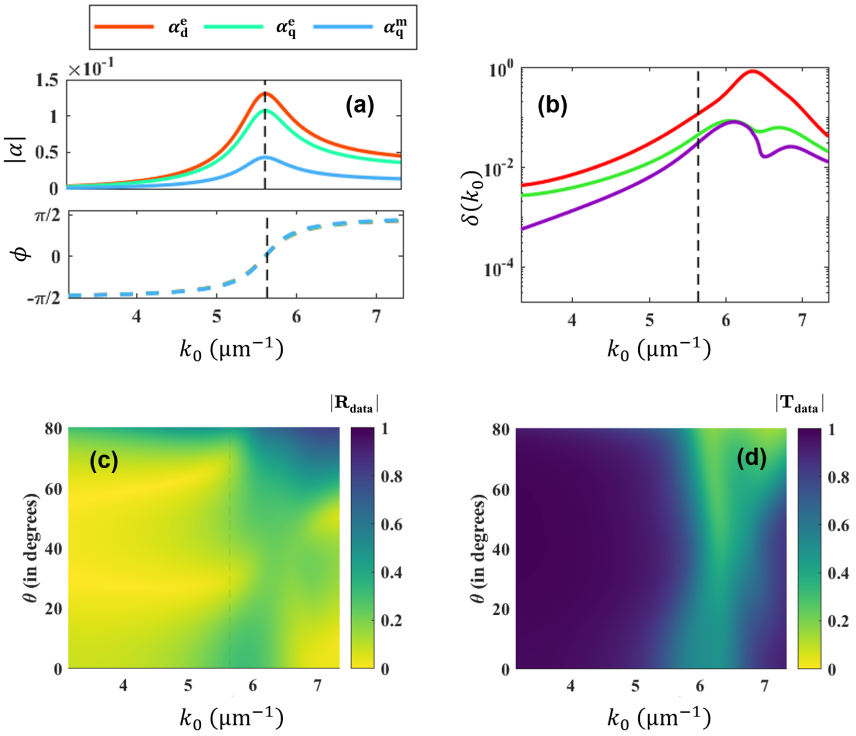

Figure 4.8.: (a) This figure shows the amplitude and phase of the polarizabilities of a sphere characterized by electric and magnetic dipole and electric quadrupole moments. At $k_0 = 5.63\,\mu\text{m}^{-1}$, the polarizabilities all exhibit the same resonance frequency, but with different oscillator strengths. (b) The error function is plotted in logarithmic scale and as a function of the frequency that was considered when homogenizing the MM at a lattice with a period of $\Lambda = 300$ nm. The error function is shown for three homogenization models: the WSD model (in red), the SSD-γ model (in green), and the SSD-τ model (in violet). (c) The absolute values of the reflection ($|\mathbf{R}_{\text{data}}|$) and (d) transmission ($|\mathbf{T}_{\text{data}}|$) are shown as a function of the incidence angle (θ) and the frequency (k_0) for the actual MM of periodicity $\Lambda = 300\,\text{nm}$.

Finally, we intend to access the possibility of homogenizing a MM made from a scatterers that sustaines a combination of different resonant multipolar contributions. The scatterers are characterized by the electric dipole, magnetic dipole, and electric quadrupole moments, each with Lorentzian polarizabilities centered at the same frequency $\left(k_{0_{d/q}}^{e/m}\right)_{\text{iso}} = 5.63\,\mu\text{m}^{-1}$. The associated oscillator strengths are given in the order of electric dipole, magnetic dipole, electric quadrupole as $\alpha_{0_{d/q}}^{e/m} = \{0.5, 0.15, 0.4\} \times \left(6\pi\sqrt{2}c_0\right)$, while the damping parameter is kept the same for all multipole moments at $\sigma_{0_{d/q}}^{e/m} = 0.1\,\text{THz}$ for all the considered moments. This particular example provides an opportunity to explore the homogenization for a metamaterial that exhibits contributions from both induced and pure electric quadrupole effects. The amplitude and phase of the multipolar polarizabilities for the spherical scatterers with varying resonant multipolar contributions are depicted in Fig. 4.8 (a).

To showcase the strong interaction among the multipoles, we depict the absolute reflection and transmission in Fig. 4.8 (c) and (d) as a function of frequency k_0 and incidence angle θ, which are computed for the actual metamaterial. In Fig. 4.8 (d), we observe that the primary resonance features of the infinite periodic array redshift from the resonance frequency of the individual particle, indicating significant lattice interactions. Unlike the examples discussed earlier, which did not involve the combination of electric quadrupole (EQ) and magnetic dipole (MD) moments, we conjecture that more intricate interactions between multipole moments must be taken into account, as implied by the spectral sharp features, such as the absolute value for the reflection coefficient $|\mathbf{R}| \to 0$, in Fig. 4.8 (c) emerging at lower frequencies, indicating long-range interactions.

This particular configuration demonstrates a robust interaction between the intrinsic multipole moments resonating at the same frequency, as reported in [183, 189]. Therefore, it provides an excellent illustration to examine the limitations of all three considered homogenization models.

We begin our analysis by examining the error function obtained from each model as a function of frequency. As shown in Fig. 4.8 (b), the WSD model once again shows very high values for the error function, particularly at high frequencies. This is expected as the present example has dominant spatial dispersion effects. On the other hand, the SSD models show a large improvement in the prediction by at least two orders of magnitude as compared to the WSD model. Based on these results, it can be concluded that the WSD model is unsuitable for accurately describing complex metamaterials within a homogeneous framework. The physical reasoning for these trends would be discussed later when studying the material parameters.

An analysis of the SSD models (shown by the green and violet curves) at lower frequencies ($k_0 < 5.63\,\mu\text{m}^{-1}$ or longer wavelengths) in Fig. 4.8 (b) indicates that the SSD-τ model outperforms the SSD-γ model significantly. This observation emphasizes the importance of using SSD-τ over SSD-γ to obtain more accurate effective material parameters.

Further, We present the effective material parameters obtained from all three homogenization models in Fig. 4.9. The insets in the figure show the fine features in the EMP, with the non-local parameters normalized by the corresponding powers of k_0.

The effective permeability parameter μ in the WSD model displays a Lorentzian resonance,

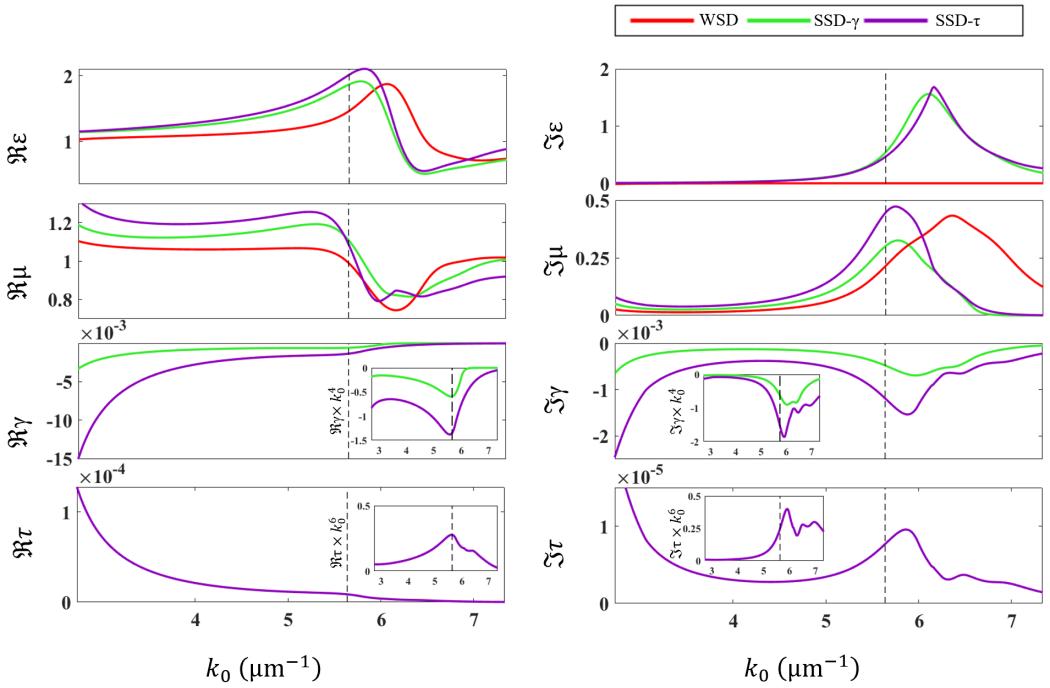

Figure 4.9.: The figure depicts the effective material parameters obtained using three different models: the WSD model (in red), the SSD-γ model (in green), and the SSD-τ model (in violet) plotted against frequency k_0. The metamaterial studied in this analysis comprises a periodic arrangement of spheres exhibiting electric dipolar, electric quadrupolar, and magnetic dipolar responses (see Fig.4.8(a)). The insets present the same data but with the y-axis of both γ and τ parameters scaled by powers of frequency k_0 (i.e., $\gamma \times k_0^4$ and $\tau \times k_0^6$) to emphasize the sharp features of the non-local material parameters.

.

indicating the presence of the intrinsic magnetic dipole moment. However, it fails to account for lattice-induced magnetic contributions as expected from EQ resonance. Additionally, while $\Re\varepsilon$ captures the Lorentzian shape for its resonance, indicating the presence of an electric dipole moment, the $\Im\epsilon$ curve saturates at the zero line, indicating that the WSD model cannot provide a satisfactory fit, respecting the passivity condition $\Im\varepsilon > 0$, for the considered parametric space. Therefore, we conclude that the WSD model is unsuitable for homogenizing this MM.

On the contrary, the SSD models present several notable findings. Firstly, the material parameters ε and μ clearly demonstrate a Lorentzian resonance indicating the presence of the resonant electric and magnetic dipole moments. Additionally, we observe a slight blue shift in the resonance frequency corresponding to both ε and μ. The $\Im\gamma$ values from both SSD models also indicate a similar blue shift in the resonance frequency. This offset is consistent with the blue shift observed in Fig. 4.8 (d). Thus, we can conclude that the

intrinsic electric quadrupolar moments (EQ) and their interaction with other multipolar moments are the cause of this blue shift in the resonance frequency.

Furthermore, as shown in Fig. 4.9, incorporating the non-local parameter τ into the constitutive relation leads to a significant renormalization of both μ and γ relative to the SSD-γ model. In particular, the magnetic permeability μ exhibits subtle features at frequencies approaching the blue-shifted resonance frequency. These features arise from the interaction between EQ and the magnetic dipole moments, which induces a weak magnetic response in the material. Such subtle details are not captured by either the WSD model or SSD-γ model.

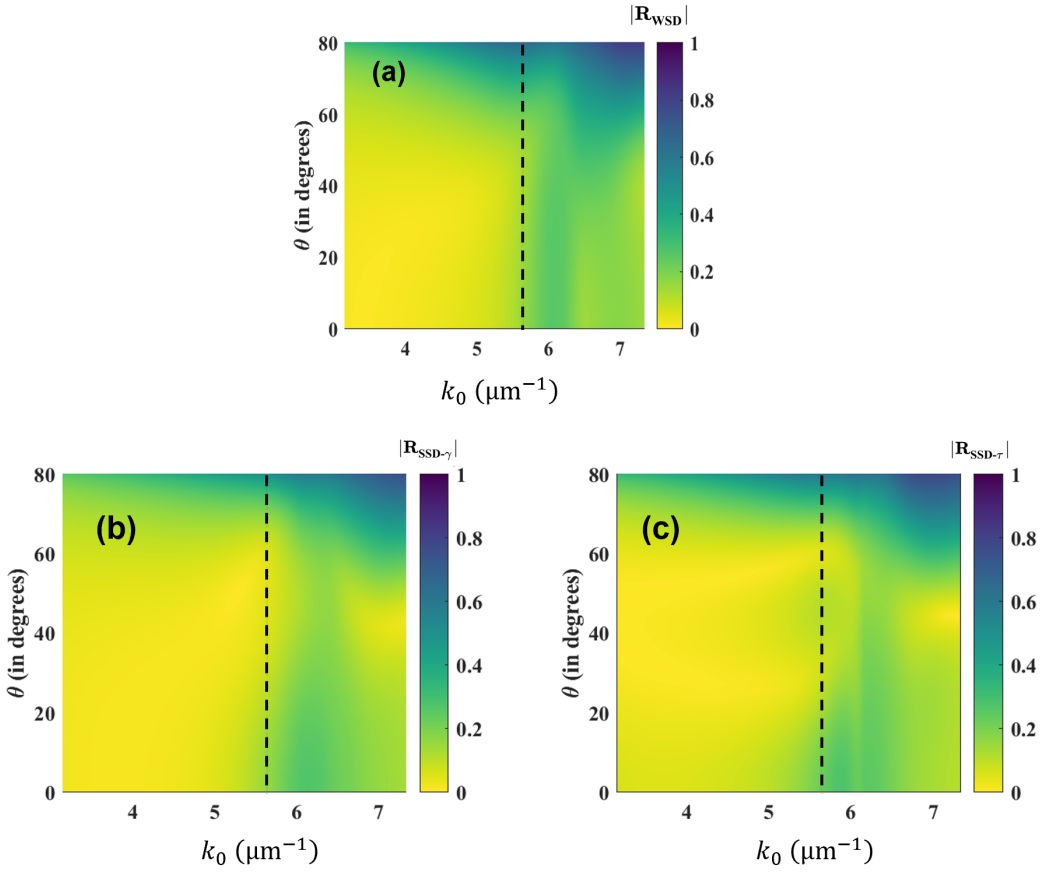

Figure 4.10.: In the figure, the absolute value of reflection is plotted as a function of frequency k_0 and incidence angle θ. (a) shows the results obtained from the WSD model, (b) shows the results from the SSD$-\gamma$ model, and (c) shows the results from the SSD$-\tau$ model. These predictions will be compared to the full-wave simulations presented earlier in Fig. 4.8 (c).

Once we have the effective material parameters, we can now calculate the reflection and transmission coefficient of both frequency k_0 and angle of incidence, $\theta \in (0, 89°]$. The corresponding absolute reflection coefficients are depicted in Fig. 4.10. This will allow us to

evaluate the spectral features captured by each model compared to full-wave simulations already shown in Fig. 4.8 (c). Consistent with our prior analysis of the error function and material parameters, the reflection spectra for the WSD model in Fig. 4.10 (a) lacks any notable spectral features.

To examine the distinct spectral features displayed in Fig. 4.8 (c), as in $|R| \to 0$, that stem from long-range lattice interactions in the MM, we concentrate on frequencies below $k_{0_{\text{iso}}}$ and angles θ ranging from 30° to 75° for the SSD models. An initial inspection reveals that the reflection spectra of the SSD-γ model in Fig. 4.10 (b) do not display any prominent features obtained from Fig. 4.8 (c), whereas the spectra obtained from the SSD-τ model in Fig. 4.10 (d) exhibit some of these distinct characteristics. The ability of the SSD-τ model to capture several of these prominent spectral features can be once again atributed to the renormalization of the effective material parameters that happens when τ is introdcued into the constitutive relation. Therefore employing the SSD-τ model promises improved accuracy for the predicted optical coefficients.

Despite the absence of the unique features in the reflection spectra of the SSD-γ model, a close examination indicates a noticeable dip in the reflection coefficient as the frequency approaches $k_{0_{\text{iso}}}$, which matches the trend observed in the SSD-τ plot shown in Fig. 4.10(c). Additionally, the error plots depicted in Fig. 4.8(b) demonstrate a narrow frequency range where there is no clear benefit in using the SSD-τ model. Referring back to the material parameters presented in Fig. 4.9, we observe that the ε values overlap for both the SSD models for a narrow frequency range towards the blue shifted resonance frequency. This behavior indicates the presence of a dipole-like resonance that is accounted for equally by both the SSD models. This observation aligns with our conclusion from the electric dipole example discussed in Section 4.2.1. Therefore, we can conclude that the γ model predicts only the pure dipolar resonances near $k_{0_{\text{iso}}}$ found in Fig. 4.10(c) by limiting itself to the effects up to the first-order approximation of the effective quadrupolar moment.

As our final results for this study, we depict the predicted optical coefficients of the SSD models, with a focus on the angular-dependent absolute reflection coefficient, given in Fig. 4.11 (a), and absolute absorption + transmission coefficients, given in Fig. 4.11 (b), at a specific free space wavelength $\lambda = 1651\,\text{nm}$. This wavelength demonstrates a Brewster-like effect that emerges from the interplay between the multipolar fields, as described in [46]. The analysis reveals that even though the SSD-τ model accurately captures sharp features

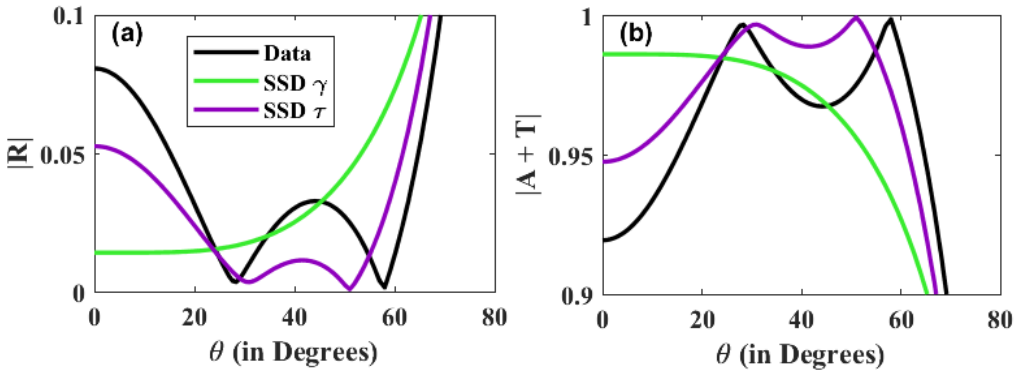

Figure 4.11.: The figure depicts the variation of absolute reflection coefficient ($|\mathrm{R}|$) and the sum of absolute absorption and transmission coefficient ($|\mathrm{A}+\mathrm{T}|$) with respect to incidence angle for a wavelength of $\lambda = 1651\,\mathrm{nm}$.

at small angles of incidence, it underestimates the Brewster angle. This observation suggests that the model does not adequately account for long-range interactions and higher-order field gradients, and material parameters may be needed to address these issues.

In conclusion, we examined in this part of the thesis the advantage of using the non-local constitutive relations in homogenizing metamaterials (MMs) and the significance of effective material parameters in describing strong lattice effects that lead to non-local responses. We also demonstrate that each effective material parameter is influenced by either the intrinsic multipolar moments or their interactions along the lattice. Further, in all three examples that we have considered, the WSD model or the local constitutive relations fail to capture the essence of spatial dispersion in the medium and therefore constantly underestimate the predictions of the reflection and transmission coefficients for the homogeneous equivalent medium. In contrast, the SSD models perform relatively well for all three examples. Specifically, the non-local parameter τ becomes increasingly important as the complexity of the multipoles used to describe the meta-atom increases. This emphasizes the importance of additional material parameters when homogenizing an optical MM with non-local effects.

Further, we learn that analyzing the scattering behavior of the meta-atom can help to determine the appropriate truncation order for the constitutive relation. It also proposes a rule of thumb for choosing the correct homogenization model based on the system's polarizability. For example, a pure mesoscopic dipole system requires at least the SSD-γ model, while the presence of an intrinsic quadrupole moment needs at least the SSD-τ model. By understanding the multipolar moments carried by the meta-atom and studying the induced moments in the original MM, researchers can make an educated guess on the

truncation order for the considered material system.

4.2.4. Determining the Lower Limit of Homogenization Methods.

The findings and insights highlighted in this subsection of the thesis have been previously reported in Ref. [136] and were also discussed by Timon Höß in his Bachelor's thesis entitled "Nonlocal effects in particle arrays with multipolar resonance" at the Institute of Theoretical Solid State Physics (TFP), Karlsruhe Institute of Technology (KIT).

Having analyzed the physical significance of effective material parameters and their dependence on induced multipolar moments, we now turn our attention to examining the reliability of non-local constitutive relations for homogenizing an electric dipolar lattice at different period-to-wavelength ratios. Through a systematic manipulation of the parameter $\frac{\Lambda}{\lambda}$, we investigate the extent to which these constitutive relations can homogenize the material as the periodicity gets shorter. Our observations reveal a breakdown in homogenization ability, regardless of the choice of the homogenization model. This breakdown can be attributed to the spread of excitation across the lattice caused by near-field interactions that become increasingly pronounced as lattice periods decrease. These findings challenge the conventional belief that small lattice periods are necessary for homogenizing a given metamaterial and suggest instead an optimal period at which homogenization is achievable.

Once again we assume a spherical scatterer of electric dipolar type surrounded by air. The polarizability is characterized by a resonance frequency of $\left(k^e_{0_d}\right)_{\text{iso}} = 6.3\,\mu\text{m}^{-1}$, oscillator strength of $\alpha^e_{0_d} = \left(6\pi\sqrt{2}c_0\right)$, and the absorption in the particle is given by the Ohmic loss factor $\sigma_{0^e_d} = 0.1\,\text{THz}$. The corresponding amplitude and phase of the electric dipole polarizability are depicted in Fig. 4.12(a). Then, we construct an array of these scatterers with infinite repetition, arranged in a square lattice pattern with a periodicity denoted by Λ.

To calculate the optical response of the actual metamaterial, we utilized a full-wave solver based on the T-matrix method described in Section 4.1.2. We considered a frequency range that is spectrally close to the resonance and determined the complex reflection and transmission coefficients as a function of the frequency (k_0) and angle of incidence $\theta \in (0°, 89°]$ for selected periodicities (Λ).The simulation parameters included TM-k_x polarization with a plane wave incidence, and the calculations were performed for 100

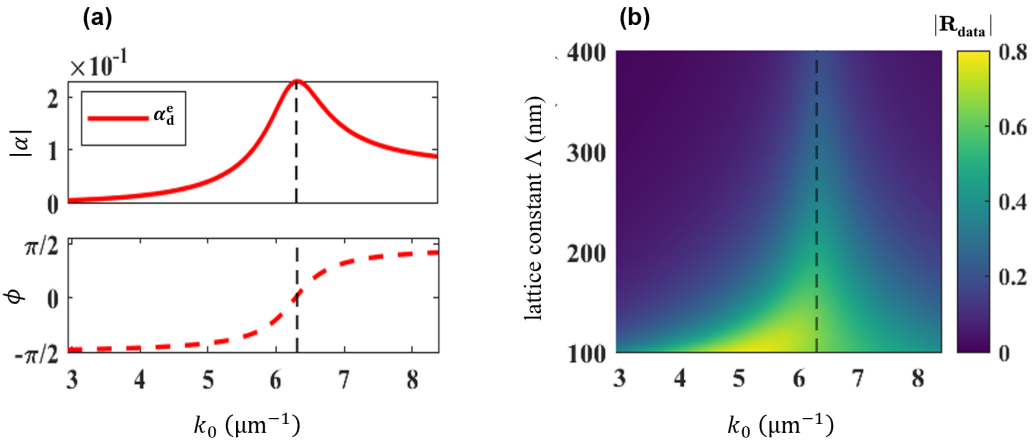

Figure 4.12.: (a) Amplitude and phase of the electric dipolar polarizability of the sphere considered in the initial example. (b) The amplitude of the reflection coefficient, $|\mathbf{R}_{\text{data}}(k_0, k_x = 0)|$, as a function of the frequency and the lattice constant as calculated using the general Mie method described earlier.

different incident angles and 240 frequencies ranging from $k_0 = 3\,\mu\text{m}^{-1}$ to $8.4\,\mu\text{m}^{-1}$, while varying the periodicity from 100 nm to 400 nm.

Once we have the target data, we employ the parameter retrieval method discussed in Section 4.1.1 to obtain the material parameters and the homogeneous description such that the optical coefficients match to those from the full-wave simulation in an optimal sense, *i.e.,* with minimal error function δ. Here, using the SSD-τ model falls redundant as the τ parameter has no significant influence on an array made from pure electric dipole scatterers, as already discussed previously in Section 4.2.1. Therefore, we only use the constitutive relation given by WSD and SSD-γ.

In order to see the salient optical features of the metamaterial being studied, the absolute reflection coefficient, $|\mathbf{R}_{\text{data}}|$, is evaluated at normal incidence as a function of frequency (k_0) and periodicity (Λ) and presented in Fig. 4.12(b). When the periodicity is large, the resonance frequency of the meta-atom is maintained at $\left(k^e_{0_d}\right)_{\text{iso}} = 6.3\ \mu\text{m}^{-1}$. As the lattice period is reduced, the amplitude of the reflection spectra increased, and a greater red shift relative to $\left(k^e_{0_d}\right)_{\text{iso}}$ in the resonance for the metamaterial is observed, which can be attributed to the increased filling fraction. This study enables us to assess the effectiveness of the considered homogenization models in capturing these salient characteristics.

Our analysis of the metamaterial begins with a study of the WSD model, and Fig. 4.13 displays the retrieved effective material parameters using this model. As the considered

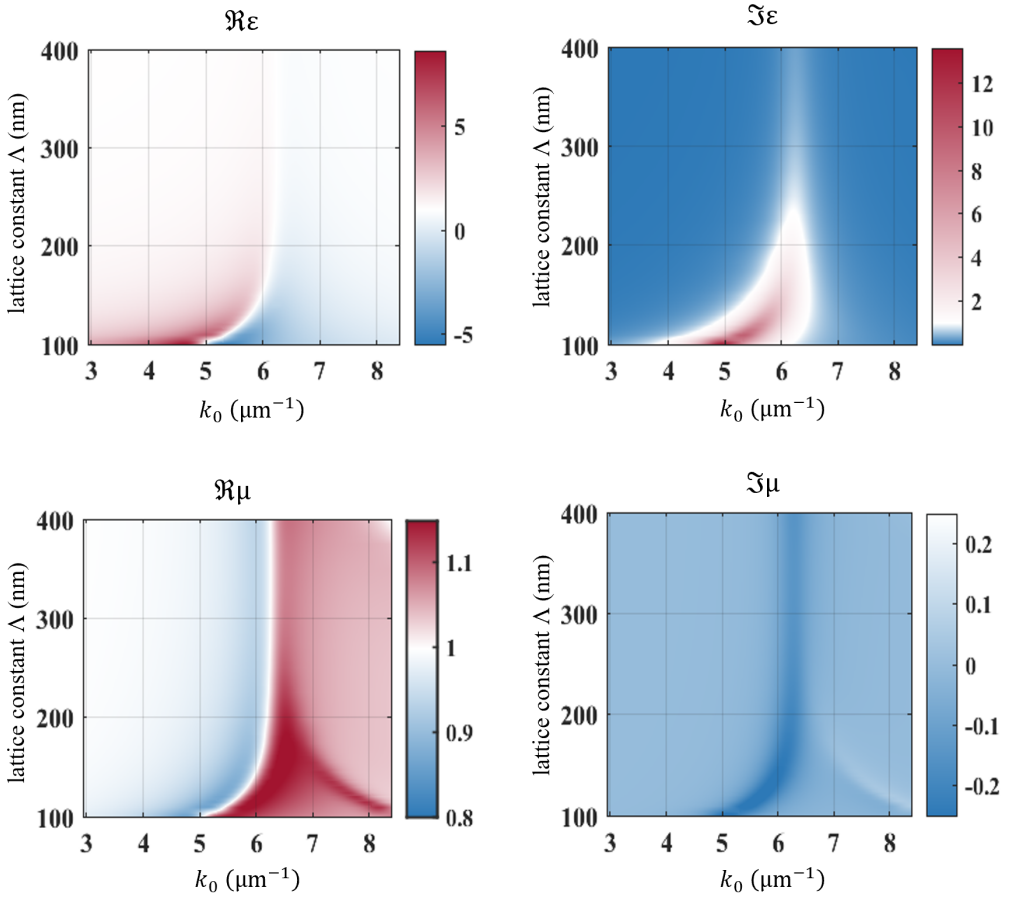

Figure 4.13.: The retrieved effective material parameter obtained for the WSD model is presented in terms of its real and imaginary components. The electric permittivity $\varepsilon(k_0)$ is displayed in the top figures, while the magnetic permeability $\mu(k_0)$ is shown in the bottom figures.

structure is an electric dipole array, the permittivity $\varepsilon(k_0)$ exhibits a strong resonance with high absorption near the isolated particle resonance at $\left(k^e_{0_d}\right)_{\text{iso}} = 6.3$ μm^{-1}, resulting in a real part of the permeability μ that remains close to 1. At frequencies beyond $\left(k^e_{0_d}\right)_{\text{iso}}$, a secondary resonance is acquired by the permeability but is missing for the electric permittivity ε. This resonance displays a blue shift as the periodicity is further decreased. The observed characteristic can be linked to the excitation of an anti-symmetric mode in the dipole array leading to dipole moments in neighboring particles to oscillate out of phase by π. Such oscillations produce a portion of a ring current which is reflected as the magnetic permeability in the bulk. The dense packaging of the scatterers sustains a pronounced near-field interaction on reducing the lattice constant, and these excitations spread across the lattice, requiring the optical response to exhibit non-local behavior. This constitutes the motivation to investigate the SSD-γ model at the considered parameter

range.

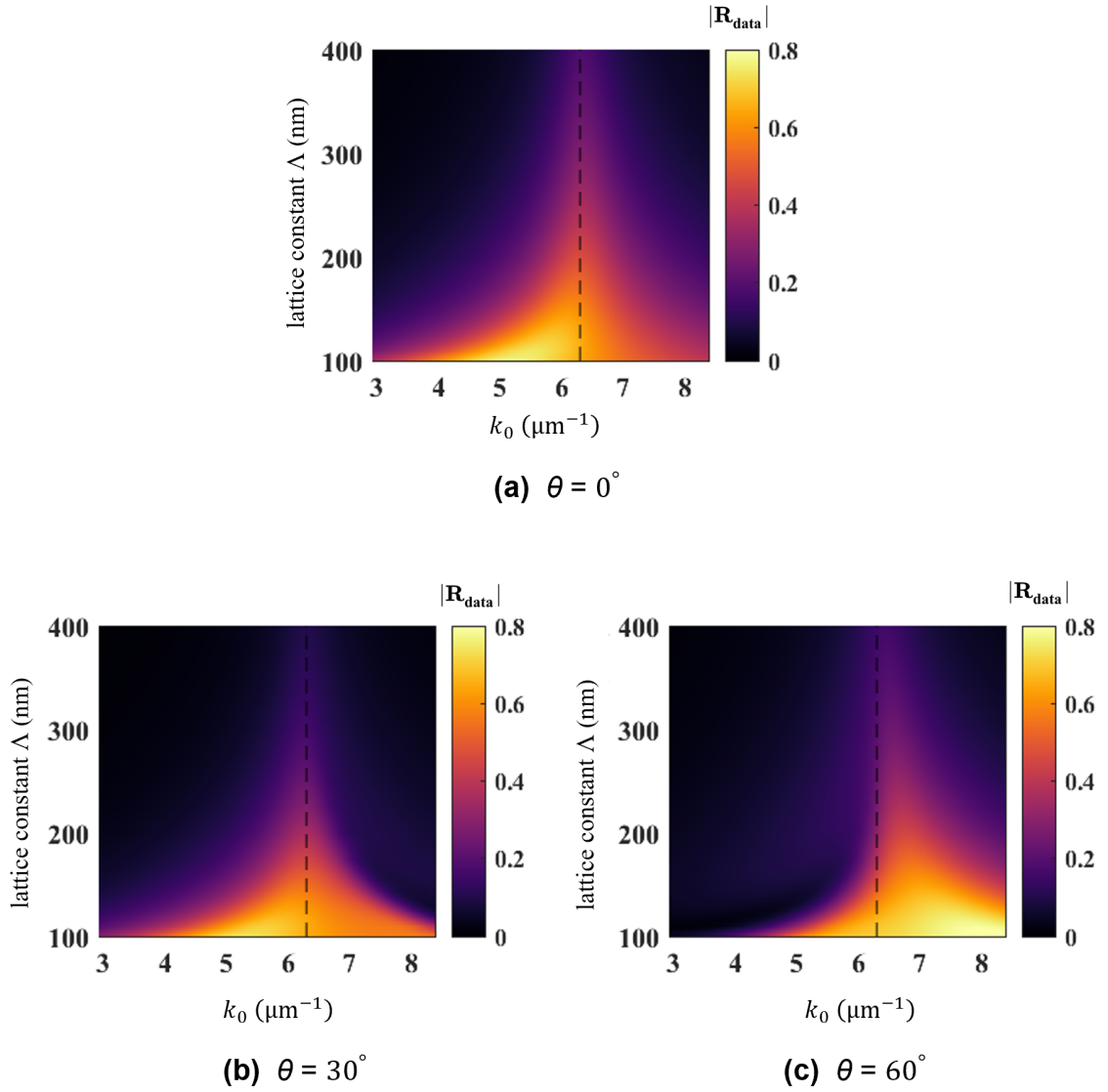

Figure 4.14.: The amplitude of the reflection coefficient $|\mathbf{R}_{\text{data}}|$ calculated using the T-matrix method at different angles of incidence. (a) represents the value at normal incidence. (b) and (c) show the value at angles of 30° and 60°, respectively. The figure highlights the emergence of a secondary resonance with increasing angle of incidence.

To reveal the emergence of the symmetric and anti-symmetric modes more clearly, we plot $|\mathbf{R}_{\text{data}}|$ at 3 different incidence angles: $\theta = 0°, 30°, \text{and } 60°$ as given in Fig. 4.14. In Fig. 4.14 (a), the case for normal incidence is illustrated, where a red shift in the resonance frequency relative to $\left(k^e_{0_d}\right)_{\text{iso}}$ (dashed line) is observed as the lattice period decreases. The observed shift can be explained by the in-phase oscillation of the neighboring dipoles mimicking the symmetric mode of the coupled oscillator. This apparent red-shift is anticipated based on ordinary hybridization theory [190, 191]. On the other hand, Fig. 4.14(b) and Fig. 4.14 (c) depict a secondary resonance that develops corresponding to

the out-of-phase oscillation of the neighboring dipoles, as in the anti-symmetric mode. The anti-symmetric mode results in a change in the ring current, hence its appearance in the effective permeability is expected.

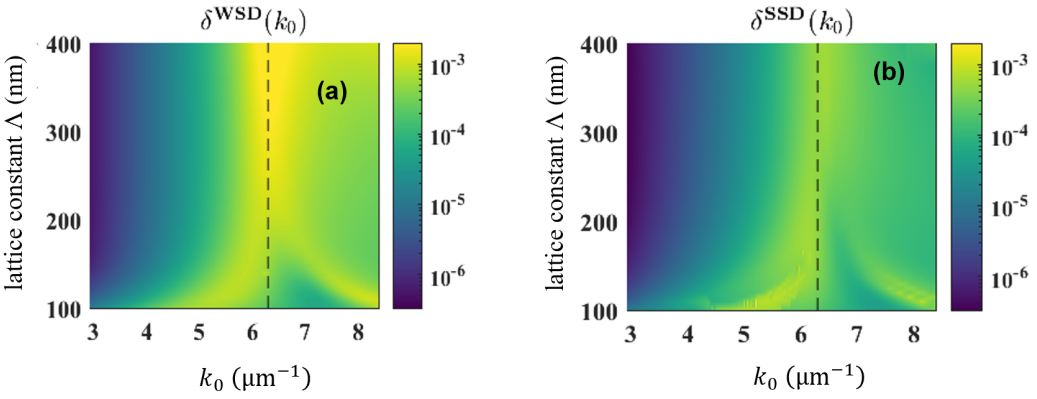

Figure 4.15.: The figures (a) and (b) show the error function $\delta(k_0)$ in logarithmic scale for a range of periodicity Λ as a function of frequency, with (a) corresponding to the WSD model and (b) to the SSD-γ model.

As we now know our goal, we shall now proceed to homogenize this MM with the SSD-γ model by using our parameter retrieval method as discussed in Fig. 4.1. We compare the error function $\delta(k_0)$ in the logarithmic scale of both the SSD-γ model and the WSD model for the considered range of periodicity in Fig. 4.15. As expected, the SSD-γ model provides a more accurate estimate of the optical coefficients, with the improvement being at least two orders of magnitude for the given frequency range. Specifically, at frequencies $k_0 > \left(k^e_{0_d}\right)_{\mathrm{iso}}$, the SSD-$\gamma$ model is very much more reliable at predicting the secondary resonance than the WSD model. One can arrive at the same observation by additionally studying Fig. 4.16, where we plot the summation of the error function across the considered frequency range as a function of the period.

Furthermore, the WSD model exhibits a drastic deterioration at larger periods, which is anticipated due to the characteristic ratio $\frac{\Lambda}{\lambda}$ dictating an increase in the degree of spatial dispersion with periodicity. In contrast, the SSD-γ model is capable of achieving satisfactory material homogenization, regardless of the period.

As we decrease Λ, the SSD-γ model continues to outperform the WSD model, but we also observe a range of periodicity ($\Lambda = 200\,\mathrm{nm} - 300\,\mathrm{nm}$) where both models exhibit relatively good performance. This is somewhat anticipated since homogenization accuracy is expected to increase when the period is significantly smaller than the operational wavelength.

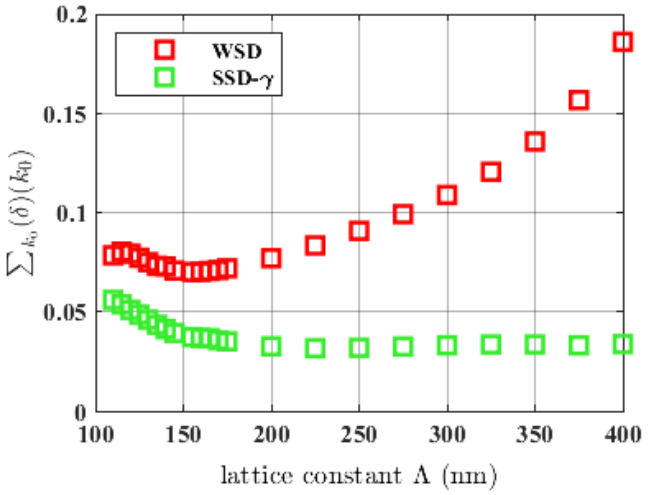

Figure 4.16.: This figure depicts the sum of the error function over the considered frequency range plotted as a function of lattice period. The red squares denote the WSD model and the green square denotes the SSD-γ model.

As we further decrease the period, a surprising observation emerges: both the SSD-γ and WSD models demonstrate inadequate performance, with rapid deterioration. The plot shown in Fig. 4.16 indicates the existence of a critical periodicity value, represented by $\Lambda_{\text{critical}} = 200$ nm, below which the homogenization itself becomes suboptimal. Notice that, these Λ values are within the range where the anti-symmetric modes are stimulated, resulting in incomplete consideration of the secondary resonance by the effective parameters in the SSD-γ model. The inability to homogenize the MM at this range can be explained as follows. When the filling fraction is high, the near field interactions become dominant. Therefore enabling strong coupling between adjacent particles allows for the individually polarized particles to transport energy over longer distances within the material. This coupling mechanism has been utilized before in [192, 193] for waveguiding. While it is understandable that the local constitutive relation cannot homogenize interactions over long distances, it is unexpected that even the SSD-γ model fails to be insufficient. As a result, the range of validity for the analyzed models is restricted, and their ability to provide a comprehensive effective description of the slab is limited for lower periodicities. Therefore, $\Lambda_{\text{critical}}$ can be deemed as the minimum periodicity limit for successful homogenization of the electric dipole slab.

In conclusion, we investigate the ability of a non-local constitutive relation in accounting for the optical response of an electric dipole array by systematically varying the lattice constant. We show the reliability of the non-local model for all the considered frequencies

and lattice constants. The non-local constitutive relation performs always better when compared to its local counterpart and is particularly able to capture the optical response at the effective level when the period tends to be rather large. On the other hand, at very small periods where the spread of excitation caused by near-field interactions among adjacent particles are pronounced, both relations became less optimal. The study also revealed an optimal period for homogenization, *i.e.,* when the period got smaller, the spread of near-field excitation in essence denies reasonable homogenization. This insight clearly suggests that in addition to the constraint on the $\frac{\Lambda}{\lambda} < 1$, for each inclusion there is an optimal period.

4.3. Effective Transition Matrix: $\mathbf{T}_{\text{eff}}$- matrix

The findings presented in this subsection of the thesis were published earlier in Ref. [194]. I would like to express my gratitude to Benedikt Zerulla and Dr. Ivan Fernandez-Corbaton for their valuable contributions and discussions that aided in the development of this section of the thesis.

Identifying material parameters in the constitutive relation traditionally involves a fitting procedure, which can be challenging and is associated with various shortcomings. One potential weakness is that a reference object is involved from the beginning. As discussed in Section 4.1.1, Before using the fitting algorithm, the target optical coefficient must be determined, which can be a restricting factor as it involves an additional step of performing a full wave simulation to generate the target data. Another potential issue is that multiple parameter sets can produce the same objective function value. While the solution may be optimal, it is not immediately clear whether the retrieved material parameters can be applied to target objects with different shapes. For instance, machine learning methods demonstrate a non-uniqueness issue [55], indicating that measurements can often be adequately approximated by various sets of material parameters [78]. The validity of all these different parameter sets for different objects is yet to be established.

To circumvent such limitations, we present a new semi-analytical method for homogenizing materials in three dimensions. Our novel homogenization method is based on a linear operator that accurately describes the linear interaction of light with the bulk material, i.e., the infinite 3D lattice of scatterers. This linear operator is represented in the form of an effective T-matrix, denoted as $\mathbf{T}_{\text{eff}}$, which is computed using the lattice vectors to

obtain the mutual interaction and the T-matrix of a single isolated copy of the unit cell, referred to as $\mathbf{T}_{\text{cell}}$.

The effective T-matrix includes all the couplings due to the infinite lattice, transforming $\mathbf{T}_{\text{cell}}$ into $\mathbf{T}_{\text{eff}}$ and removing the lattice interactions. Consequently, the material response can be described by replacing the copies of $\mathbf{T}_{\text{cell}}$ interacting with each other with copies of $\mathbf{T}_{\text{eff}}$, which do not interact with each other. The effective T-matrix is an excellent starting point for homogenization because it is shape-independent, decouples the unit cells, and provides an exact description of the light interaction with the 3D lattice of scatterers forming the material. Notably, $\mathbf{T}_{\text{eff}}$ does not suffer from spatial dispersion.

In our research, we present a bijective connection between the dipolar component of $\mathbf{T}_{\text{eff}}$, denoted as $\mathbf{T}_{\text{eff}}^{\text{dip}}$, and the 6×6 model describing the local constitutive relations of the effective medium. Specifically, $\mathbf{T}_{\text{eff}}^{\text{dip}}$ contains 36 parameters and is directly related to the effective material parameters in the constitutive relations. These material parameters are exclusively determined by the 3D lattice and scatterers present in the unit cell and are not affected by the shape of the target object. Additionally, they account for all the modifications induced by the lattice on the dipoles and are free from spatial dispersion. When compared to other methods, neither retrieval nor fitting procedures are needed, and the actual assignment of effective properties is a straightforward computation using the T-matrix framework. Within one calculation, all entries of the effective material tensors are computed.

We start with the definition of the effective T-matrix $\tilde{\mathbf{T}}\text{eff}(\mathbf{k}_{\parallel})$ as discussed in Eq. (17) of Ref. [171]. This $\tilde{\mathbf{T}}\text{eff}(\mathbf{k}_{\parallel})$ describes the scattering by an object located at the origin of a 2D periodic lattice, including all lattice couplings. The effective T-matrix depends on the component of the wave vector parallel to the lattice plane, denoted as $\mathbf{k}_{\parallel}$. For a 3D lattice, the formula remains the same, but $\mathbf{k}_{\parallel}$ is replaced by the total wave vector $\mathbf{k}$ [195].

$$\tilde{\mathbf{T}}_{\text{eff}}(\mathbf{k}) = \left(\mathbf{I} - \mathbf{T}_{\text{cell}} \sum_{\boldsymbol{R} \neq \mathbf{0}} \mathbf{C}^{(3)}(-\boldsymbol{R}) \mathrm{e}^{\mathrm{i}\mathbf{k}\cdot\boldsymbol{R}} \right)^{-1} \mathbf{T}_{\text{cell}}, \tag{4.9}$$

where $\mathbf{T}_{\text{cell}}$ is the T-matrix of an isolated unit cell. The infinite sum $\sum_{\boldsymbol{R}\neq\mathbf{0}} \mathbf{C}^{(3)}(-\boldsymbol{R})\mathrm{e}^{\mathrm{i}\mathbf{k}\cdot\boldsymbol{R}}$, which is evaluated with the Ewald summation method, includes the interaction of the scatterers forming the material [171]. In this matrix, $\boldsymbol{R}$ is a lattice vector, $\mathbf{C}^{(3)}(-\boldsymbol{R})$ is a

matrix of translation coefficients, and $\mathbf{k}$ is the wave vector of the incident field. By summing a maximum allowed multipolar order, the computation of the total electromagnetic coupling between the unit cell located at $\boldsymbol{R} = \mathbf{0}$ and all other unit cells in the infinite 3D lattice becomes exact.

The elements of the $\tilde{\mathbf{T}}_{\text{eff}}(\mathbf{k})$ linearly relate $\mathbf{q}(\mathbf{k_i})$, the multipolar expansion coefficient of the incident plane wave with wave vectors $\mathbf{k_i}$, on the unit cell placed at the origin and $\mathbf{p}(\mathbf{k_i})$ the multipolar expansion coefficient of the corresponding scattered plane waves up to an arbitrary multipolar order. The relation reads as follows:

$$\tilde{\mathbf{p}}(\mathbf{k}) = \tilde{\mathbf{T}}_{\text{eff}}(\boldsymbol{k}) \cdot \mathbf{a}(\mathbf{k}). \tag{4.10}$$

The definition of the multipolar expansion functions, also known as multipolar fields or vector spherical harmonics, can be found in Eq. (15, S3a-S3d) of Ref. [171].

The $\tilde{\mathbf{T}}_{\text{eff}}(\boldsymbol{k})$ matrix in Eq. (4.10) can only be used for a specific incident field, i.e., a plane wave with momentum $\mathbf{k}$. This is because the 3D lattice displays distinct properties when viewed from different directions, which affects the lattice sums through the $e^{i\mathbf{k}\cdot\boldsymbol{R}}$ factor. Thus, $\tilde{\mathbf{T}}_{\text{eff}}(\boldsymbol{k})$ cannot be used for any other incident direction, making it a significant disadvantage as a starting point for homogenization. In other words, if material parameters are determined using $\tilde{\mathbf{T}}_{\text{eff}}(\mathbf{k})$, they will be dependent on the direction of $\mathbf{k}$, which is undesirable in the context of a homogeneous medium. This issue can be mitigated if considering a planar slab and the plane wave decomposition of the scattered field.

On decomposing the scattered field $\tilde{\mathbf{p}}$ in Eq. (4.10) into plane waves, This decomposition allows us to view Eq. (4.10) as providing one of the columns of a T-matrix in the plane wave basis $\mathbf{T}_{\text{eff}}^{\text{pw}}$, where the system is excited by a plane wave and produces scattered plane waves. By scanning the direction of $\mathbf{k}$, we can obtain the entire $\mathbf{T}_{\text{eff}}^{\text{pw}}$. The next step involves transforming $\mathbf{T}_{\text{eff}}^{\text{pw}}$ from the plane wave basis to the multipolar basis, which yields $\mathbf{T}_{\text{eff}}$, an effective T-matrix in the multipolar basis that is valid for all $\mathbf{k}$ directions and is not explicitly dependent on the $\mathbf{k}$ direction. To compute $\mathbf{T}_{\text{eff}}$, we can adapt the procedure described in Ref. [196]. This involves selecting a finite number of points on the $\hat{\mathbf{k}}$ sphere (i.e., the sphere of directions of $\mathbf{k}$), which can be accomplished using the method outlined in [197]. Then, we compute the $\tilde{\mathbf{T}}_{\text{eff}}(\boldsymbol{k})$ matrices corresponding to each $\hat{\mathbf{k}}$ and use Eq. (4.10) two times for each $\hat{\mathbf{k}}$ (once for each of the two possible polarization handedness of an

incident plane wave with momentum $\mathbf{k}$). The coefficients of all the incident plane waves $\mathbf{a}^{\mathbf{k}_1}, \ldots, \mathbf{a}^{\mathbf{k}_K}$, and their corresponding expansions of the scattered waves $\tilde{\mathbf{p}}^{\mathbf{k}_1}, \ldots, \tilde{\mathbf{p}}^{\mathbf{k}_K}$, can then be collected in a matrix equation as follows:

$$(\tilde{\mathbf{p}}^{\mathbf{k}_1}, \ldots, \tilde{\mathbf{p}}^{\mathbf{k}_K}) = \mathbf{T}_{\text{eff}} \cdot (\mathbf{a}^{\mathbf{k}_1}, \ldots, \mathbf{a}^{\mathbf{k}_K}), \tag{4.11}$$

To obtain $\mathbf{T}_{\text{eff}}$, it is important to select a large number of points in the direction sphere, as it should be much larger than the size of $\mathbf{T}_{\text{eff}}$. An important aspect of Eq. (4.11) is that it ensures that the response of $\mathbf{T}_{\text{eff}}$ to an incident plane wave with a specific propagation direction $\hat{\mathbf{k}}$ is similar to the response of $\tilde{\mathbf{T}}_{\text{eff}}(\mathbf{k})$.

Once the $\mathbf{T}_{\text{eff}}$ of type Eq. (4.11) is known, we can proceed to calculate the effective material parameters for a given homogenization model. since we are interested only in the dipolar elements $\mathbf{T}_{\text{eff}}^{\text{dip}}$, we have opted for a linear 6×6 local bi-anisotropic Condon-Tellegen model written in the frequency domain:

$$\begin{pmatrix} \mathbf{D}(k_0) \\ \mathbf{B}(k_0) \end{pmatrix} = \begin{pmatrix} \varepsilon_{\text{eff}}(k_0) & \mathrm{i}\kappa_{\text{eff}}(k_0) \\ -\mathrm{i}\kappa_{\text{eff}}(k_0) & \mu_{\text{eff}}(k_0) \end{pmatrix} \begin{pmatrix} \mathbf{E}(k_0) \\ \mathbf{H}(k_0) \end{pmatrix}, \tag{4.12}$$

where $\varepsilon_{\text{eff}}(k_0)$ is the effective electric permittivity, $\mu_{\text{eff}}(k_0)$ the effective magnetic permeability, and the $\kappa_{\text{eff}}(k_0)$ is the effective chirality parameter describing the coupling between the electric and magnetic fields.

The derivation connecting the 6×6 effective constitutive matrix given in Eq. (4.12) to the dipolar part of $\mathbf{T}_{\text{eff}}$, denoted as $\mathbf{T}_{\text{eff}}^{\text{dip}}$, is provided in the appendix Appendix D. $\mathbf{T}_{\text{eff}}^{\text{dip}}$ consists of 36 parameters and is obtained by setting all the entries of $\mathbf{T}_{\text{eff}}$ to zero, except those that relate to the incident and scattered dipolar fields. This connection is bijective and can be expressed as follows:

$$\begin{pmatrix} \varepsilon_{\text{eff}} & \mathrm{i}\kappa_{\text{eff}} \\ \mathrm{i}\gamma_{\text{eff}} & \mu_{\text{eff}} \end{pmatrix} = \begin{pmatrix} \varepsilon_{\text{h}}\mathbf{I}_3 & 0 \\ 0 & \mu_0\mathbf{I}_3 \end{pmatrix} + n\left(\mathbf{I}_6 - n \cdot q \; s_1\left[\mathbf{T}_{\text{eff}}^{\text{dip}}, \mathbf{L}\right]\right)^{-1} \times q \; s_2\left[\mathbf{T}_{\text{eff}}^{\text{dip}}\right]. \tag{4.13}$$

The expression in Eq. (4.13), which defines the effective constitutive parameters in terms of $\mathbf{T}_{\text{eff}}^{\text{dip}}$, involves a depolarization tensor $\mathbf{L}$ and various functions, as described in Eq. (D.6) in the Appendix D. For brevity, we drop the explicit frequency argument (k_0). The

term containing $\mathbf{L}$ accounts for the depolarization of a lattice of non-interacting scatterers, as opposed to other methods where depolarization arises from the interaction between scatterers [198, 199].

It should be emphasized that $\mathbf{T}_{\text{eff}}^{\text{dip}}$ contains information not only on the dipolar component but also the non-dipolar component of the T-matrix of the isolated scatterer $\mathbf{T}_{\text{cell}}$. The non-dipolar contributions emerging from the multipolar interactions in the lattice where they couple to the dipolar terms of the effective T-matrix, and can be especially prominent in dense lattices, even for objects that are electromagnetically small. All the changes that arise from non-local lattice interactions to the dipolar response are accounted well within the local material parameters. The frequency-dependent formulation accommodates any existing temporal dispersion.

It is crucial to verify that the non-dipolar component of $\mathbf{T}_{\text{eff}}$ does not dominate when utilizing the local constitutive relation as shown in Eq. (4.12). To evaluate this, the following equation can be used:

$$\delta\left(\mathbf{T}_{\text{eff}}\right) = \sqrt{\frac{\text{Tr}\left\{\left(\mathbf{T}_{\text{eff}}^{\text{dip}} - \mathbf{T}_{\text{eff}}\right)^{\dagger}\left(\mathbf{T}_{\text{eff}}^{\text{dip}} - \mathbf{T}_{\text{eff}}\right)\right\}}{2\left(\text{Tr}\left\{\mathbf{T}_{\text{eff}}^{\text{dip}\dagger}\mathbf{T}_{\text{eff}}^{\text{dip}}\right\} + \text{Tr}\left\{\mathbf{T}_{\text{eff}}^{\dagger}\mathbf{T}_{\text{eff}}\right\}\right)}}, \tag{4.14}$$

The formula above uses $\delta(\mathbf{T}_{\text{eff}}) \in [0, 1]$ where $\delta(\mathbf{T}_{\text{eff}}) = 0$ indicates that $\mathbf{T}_{\text{eff}}$ is equal to its effective dipolar part $\mathbf{T}_{\text{eff}}^{\text{dip}}$, which is located in the upper-left corner of the matrix, while the rest of the entries are zero. The symbol † represents the transpose conjugate operation. To compute $\delta(\mathbf{T}_{\text{eff}})$, $\mathbf{T}_{\text{eff}}^{\text{dip}}$ is constructed to have the same dimensions as $\mathbf{T}_{\text{eff}}$, with the effective dipolar part located only in the upper-left corner of the matrix. that the square root of the sum of the absolute values, squared individually, , of every entry in the matrix $\mathbf{A}$ is given by $\sqrt{\text{Tr}\{\mathbf{A}^{\dagger}\mathbf{A}\}}$, which is the expression of the Hilbert-Schmidt norm of $\mathbf{A}$. In order to ensure the appropriateness of Eq. (4.12), a very small value of $\delta(\mathbf{T}_{\text{eff}}) \to 0$ is necessary.

In the following example, we demonstrate the effectiveness of the $\mathbf{T}_{\text{eff}}$ methodology by using it to homogenize an array of gold spheres arranged on a cubic lattice. This particular example is selected to ensure that the non-dipolar terms in $\mathbf{T}_{\text{eff}}$ are negligible, and that the local constitutive relation is sufficient to describe the gold array as a homogeneous medium.

4.3.1. Gold Spheres in a Cubic Lattice

To illustrate, let's examine gold spheres arranged in a cubic lattice with a lattice constant of $\Lambda = 2.05\,\text{nm}$ and a radius of $1\,\text{nm}$. The symmetry of the cubic lattice by default sets the chirality parameter κ to be zero. The host medium that surrounds them has a relative permittivity of $\varepsilon_{\text{r,h}} = 2.25$. This particular example was chosen with consideration to the findings in Ref. [200].

The material parameters of gold utilized in this study are obtained from [71]. All multipoles up to the $N = 5$ multipolar order are taken into account in the calculations. Initially, the T-matrix of a isolated sphere is computed using Mie theory. Fig. 4.17**(a)** displays the ratio of the electric dipolar entry of the effective temperature ($\mathbf{T}_{\text{eff}}$) of a material to the same T-matrix entry of an isolated sphere $\mathbf{T}_{\text{cell}}$. While the response of an individual sphere is well approximated by an electric dipolar polarizability ($N = 1$), the interactions of the lattice involving up to the $N = 5$ multipolar order significantly modify the electric dipolar polarizability of the individual sphere. At certain frequencies, the amplitude of the electric dipolar entry of $\mathbf{T}_{\text{eff}}$ is more than twice the corresponding value for the isolated sphere in $\mathbf{T}_{\text{cell}}$. Incorporating higher multipolar orders in the computation of $\mathbf{T}_{\text{eff}}$ is crucial due to the significant influence of lattice-induced effects on the dipolar part of $\mathbf{T}_{\text{eff}}$. These effects also have an impact on the effective permittivity, as demonstrated in Fig. 4.17**(b)**, where a very distinct resonance is observed near $800\,\text{nm}$. A much less notable resonance can also be observed close to $600\,\text{nm}$.

We have not included the permeability as there is no significant magnetic resonance in the frequency range under consideration. However, it has been taken into account in calculating the responses of the slab and sphere presented below. In Fig. E.6 of the Appendix D, we show that the dipolar part dominates the effective T-matrix ($\delta\left(\mathbf{T}_{\text{eff}}\right) < 8 \times 10^{-5}$ in the entire frequency range), indicating the importance of incorporating higher multipolar orders in the calculation of $\mathbf{T}_{\text{eff}}$. Hence, we expect accurate results from the homogenized models for target objects of various shapes.

Next, we examine a specific geometry: a slab of thickness $2.15\,\text{mm}$, equivalent to 2^{20} layers of gold spheres. We use the well-established Fresnel equations and standard interface conditions to obtain the reflection coefficient of the slab using the effective material parameters. We then compare the obtained reflection coefficients with the exact solutions

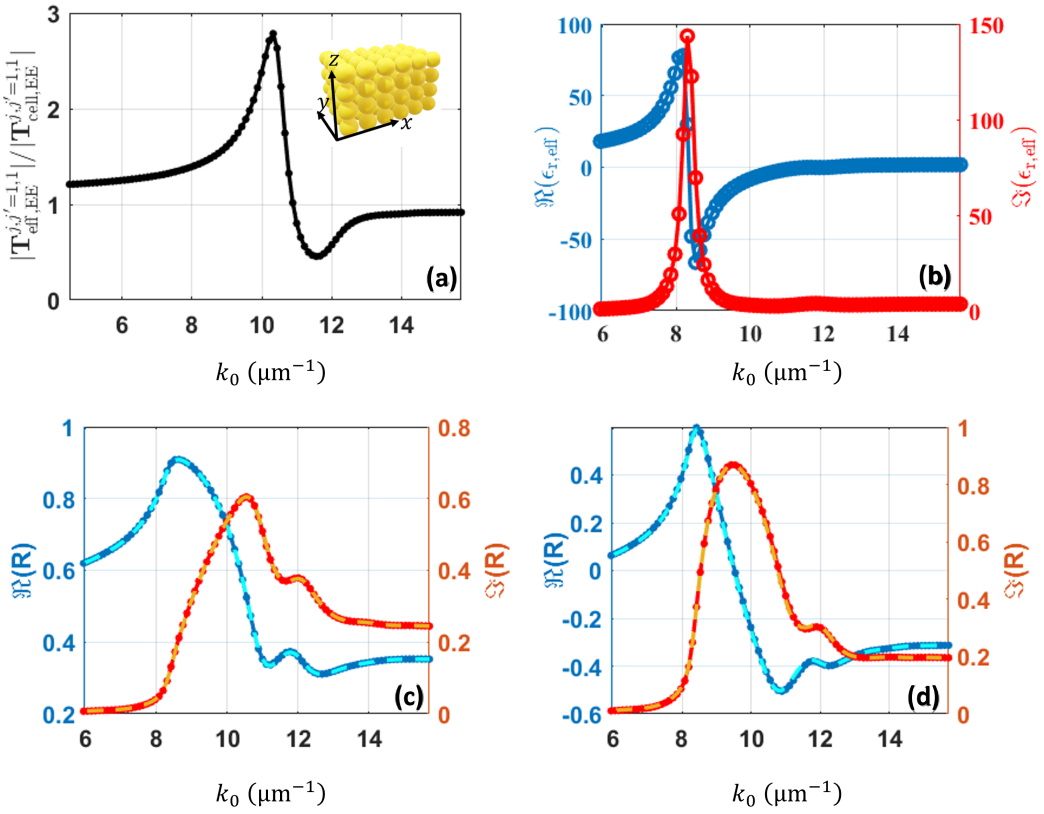

Figure 4.17.: (a) The figure displays the ratio of the electric dipolar entry of the effective temperature ($\mathbf{T}_{\mathrm{eff}}$) of a material to the same T-matrix entry of an isolated sphere. (b) The Eq. (4.13) is used to derive the effective permittivity of a lattice structure. (c) The transverse magnetic (TM) reflection coefficient for normal incidence and (d) for oblique incidence is presented for a 2.15 mm thick slab, equivalent to 2^{20} layers of gold spheres. The wave vector direction in the case of oblique incidence is $\hat{\mathbf{k}}_{\mathrm{inc}} = [\sin(\theta), 0, \cos(\theta)]^{\mathrm{T}}$, with $\theta = 75°$. The results obtained using the effective parameters show perfect agreement with the exact results for the non-homogeneous slab made from the lattice of gold spheres, as calculated with the full-wave solver mpGMM, in both cases.

for a slab made from the actual lattice of gold spheres, calculated using the full-wave solver Multilayer Periodic General Mie Method (mpGMM) whose functionality is described in Ref. [171]. Since the slab is highly absorbing and thick, its transmission is zero. We use a transverse magnetic (TM)-polarized plane wave with a wave vector in the XZ-plane, $\hat{\mathbf{k}}_{\mathrm{inc}} = [\sin(\theta), 0, \cos(\theta)]^{\mathrm{T}}$, where θ represents the angle of incidence. We consider two cases: normal incidence ($\theta = 0°$) in Fig. 4.17**(c)**, and oblique incidence with $\theta = 75°$ in Fig. 4.17**(d)**. For normal incidence, TM polarization means polarization along the negative x-direction. For oblique incidence, the polarization is correspondingly rotated [see e.g., Eq. (2.62) in Ref. [201]].

Since the material is effectively isotropic, only the x-components of the effective permittivity and permeability are used to calculate the response of the effective slab. It is observed that

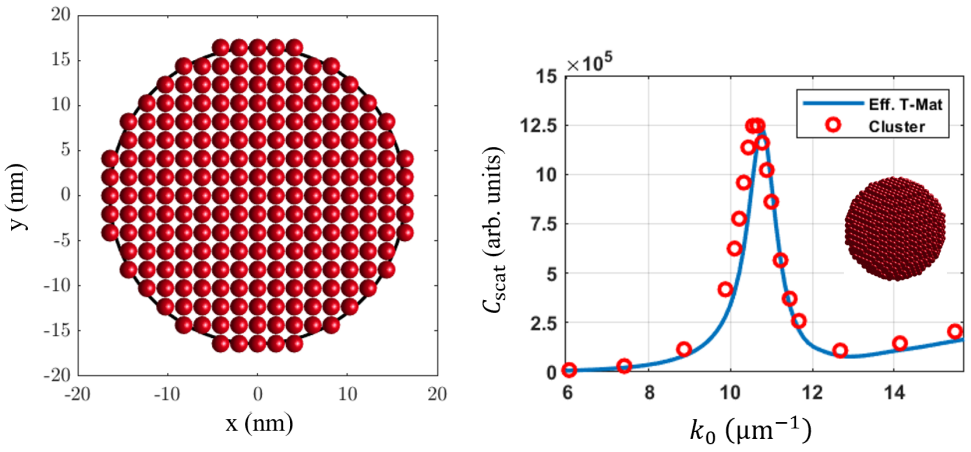

Figure 4.18.: The cubic lattice of gold spheres analyzed in Fig. 4.17 is used to create an object that is approximately spherical in shape. An equatorial cross-cut of the arrangement is presented in Fig. 4.18**(a)**, where a black circle of radius $R_{\text{eff}} = 8a = 16.4\,\text{nm}$ is shown. In **(b)**, The scattered plane wave cross-section is then shown for both the cluster and the effective sphere, and it is found that the calculated cross-section for the cluster agrees well with the effective material parameters.

the results obtained with mpGMM are in excellent agreement with the results obtained using the effective parameters. However, it should be noted that in the material described above, the distance between particles is so small that electron spill-out and tunneling can occur, and these quantum-mechanical effects are not taken into account in the effective T-matrix. It is important to note that the T-matrix formalism is not suitable when significant electronic currents flow across the smallest spheres surrounding the scatterers [168, 202]. This example serves to illustrate the homogenization approach.

In the following analysis, we investigate a target object that has a different shape than the previous one. Specifically, we utilize the same discrete gold-spheres-in-cubic-lattice material to form a cluster with an approximately spherical shape having a radius of $R_{\text{eff}} = 8a = 16.4\,\text{nm}$, as illustrated in the inset of Fig. 4.18**(a)**, and presented in Fig. 4.18**(b)**. We compare the scattering cross-sections calculated in two different ways: using CELES [203] to compute the exact solution for the cluster and Mie theory to calculate the cross-section for a homogeneous effective sphere with radius R_{eff} and effective material parameters derived from $\mathbf{T}_{\text{eff}}^{\text{dip}}$.

Cross-sections for the scattered waves is given as:

$$C_{\mathrm{sca}} = \frac{2\pi \sum_{\hat{\boldsymbol{k}}_{\mathrm{sca}}} |\mathbf{E}_{\hat{\boldsymbol{k}}_{\mathrm{sca}}}|^2}{k_{\mathrm{sca,h}}^2}, \tag{4.15}$$

where $\mathbf{E}_{\hat{\boldsymbol{k}}_{\mathrm{sca}}}$ are the scattered field amplitudes computed with CELES, $k_{\mathrm{sca,h}}$ is the absolute value of the wave vector of the scattered plane waves in the surrounding medium, and $\hat{\boldsymbol{k}}_{\mathrm{sca}}$ is the propagation direction of the scattered plane waves.

The results reveal a good agreement between the two cross-sections, supporting the idea that effective material parameters can be utilized regardless of the target object's shape. The resonance observed in the figure corresponds to a localized plasmon-polariton excited in the sphere when the effective permittivity closely satisfies the Fröhlich condition. However, some differences are observed in Fig. 4.18**(b)**, which can be attributed to the non-perfect spherical shape of the cluster. Furthermore, for homogenization techniques to be applicable, a cluster must have a sufficiently large number of unit cells, and some inaccuracies may arise due to having a finite number of spheres in the cluster.

In conclusion, we present a method for homogenizing artificial materials composed of three-dimensional lattices of electromagnetic scatterers. The homogenization process is based on the non-spatially dispersive yet exact response of the discrete material, which includes all lattice interactions. By truncating to dipolar order, the material parameters of the homogeneous effective medium are determined without relying on any specific shape of a target object. Our results demonstrate that the effective homogeneous models accurately predict the electromagnetic response of finite objects made from the actual 3D lattice of scatterers, regardless of the object's shape. Our findings also demonstrate that the electromagnetic behavior of finite objects constructed from the real 3D lattice of scatterers can be accurately predicted by the corresponding effective homogeneous models, regardless of the target object's shape. The only significant approximation in this method is the truncation to dipolar order, which imposes a small difference between the exact description of the discrete material and its dipolar part. This condition is not a strict limitation on the $\mathbf{T}_{\mathrm{eff}}$ formalism but rather depends on the type of material and the choice of constitutive relation for the homogenization procedure.

We believe that our method for homogenizing artificial materials made from three-dimensional lattices of electromagnetic scatterers will prove valuable for designing photonic devices

and interpreting experimental measurements. This approach is especially well-suited for objects created using three-dimensional laser printing and those containing structured molecular materials. Going forward, a promising extension of this method would involve incorporating quadrupolar orders of the exact response in the homogeneous model. By doing so, we can expand the range of materials that can be homogenized while considering higher orders than the dipole.

5. Summary

In this thesis, a novel approach for describing homogenized metamaterials in an effective manner is presented. The method assumes a nonlocal response in order to determine effective properties that can replicate the full wave response of the actual metamaterial, including all its fine details, while still treating the metamaterial as homogeneous. To achieve this, nonlocal constitutive equations are advocated for, which go beyond the local equations that are commonly used to describe metamaterials. One of the key contributions of this work is the establishment of an understanding of these effective parameters and their meaning.

To linearly relate the displacement field $\mathbf{D}(\mathbf{k}, k_0)$ to the electric field of light $\mathbf{E}(\mathbf{k}, k_0)$, the thesis proposes the use of a Taylor expansion of the nonlocal kernel $\mathbf{R}(\mathbf{k}, k_0)$ in the Fourier space. Traditionally, the curl form of Maxwell's equations was used to express the constitutive relation through a Taylor expansion of the nonlocal response function, leading to differential operators also having the curl form. However, this consideration was never formally proven. As a result, the thesis presents its first contribution by proving, on analytical grounds, that the effective constitutive relation can only be reduced to curl-differential operators. The findings presented in this work have two main implications. Firstly, they provide a new justification for the definition of the curl-based special constitutive relation used in prior works [113, 118, 136]. Secondly, the tensor coefficients can be decomposed into dimensionless matrix coefficients and Levi-Civita tensors by transitioning to the dual space representations of both symmetric and antisymmetric tensors. The derivation is not rigorous, but the arguments can be proven, which opens up possibilities for further exploration. Finally, the new findings enable the tensor form of the constitutive relations to be rewritten into a more practical form, which facilitates the evaluation of the interface problem.

In Chapter 3, we study the dispersion relation by solving the wave equation for the general constitutive relation in the Fourier frequency space. This allows one to study the bulk properties of the MM in terms of an eigenmode analysis. Furthermore, to connect the constitutive relation with a prescribed incident plane wave, the interface conditions are derived using a generalized formulation of Maxwell's equations. Based on such interface conditions, Fresnel expressions are then obtained, which predict the amplitude of the reflected and transmitted plane wave when a slab of such a nonlocal metamaterial is illuminated. The comprehensive analytical expression derived in this chapter can be used to characterize both chiral and achiral (centrosymmetric) metamaterials. Our approach allows in-depth analysis of metamaterials with strong spatial dispersion and is applicable to a wide range of metamaterials.

Chapter 4 discusses two efficient methods for homogenization of optical metamaterials. The first method involves using parameter retrieval techniques to assign effective material parameters by treating the metamaterial as a bulk material. A Maxwell solver is introduced to predict the wave properties of the eigenmodes within the material domain, and a least-square fitting algorithm is coupled with it to conduct the parameter retrieval process.

With this procedure, we examine our initial example, which is a non-local isotropic metamaterial composed of scatterers that maintain either an electric dipole, electric quadrupole, or both an electric dipole and quadrupole moments, along with a magnetic dipole moment. We apply three homogenization models (WSD, SSD-γ, and SSD-τ) to homogenize the MM in this example. The quality of these homogenization models is assessed using an error function δ, which quantifies the difference between the predicted and actual reflection and transmission coefficients of the bulk material. Several conclusions are derived from this study.

Firstly, this study explores the use of non-local constitutive relations in homogenizing metamaterials and demonstrates the significance of effective material parameters in describing strong lattice effects that lead to non-local responses. The study also shows that the WSD model fails to capture the essence of spatial dispersion in the medium, while the SSD models perform relatively well. Secondly, we learn that, the analysis of the scattering behavior of the meta-atom can help determine the appropriate truncation order for the constitutive relation. For instance, to fully understand the optical behavior of a basic mesoscopic electric dipole system, the SSD-γ model is necessary, while the presence of

an intrinsic electric quadrupole moment requires the SSD-τ model to capture its optical behavior accurately at an effective level. Additionally, our observations indicated that the material parameter τ becomes more important as the complexity of the multipolar moments utilized to describe the meta-atoms increases. We attribute this phenomenon to the strong multipolar interaction present in the actual metamaterial, which manifests as strong spatial dispersion or non-locality in its homogeneous counterpart. Thus, understanding the multipolar moments carried by the meta-atom can aid in making an informed estimate of the appropriate truncation order for the constitutive relation for the material system under consideration.

As our second example of the parameter retrieval method, we examine the use of the non-local constitutive relation in homogenizing a metamaterial whose period-to-wavelength ratio is systematically varied. Our findings indicate that the non-local models are both stable and reliable in calculating the correct effective material parameters and optical coefficient at larger lattice periods. But for shorter lattice periods, even homogenizing with the non-local constitutive relation can be difficult and unreliable. This is due to the increased packing fraction in the metamaterial as the lattice period is reduced, resulting in an increase in near-field interactions among the meta-atoms that spread over a long range. Although this effect mimics the properties of strong spatial dispersion, our study suggests that even non-local models fail to account for the spread of excitations due to near-field effects. We finally conclude from this study that, there is a critical lattice period denoted by $\Lambda_{\text{critical}} = 200\,\text{nm}$ for the considered MM, below which homogenization makes no sense.

In the latter part of Chapter 4, we present a new semi-analytical method based on the T-matrix to homogenize a metamaterial. We introduce a new linear operator called the effective transition matrix, or $\mathbf{T}_{\text{eff}}$-matrix. The elements of the $\mathbf{T}_{\text{eff}}$-matrix linearly connect the multipolar expansion coefficient of the incident plane wave with wave vectors on the unit cell located at the origin and the multipolar expansion coefficient of the corresponding scattered plane waves up to an arbitrary multipolar order. Here, we develop the $\mathbf{T}_{\text{eff}}$-matrix to encompass the full material properties, including interactions, while remaining independent of any lattice information such as shape. Thus, a complete $\mathbf{T}_{\text{eff}}$-matrix provides a comprehensive electromagnetic characterization of the periodic metamaterial under consideration. One major advantage of using the $\mathbf{T}_{\text{eff}}$ method instead of parameter retrieval methods is that it allows for the calculation of effective material parameters

without the need for a specific target object, as long as the T-matrix of the individual meta-atoms is fully known. Although the $\mathbf{T}_{\text{eff}}$-matrix is exact upto an arbitrary multipolar order, we restrict our analysis to the local constitutive relation for convenience. Thus the only significant approximation in this method, at the moment, is the truncation of the $\mathbf{T}_{\text{eff}}$-matrix to dipolar order, which imposes a small difference between the exact description of the discrete material and its dipolar part.

In addition, we demonstrate the utility of the $\mathbf{T}_{\text{eff}}$-method by homogenizing a 3D isotropic metamaterial composed of gold nano-spheres. The effective material parameters ε and μ, as well as the corresponding reflection and transmission coefficients, are computed and compared to those obtained from a complete wave solution. The results show that the effective homogeneous models accurately predict the electromagnetic response of the actual metamaterial. Furthermore, we utilize the effective material parameters calculated previously to construct a new target object with an approximate spherical shape of radius r. To validate our findings, we calculate the scattering cross section of the actual metamaterial using CELES and compare it with that of the homogeneous equivalent computed using the $\mathbf{T}_{\text{eff}}$-matrix. The two cross sections are found to be in good agreement, indicating that the homogeneous medium can be used to construct a new lattice. The $\mathbf{T}_{\text{eff}}$ method shows great potential in designing and characterizing metamaterials with considerably less effort.

The technique and results presented here are shown to expand the capabilities of the effective medium theory into the strong spatial dispersion regime. Additionally, the tools and methods developed in this project can be readily applied to the characterization of metamaterials exhibiting sixth-order spatial dispersion.

An interesting avenue for future research, building upon the findings of this thesis, would involve investigating spatio-temporal metamaterials that exhibit either spatial non-locality, temporal non-locality, or both. Local time-varying metamaterials have demonstrated significant potential, and we anticipate that expanding into the non-local regime would reveal novel and compelling physics. Another possible field for exploration, would be to extend the $\mathbf{T}_{\text{eff}}$ method to encompass non-local effects, which would prove beneficial in dealing with meta-atoms featuring arbitrarily large multipolar orders. Additionally, the techniques presented in this thesis can be further applied within the framework of machine learning to envision a purely non-local material that could uncover exciting new physics.

Appendix

A. Expressing Levi-Civita in Terms of the Rotation Matrix

Expressing the Levi-Civita symbol ϵ in terms of the rotation matrix $\bar{R}(\theta)$ is a bit tricky. This is because the $\bar{R}(\theta)$ contains both rotation and reflection components, while the Levi-Civita is purely a measure of orientation. Nonetheless, one possible expression for the 3D Levi-Civita ϵ_{ijk} in the Cartesian basis can be written as

$$\epsilon_{ijk} = \frac{1}{2}\Big(\Big[\bar{R}_x^{\mathrm{T}}(\theta)\mathrm{S}_x\Big] \otimes \Big[\bar{R}_y^{\mathrm{T}}(\theta)\mathrm{S}_y\Big] \otimes \Big[\bar{R}_z^{\mathrm{T}}(\theta)\mathrm{S}_z\Big]\Big) \quad . \tag{A.1}$$

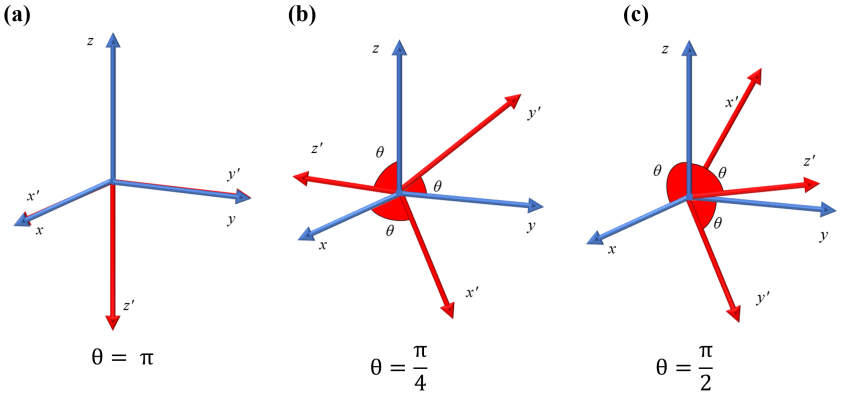

Figure A.1.: In this figure, we see the effect of the rotation matrix $\bar{R}_i(\theta)$ on a 3D vector $\mathbf{r} = x\ \hat{x} + y\ \hat{y} + z\ \hat{z}$, where $\hat{x}$, $\hat{y}$, and $\hat{z}$ are the unit vectors along the Cartesian coordinate axes. The rotation matrix $\mathbf{R_i}(\theta)$ represents a rotation of angle θ around an axis of rotation n with unit vector components $\mathbf{n} = (n_x, n_y, n_z)$ [204]. The action of the rotation matrix on the vector $\mathbf{r}$ is $\bar{R}_i.\mathrm{n}_i$ corresponding to the change in the orientation in space $w.r.t$ the rotation axis specified by n. This operation is also equivalent to the action of the Levi-Civita operator ϵ_{ijk}, which can be expressed in terms of the rotation matrix.

Here, using the right-hand rule, the basic rotation matrix $\bar{R}_i(\theta)$ with $i = \{x, y, z\}$ indicating

the axis of rotation, that rotates any vector by an angle θ can be written as a matrix:

$$\begin{aligned}
\bar{R}_x(\theta) &= \begin{pmatrix} 1 & 0 & 0 \\ 0 & \cos(\theta) & -\sin(\theta) \\ 0 & \sin(\theta) & \cos(\theta) \end{pmatrix} \\
\bar{R}_y(\theta) &= \begin{pmatrix} \cos(\theta) & 0 & \sin(\theta) \\ 0 & 1 & 0 \\ -\sin(\theta) & 0 & \cos(\theta) \end{pmatrix} \\
\bar{R}_z(\theta) &= \begin{pmatrix} \cos(\theta) & -\sin(\theta) & 0 \\ \sin(\theta) & \cos(\theta) & 0 \\ 0 & 0 & 1 \end{pmatrix} \\
\mathrm{S} &= \begin{pmatrix} 0 & -n_z & n_y \\ n_z & 0 & -n_x \\ -n_2 & n_x & 0 \end{pmatrix}
\end{aligned} \tag{A.2}$$

and the S matrix contains the components n_i, with $i = \{x, y, z\}$ of the unit vector $\mathbf{n}$ with $|\mathbf{n}| = \mathrm{n}_x^2 + \mathrm{n}_y^2 + \mathrm{n}_z^2 = 1$ that defines the axis of rotation. The illustration of the action of the rotation operator $\bar{R}(\theta)$ is given in Fig. A.1.

Before we move forward, let us also remark on some useful properties of the Levi-Civita symbol that will aid us:

1. The Levi-Civita symbol is also an intrinsic tensor field of a manifold, meaning that it is independent of any particular choice of the coordinate system if the basis vectors of the tangent space are orthonormal with respect to the metric tensor $\mathbf{g}$ for the chosen orientation [*Section 21.5,* [205]. It is a completely antisymmetric tensor of rank d (where d is the dimension of the manifold), and it is defined in terms of the metric tensor and its derivatives.

2. Transpose property of the 3D Levi-Civita indices follow

$$\epsilon_{ijk} = \begin{cases} 1 & \text{if } \sigma(i,j,k) \text{ is even} \\ -1 & \text{if } \sigma(i,j,k) \text{ is odd} \\ 0 & \text{if any index repeat.} \end{cases} \tag{A.3}$$

3. The Levi-Civita symbol and the Kronecker delta are related by the equation:

$$\epsilon_{ijk}\epsilon_{lmn} = \begin{vmatrix} \delta_{il} & \delta_{im} & \delta_{in} \\ \delta_{jl} & \delta_{jm} & \delta_{jn} \\ \delta_{kl} & \delta_{km} & \delta_{kn} \end{vmatrix}$$

Using this relationship, we can derive the following expression:

$$\sum_{l=1}^{3} \epsilon_{ijl}\epsilon_{mnl} = \delta_{jn}\delta_{nj} - \delta_{im}\delta_{mi}$$

Consequently, any multiplication of an even number of Levi-Civita symbols must yield a symmetric result.

B. Centrosymmetric Metamaterial

B.1. Energy Flux Associated with the SSD Models: Poynting Vector Formulation

In this subsection of the appendix, we provide a brief summary of the derivation of the Poynting vector $\mathbf{S}$ for both the TE and TM polarization. We focus on obtaining the energy flux through a plane in normal direction $S_z = \mathbf{S} \cdot \hat{\mathrm{z}}$ when the wave propagates in the $\hat{\mathrm{z}}$ direction.

Assuming a plane wave *ansatz*, $\mathbf{E}(\mathbf{r},t) = \Re[\mathbf{E}(\mathbf{r})e^{-\mathrm{i}k_0 t}]$ and $\mathbf{H}(\mathbf{r},t) = \Re[\mathbf{H}(\mathbf{r})e^{-\mathrm{i}k_0 t}]$ where $\mathbf{E}(\mathbf{r})$ and $\mathbf{H}(\mathbf{r})$ are generally complex, we have the expression for the time-averaged power flow over a complete time cycle T in the time domain can be expressed as:

$$\langle \mathbf{S}(\mathbf{r},t) \rangle = \frac{1}{\mathrm{T}} \int_{\mathrm{T}} (\mathbf{E}(\mathbf{r},t) \times \mathbf{H}(\mathbf{r},t)) \mathrm{d}t. \tag{B.1}$$

In the frequency domain, the expression for the Fourier transform of the time-averaged power flow becomes [*section 6.9,* [115]]:

$$\langle \mathbf{S}(\mathbf{k}, k_0) \rangle = \frac{1}{2} \Re(\mathbf{E}(\mathbf{k}, k_0) \times \mathbf{H}^*(\mathbf{k}, k_0)). \tag{B.2}$$

This corresponds to the intensity $I = \langle \mathbf{S}(\mathbf{k}, k_0) \rangle$.

We begin by using Ampere's law to derive the expression for $\langle S_z \rangle$. Ampere's law is given by

$$\mathrm{i}\mathbf{k} \times \mathbf{H}(\mathbf{k}, k_0) + \mathrm{i}k_0 \mathbf{R}(\mathbf{k}, k_0)\mathbf{E}(\mathbf{k}, k_0) = 0, \tag{B.3}$$

We then substitute the expression for $\mathbf{R}(\mathbf{k}, k_0)$ corresponding to the choice of the SSD model. In our calculation, we use the matrix form of the curl operator

$$\mathrm{i}\mathbf{k}\times = \mathrm{i} \begin{pmatrix} 0 & -k_z & k_y \\ k_z & 0 & -k_x \\ -k_y & k_x & 0 \end{pmatrix}, \tag{B.4}$$

Consider the first case of TM polarization, where we have two electric field components E_x and E_z, and one magnetic field component H_y. In this case, the $\hat{\mathrm{z}}$ component of the Poynting vector can be expressed as:

$$\langle S_z(k_0) \rangle = \frac{1}{2} \Re(E_x(k_0) {H_y}^*(k_0)). \tag{B.5}$$

Thus, we can solve Equation B.2 for the H_y component as

$$H_y = E_x \frac{\left(k_0^2 \mu_y p_0^{\mathrm{TM}} + \left(k_x^2 \epsilon_x + k_z^2 \epsilon_z\right)(\mu_y - 1)\right)}{k_z k_0 \mu_y \epsilon_z} \text{ for SSD-}\gamma \text{ model,} \tag{B.6}$$

$$H_y = E_x \frac{\left(k_0^2 \mu_y p_0^{\mathrm{TM}} + k_0^2 \mu_y q_0^{\mathrm{TM}} \left(k_x^2 \epsilon_x + k_z^2 \epsilon_z\right)(\mu_y - 1)\right)}{k_z k_0 \mu_y \epsilon_z} \text{ for SSD-}\tau \text{ model} \tag{B.7}$$

where,

$$\begin{aligned} p_0^{\mathrm{TM}} &= k_x^4 \gamma_z \epsilon_x + k_z^4 \gamma_x \epsilon_z + k_x^2 k_z^2 \left(\gamma_x \epsilon_x + \gamma_z \epsilon_z\right) + \epsilon_x \epsilon_z \\ q_0^{\mathrm{TM}} &= \left(k_x^2 + k_z^2\right)^2 \left(k_x^2 \varepsilon_x + k_z^2 \varepsilon_z\right) \tau_y. \end{aligned} \tag{B.8}$$

Therefore, the time average energy flux component for the considered SSD model can be written as

$$\langle S_z \rangle = |E_x|^2 \, \Re \left(\frac{\left(k_0^2 \mu_y p_0^{\mathrm{TM}} + \left(k_x^2 \epsilon_x + k_z^2 \epsilon_z \right) \left(\mu_y - 1 \right) \right)}{2 k_z k_0 \mu_y \epsilon_z} \right) \text{ for SSD-}\gamma \text{ model,} \tag{B.9}$$

$$\langle S_z \rangle = |E_x|^2 \, \Re \left(\frac{k_0^2 \mu_y \left(p_0^{\mathrm{TM}} + q_0^{\mathrm{TM}} \right) + \left(k_x^2 \epsilon_x + k_z^2 \epsilon_z \right) \left(\mu_y - 1 \right)}{2 k_z k_0 \mu_y \epsilon_z} \right) \text{ for SSD-}\tau \text{ model.} \tag{B.10}$$

Note, we have dropped the arguments associated with all the components for readability.

Analogously, we can also derive the expressions for the TE polarization, which involves an electric field component E_y and two magnetic field components H_x and H_z, with the propagation direction assumed to be along $\hat{z}$. Following Eq. (B.2) we may express the Poynting vector component $\langle S_z \rangle$ as:

$$\langle S_z(\mathbf{k}, k_0) \rangle = -\frac{1}{2} \Re (E_y(\mathbf{k}, k_0) {H_x}^*(\mathbf{k}, k_0)). \tag{B.11}$$

By solving Eq. (B.3) with the appropriate expression for $\mathbf{R}(\mathbf{k}, k_0)$ based on the selected SSD model, we can determine the magnetic field component H_y,

$$H_y = E_y \frac{k_0 k_z}{k_0^2 (k_x^2 + k_z^2)} \left\{ p_0^{\mathrm{TE}} - \left(k_x^2 + k_z^2 \right) \right\} \text{ for SSD-}\gamma, \tag{B.12}$$

$$H_y = E_y \frac{k_0 k_z}{k_0^2 (k_x^2 + k_z^2)} \left\{ p_0^{\mathrm{TE}} - q_0^{\mathrm{TE}} - \left(k_x^2 + k_z^2 \right) \right\} \text{ for SSD-}\tau, \tag{B.13}$$

where we have

$$\begin{aligned} p_0^{\mathrm{TE}} &= \left(k_x^2 \mu_x + k_z^2 \mu_z \right) - k_0^2 \mu_x \mu_z (k_x^2 + k_z^2)^2 \gamma_y + k_0^2 \mu_x \mu_y, \epsilon_y \\ q_0^{\mathrm{TE}} &= -k_0^2 \mu_x \mu_z (k_x^2 + k_z^2)(k_x^2 \tau_z + k_z^2 \tau_x). \end{aligned} \tag{B.14}$$

Thus, we can express the expression for $\langle S_z \rangle$ for the different SSD models when the incident polarization is TE as follows:

$$\langle S_z \rangle = |E_y|^2 \, \Re \left(\frac{k_0 k_z}{2 k_0^2 (k_x^2 + k_z^2)} \left\{ p_0^{\mathrm{TE}} - \left(k_x^2 + k_z^2 \right) \right\} \right) \text{ for SSD-}\gamma, \tag{B.15}$$

$$\langle S_z \rangle = |E_y|^2 \, \Re \left(\frac{k_0 k_z}{2 k_0^2 (k_x^2 + k_z^2)} \left\{ p_0^{\mathrm{TE}} - q_0^{\mathrm{TE}} - \left(k_x^2 + k_z^2 \right) \right\} \right) \text{ for SSD-}\tau, \tag{B.16}$$

B.2. Fresnel Expressions: Calculating Reflection and Transmission Coefficients

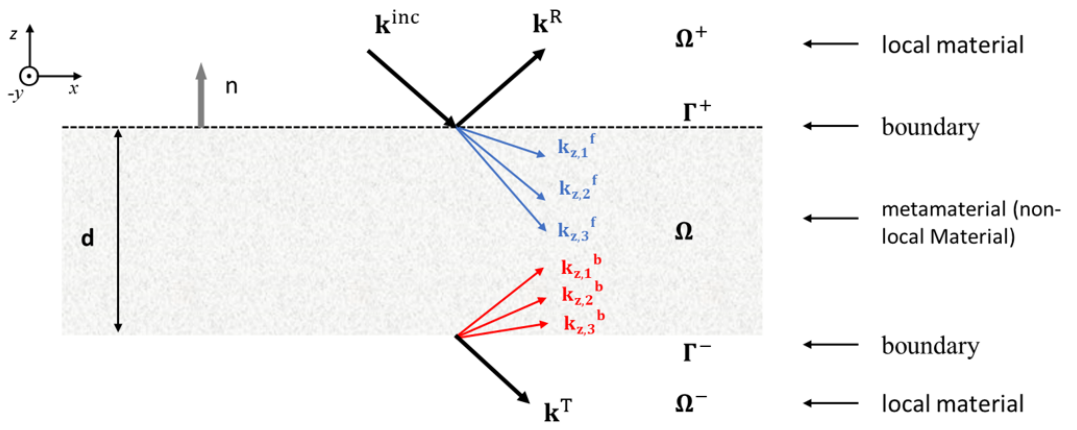

Figure B.2.: General scenario considered where a slab Ω divides a substrate and cladding into two distinct half-spaces Ω^+ and Ω^- separated by the boundary Γ_1 and Γ_2, respectively. In this thesis, we consider only symmetric configurations, *i.e.,* both the substrate and the cladding are made from the same material. Additionally, we restrict ourselves to systems where the host medium is an isotropic homogeneous local medium characterized by a permittivity ε and permeability $\mu = 1$, containing the nonlocal MM in the domain Ω.

The figure Fig. B.2 depicts a scenario where a slab Ω of thickness d separates a substrate and cladding into two distinct half-spaces, Ω^+ and Ω^-, respectively. The substrate and cladding are identical materials and can be described generally as a homogeneous isotropic local medium characterized by a nondispersive permittivity ε and permeability of $\mu = 1$. The figure shows the boundaries that define the interfaces between the substrate, slab, and cladding. In this setup, the nonlocal MM is contained within the domain Ω. Finally, the figure shows the backward propagating modes excited at the second interface contributing to the total reflection in the cladding.

Illuminating with TM-Polarization

Without loss of generality, we assume that the incidence plane is the zx-plane as before with the incident wave vector $\mathbf{k}^{\text{inc}} = (k_x, 0, k_z^{\text{inc}})$ with z-direction being the principle propagation direction. The electric field lie on the incident plan, such that $\mathbf{E}^{\text{inc}}(\mathbf{r}, k_0) = (E_x^{\text{inc}}(k_0)\ \hat{\mathrm{x}}, E_z^{\text{inc}}(k_0)\ \hat{\mathrm{z}})\mathrm{e}^{\mathrm{i}\mathbf{k}^{\text{inc}}\cdot\mathbf{r}}$ for $\mathbf{r} \in \Omega^+$. Consequently, the reflected and transmitted fields are defined similarly with the filed vector $\mathbf{E}^{\text{R}}(\mathbf{r}, k_0) = \left(E_x^{\text{R}}(k_0)\ \hat{\mathrm{x}}, E_z^{\text{R}}(k_0)\ \hat{\mathrm{z}}\right)\mathrm{e}^{\mathrm{i}\mathbf{k}^{\text{R}}\cdot\mathbf{r}}$ for $\mathbf{r} \in \Omega^+$ and $\mathbf{E}^{\text{T}}(\mathbf{r}, k_0) = \left(E_x^{\text{T}}(k_0)\ \hat{\mathrm{x}}, E_z^{\text{T}}(k_0)\ \hat{\mathrm{z}}\right)\mathrm{e}^{\mathrm{i}\mathbf{k}^{\text{T}}\cdot(\mathbf{r}-d\ \hat{\mathrm{z}})}$ for $\mathbf{r} \in \Omega^-$ with the corresponding wave vectors $\mathbf{k}^{\text{R}} = \left(k_x, 0, k_z^{\text{R}}\right)$ and $\mathbf{k}^{\text{T}} = \left(k_x, 0, k_z^{\text{T}}\right)$ respectively. Notice that we have considered

the phase shift acquired by the transmitted field as the waves within the homogeneous medium travel the thickness $|z| = \mathrm{d}$ from the Γ^+ to Γ^-.

Within the slab Ω, the metamaterial is described by the constitutive relation Eq. (2.28). In this setting, we know that each additional nonlocal parameter advances the dispersion relation and excites additional modes inside the medium, which are pairwise forward and backward propagating. In this sense, for the TM- polarization, we have the total field inside the medium as

$$\mathbf{E}^{\mathrm{slab}}(\mathbf{r}, k_0) = \sum_{i=1}^{N} \left(\left\{ \mathrm{E}^f_{x,i}(k_0) + \mathrm{E}^b_{x,i}(k_0) \right\} \hat{\mathrm{x}} + \left\{ \mathrm{E}^f_{z,i}(k_0) + \mathrm{E}^b_{z,i}(k_0) \right\} \hat{\mathrm{z}} \right) \mathrm{e}^{\mathrm{i}\mathbf{k}_i \cdot r} \tag{B.17}$$

In our scenario, only the incident field is the known quantity, all the other field amplitudes have to be deduced from the interface conditions IC 1-IC 4.

Additionally, for the case of TM-polarization, the electric field components/eigenmodes can be related through the Gauss divergence law $\nabla \cdot \mathbf{D} = 0$*, as

$$k_x \mathrm{E}_x + k_z \mathrm{E}_z = 0 \implies \mathrm{E}_x = -\frac{k_z}{k_x} \mathrm{E}_z \quad \text{for } \Omega^{\pm} \tag{B.18}$$

$$\varepsilon_x k_x \mathrm{E}^{f/b}_{x,i} + \varepsilon_z k^{f/b}_{z,i} \mathrm{E}^{f/b}_{z,i} = 0 \implies \mathrm{E}^{f/b}_{x,i} = -\frac{\varepsilon_z}{\varepsilon_x} \frac{k^{f/b}_{z,i}}{k_x} \mathrm{E}^{f/b}_{z,i} \quad \text{for } \Omega, \tag{B.19}$$

assuming that all field components and material parameters follow the argument (k_0).

where the label f/b represent the forward or backward propagating eigenmodes and $i = \{1 \dots 2N\}$ correspond to the $2N$ order of the polynomial dispersion relation.

A quantity called the Fresnel matrix is used to relate the unknown fields and the input vector, $\underline{\mathbf{E}} = \left(\mathrm{E}^{\mathrm{R}}_z, \mathrm{E}^{\mathrm{f}}_{z,1}, \mathrm{E}^{\mathrm{f}}_{z,2}, \mathrm{E}^{\mathrm{f}}_{z,3}, \mathrm{E}^{\mathrm{b}}_{z,1}, \mathrm{E}^{\mathrm{b}}_{z,2}, \mathrm{E}^{\mathrm{b}}_{z,3}, \mathrm{E}^{\mathrm{T}}_z \right)$ and $\underline{\mathbf{I}} = -\mathrm{E}^{\mathrm{inc}}_z \left(k^{\mathrm{inc}}_z, \left(\mathbf{k}^{\mathrm{R}} \right)^2, 0, 0, 0, 0, 0, 0 \right)^{\mathrm{T}}$, respectively, via the equation

$$\mathbf{F}^{\mathrm{SSD,TM}} \cdot \underline{\mathbf{E}} = \underline{\mathbf{I}}. \tag{B.20}$$

The construction of the Fresnel matrix is to summarize the dispersion relations and interface conditions. The first three rows correspond to the interface conditions at the first interface Γ^+, while the last three rows correspond to the second interface Γ^-. The first and last columns contain coefficients for the reflected and transmitted fields, respectively. Zeros

*It should be noted that only the permittivity tensor is relevant here, as all coefficients associated with the curl disappear due to the fact that $\nabla \cdot (\nabla \times \mathbf{F}) = 0$ for any vector $\mathbf{F}$.

appear where there is no reflection or transmission. The middle four columns represent the field amplitudes within the slab, with the first two columns containing the forward propagating modes and the last two columns containing the backward propagating modes. The backward modes are important for the correct calculation of the reflection coefficient. The Fresnel matrix for the SSD-τ model reads,

$$\mathbf{F}^{\mathrm{SSD,TM}} = \begin{pmatrix} -k_z^{\mathrm{R}} & \mathrm{A}_1 & \mathrm{A}_2 & \mathrm{A}_3 & \mathrm{A}_4 & \mathrm{A}_5 & \mathrm{A}_6 & 0 \\ \left(\mathbf{k}^{\mathrm{R}}\right)^2 & \mathrm{B}_1 & \mathrm{B}_2 & \mathrm{B}_3 & \mathrm{B}_4 & \mathrm{B}_5 & \mathrm{B}_6 & 0 \\ 0 & \mathrm{C}_1 & \mathrm{C}_2 & \mathrm{C}_3 & \mathrm{C}_4 & \mathrm{C}_5 & \mathrm{C}_6 & 0 \\ 0 & \mathrm{D}_1 & \mathrm{D}_2 & \mathrm{D}_3 & \mathrm{D}_4 & \mathrm{D}_5 & \mathrm{D}_6 & 0 \\ 0 & \mathrm{A}_1\mathrm{e}^{\mathrm{i}k_{z,1}d} & \mathrm{A}_2\mathrm{e}^{\mathrm{i}k_{z,2}d} & \mathrm{A}_3\mathrm{e}^{\mathrm{i}k_{z,3}d} & \mathrm{A}_4\mathrm{e}^{\mathrm{i}k_{z,4}d} & \mathrm{A}_5\mathrm{e}^{\mathrm{i}k_{z,5}d} & \mathrm{A}_6\mathrm{e}^{\mathrm{i}k_{z,6}d} & k_z^{\mathrm{T}} \\ 0 & \mathrm{B}_1\mathrm{e}^{\mathrm{i}k_{z,1}d} & \mathrm{B}_2\mathrm{e}^{\mathrm{i}k_{z,2}d} & \mathrm{B}_3\mathrm{e}^{\mathrm{i}k_{z,3}d} & \mathrm{B}_4\mathrm{e}^{\mathrm{i}k_{z,4}d} & \mathrm{B}_5\mathrm{e}^{\mathrm{i}k_{z,5}d} & \mathrm{B}_6\mathrm{e}^{\mathrm{i}k_{z,6}d} & \left(\mathbf{k}^{\mathrm{T}}\right)^2 \\ 0 & \mathrm{C}_1\mathrm{e}^{\mathrm{i}k_{z,1}d} & \mathrm{C}_2\mathrm{e}^{\mathrm{i}k_{z,2}d} & \mathrm{C}_3\mathrm{e}^{\mathrm{i}k_{z,3}d} & \mathrm{C}_4\mathrm{e}^{\mathrm{i}k_{z,4}d} & \mathrm{C}_5\mathrm{e}^{\mathrm{i}k_{z,5}d} & \mathrm{C}_6\mathrm{e}^{\mathrm{i}k_{z,6}d} & 0 \\ 0 & \mathrm{D}_1\mathrm{e}^{\mathrm{i}k_{z,1}d} & \mathrm{D}_2\mathrm{e}^{\mathrm{i}k_{z,2}d} & \mathrm{D}_3\mathrm{e}^{\mathrm{i}k_{z,3}d} & \mathrm{D}_4\mathrm{e}^{\mathrm{i}k_{z,4}d} & \mathrm{D}_5\mathrm{e}^{\mathrm{i}k_{z,5}d} & \mathrm{D}_6\mathrm{e}^{\mathrm{i}k_{z,6}d} & 0 \end{pmatrix} \tag{B.21}$$

Here the coefficients that appear in the Fresnel matrix read,

$$\mathrm{A}_i = \frac{\varepsilon_z(k_0)}{\varepsilon_x(k_0)} k_{z,i}, \tag{B.22}$$

$$\mathrm{B}_i = \left(k_x^2 + \frac{\varepsilon_z(k_0)}{\varepsilon_x(k_0)} k_{z,i}^2\right)\left(k_0^2\left\{k_{z,i}^2\gamma_x(k_0) + k_x^2\gamma_z(k_0) + \left(k_x^2 + k_{z,i}^2\right)^2\tau_y(k_0)\right\} - \mu^{-1}(k_0)\right), \tag{B.23}$$

$$\mathrm{C}_i = -k_z\left(k_x^2 + \frac{\varepsilon_z(k_0)}{\varepsilon_x(k_0)} k_{z,i}^2\right)\left\{\gamma_x(k_0) + \left(k_x^2 + k_{z,i}^2\right)\tau_y(k_0)\right\}, \tag{B.24}$$

$$\mathrm{D}_i = \left(k_x^2 + \frac{\varepsilon_z(k_0)}{\varepsilon_x(k_0)} k_{z,i}^2\right)\left\{\left(k_x^2 + k_{z,i}^2\right)\tau_y(k_0)\right\}. \tag{B.25}$$

The wave vectors and their $\hat{z}$ components are given by the dispersion relation governed by the local constitutive relations for the isotropic homogeneous surrounding medium characterized by $\varepsilon(k_0)$:

$$(k_z^{\mathrm{inc}})^2 = \varepsilon(k_0)k_0^2 - k_x^2, \tag{B.26}$$

with $k_z^{\mathrm{R}} = -k_z^{\mathrm{inc}}$ and $k_z^{\mathrm{T}} = -k_z^{\mathrm{inc}}$. Finally, the complex reflection and transmission coefficients are obtained by inverting the Fresnel matrix $\mathbf{F}^{\mathrm{SSD,TM}}$ and multiplying with the

input vector $\underline{\mathbf{I}}$ and respectively taking the first and last component, as

$$\mathbf{R}^{\mathrm{SSD}-\tau,\mathrm{TM}} = \left[\left(\mathbf{F}^{\mathrm{SSD,TM}}\right)^{-1} \cdot \underline{\mathbf{I}} \right]_1, \tag{B.27}$$

$$\mathbf{T}^{\mathrm{SSD}-\tau,\mathrm{TM}} = \left[\left(\mathbf{F}^{\mathrm{SSD,TM}}\right)^{-1} \cdot \underline{\mathbf{I}} \right]_8. \tag{B.28}$$

Correspondingly, the same procedure can be repeated with the limiting conditions $\tau \to 0$ giving a rank 6 Fresnel matrix for the SSD-γ model and then the limit $\{\tau, \gamma\} \to 0$ giving the rank 4 Fresnel matrix for the WSD model to calculate the corresponding complex reflection and transmission coefficients.

For completeness, we next discuss the case for an incident TE polarization field.

Illuminating with TE-Polarization

In the case of having an incident TE polarization with the wave vector components $\mathbf{k} = (k_x, 0, k_z)$, we have two magnetic components H_x, H_z and one electric component E_y. Since we only have one electric field component, it is quite straightforward to write the incident as $\mathbf{E}^{\mathrm{inc}}(\mathbf{r}, k_0) = \mathrm{E}_{0,y} \mathrm{e}^{\mathrm{i}\mathbf{k}^{\mathrm{inc}}\cdot\mathbf{r}} \hat{\mathrm{y}}$, the reflection $\mathbf{E}^{\mathrm{R}}(\mathbf{r}, k_0)$ and transmission $\mathbf{E}^{\mathrm{T}}(\mathbf{r}, k_0)$ field vectors follow correspondingly.

Within the slab Ω, we have the additional eigenmodes contributing to the propagating electric field as

$$\mathbf{E}^{\mathrm{slab}}(\mathbf{r}, k_0) = \sum_{i=1}^{2N} \left\{ \mathrm{E}^{f}_{y,i}(k_0) + \mathrm{E}^{b}_{y,i}(k_0) \right\} \mathrm{e}^{\mathrm{i}\mathbf{k}_i\cdot\mathbf{r}}\ \hat{\mathrm{y}}. \tag{B.29}$$

On computing the interface conditions IC 1-IC 4 for the wave vector components thus obtained for the TE illumination, we have the corresponding Fresnel matrix

$$\mathbf{F}^{\mathrm{SSD,TE}} = \begin{pmatrix}
1 & \mathrm{A}_1 & \mathrm{A}_2 & \mathrm{A}_3 & \mathrm{A}_4 & \mathrm{A}_5 & \mathrm{A}_6 & 0 \\
k_z^{\mathrm{R}} & \mathrm{B}_1 & \mathrm{B}_2 & \mathrm{B}_3 & \mathrm{B}_4 & \mathrm{B}_5 & \mathrm{B}_6 & 0 \\
0 & \mathrm{C}_1 & \mathrm{C}_2 & \mathrm{C}_3 & \mathrm{C}_4 & \mathrm{C}_5 & \mathrm{C}_6 & 0 \\
0 & \mathrm{D}_1 & \mathrm{D}_2 & \mathrm{D}_3 & \mathrm{D}_4 & \mathrm{D}_5 & \mathrm{D}_6 & 0 \\
0 & \mathrm{A}_1\mathrm{e}^{\mathrm{i}k_{z,1}d} & \mathrm{A}_2\mathrm{e}^{\mathrm{i}k_{z,2}d} & \mathrm{A}_3\mathrm{e}^{\mathrm{i}k_{z},3d} & \mathrm{A}_4\mathrm{e}^{\mathrm{i}k_{z,4}d} & \mathrm{A}_5\mathrm{e}^{\mathrm{i}k_{z,5}d} & \mathrm{A}_6\mathrm{e}^{\mathrm{i}k_{z,6}d} & 1 \\
0 & \mathrm{B}_1\mathrm{e}^{\mathrm{i}k_{z,1}d} & \mathrm{B}_2\mathrm{e}^{\mathrm{i}k_{z,2}d} & \mathrm{B}_3\mathrm{e}^{\mathrm{i}k_{z,3}d} & \mathrm{B}_4\mathrm{e}^{\mathrm{i}k_{z,4}d} & \mathrm{B}_5\mathrm{e}^{\mathrm{i}k_{z,5}d} & \mathrm{B}_6\mathrm{e}^{\mathrm{i}k_{z,6}d} & k_z^{\mathrm{T}} \\
0 & \mathrm{C}_1\mathrm{e}^{\mathrm{i}k_{z,1}d} & \mathrm{C}_2\mathrm{e}^{\mathrm{i}k_{z,2}d} & \mathrm{C}_3\mathrm{e}^{\mathrm{i}k_{z,3}d} & \mathrm{C}_4\mathrm{e}^{\mathrm{i}k_{z,4}d} & \mathrm{C}_5\mathrm{e}^{\mathrm{i}k_{z,5}d} & \mathrm{C}_6\mathrm{e}^{\mathrm{i}k_{z,6}d} & 0 \\
0 & \mathrm{D}_1\mathrm{e}^{\mathrm{i}k_{z,1}d} & \mathrm{D}_2\mathrm{e}^{\mathrm{i}k_{z,2}d} & \mathrm{D}_3\mathrm{e}^{\mathrm{i}k_{z,3}d} & \mathrm{D}_4\mathrm{e}^{\mathrm{i}k_{z,4}d} & \mathrm{D}_5\mathrm{e}^{\mathrm{i}k_{z,5}d} & \mathrm{D}_6\mathrm{e}^{\mathrm{i}k_{z,6}d} & 0
\end{pmatrix} \tag{B.30}$$

Once again, the Fresnel matrix relates the unknown fields and the input vector, $\underline{\mathbf{E}} = \left(\mathrm{E}_y^{\mathrm{R}}, \mathrm{E}_{y,1}^{\mathrm{f}}, \mathrm{E}_{y,2}^{\mathrm{f}}, \mathrm{E}_{y,3}^{\mathrm{f}}, \mathrm{E}_{y,1}^{\mathrm{b}}, \mathrm{E}_{y,2}^{\mathrm{b}}, \mathrm{E}_{y,3}^{\mathrm{b}}, \mathrm{E}_y^{\mathrm{T}}\right)$ and $\underline{\mathbf{I}} = -\mathrm{E}_y^{\mathrm{inc}}\left(1, \mathbf{k}_z^{\mathrm{inc}}, 0, 0, 0, 0, 0, 0\right)^{\mathrm{T}}$, respectively, via the equation

$$\mathbf{F}^{\mathrm{SSD,TE}} \cdot \underline{\mathbf{E}} = \underline{\mathbf{I}}. \tag{B.31}$$

Now the coefficients that appear in the Fresnel matrix is read as,

$$\mathrm{A}_i = 1, \tag{B.32}$$

$$\mathrm{B}_i = -k_z\Big(\mu^{-1}(k_0) - k_0^2\Big(k_x^2 + k_z^2\Big)\Big(\gamma_y(k_0) + k_z^2\tau_x(k_0) + k_x^2\tau_z(k_0)\Big)\Big), \tag{B.33}$$

$$\mathrm{C}_i = \Big(k_x^2 + k_z^2\Big)\Big(\gamma_y(k_0) + k_z^2\tau_x(k_0) + k_x^2\tau_z(k_0)\Big)), \tag{B.34}$$

$$\mathrm{D}_i = k_z\Big(k_x^2 + k_z^2\Big)\tau_x(k_0). \tag{B.35}$$

The component k_z^{R} and k_z^{T} are given by the dispersion relation governed by the local constitutive relations: $(k_z^{\mathrm{inc}})^2 = \varepsilon k_0^2 - k_x^2$ with $k_z^{\mathrm{R}} = -k_z^{\mathrm{inc}}$ and $k_z^{\mathrm{T}} = -k_z^{\mathrm{inc}}$. Finally, the complex reflection and transmission coefficients are obtained by inverting the Fresnel matrix $\mathbf{F}^{\mathrm{SSD,TE}}$ and multiplying with the input vector $\underline{\mathbf{I}}$ and respectively taking the first and last component, as

$$\mathbf{R}^{\mathrm{SSD}-\tau,\mathrm{TE}} = \left[\ \left(\mathbf{F}^{\mathrm{SSD,TE}}\right)^{-1} \cdot \underline{\mathbf{I}}\right]_1 \tag{B.36}$$

$$\mathbf{T}^{\mathrm{SSD}-\tau,\mathrm{TE}} = \left[\ \left(\mathbf{F}^{\mathrm{SSD,TE}}\right)^{-1} \cdot \underline{\mathbf{I}}\right]_8 . \tag{B.37}$$

C. Chiral Metamaterial

C.1. Derivation of the General Interface Condition

To derive the interface conditions, a thorough understanding of the Helmholtz wave equation is necessary, particularly its generalized form. The Maxwell equations consist of four coupled partial differential equations for the fields $\mathbf{D}$, $\mathbf{B}$, $\mathbf{E}$, and $\mathbf{H}$, as well as their spatial derivatives. The solutions to these equations must ensure a well-defined energy, which is contingent on the four vectors $(\mathbf{D}, \mathbf{B}, \mathbf{E}, \mathbf{H}) \in \mathbf{L}^2(\Omega)$, $\nabla \cdot \mathbf{D} \in \mathbf{L}^2(\Omega)$, $\nabla \cdot \mathbf{B} \in \mathbf{L}^2(\Omega)$, $\nabla \times \mathbf{E} \in \mathbf{L}^2(\Omega)$, and $\nabla \times \mathbf{H} \in \mathbf{L}^2(\Omega)$. Therefore, the vector functions $\mathbf{D}$, $\mathbf{B}$, $\mathbf{E}$, and $\mathbf{H}$ must be elements of the Sobolev space $\mathcal{H}(div, \Omega)$ and $\mathcal{H}(curl, \Omega)$, where Ω denotes the MM domain [*section 2.2.1*, [118]].

One can obtain the complete set of additional interface conditions between centrosymmetric metamaterials by defining the fields in the Sobolev space and applying the weak formulation of the wave equation, as elaborated in Section 2.4.1. These interface conditions are given by Eq. (3.15) and can be derived by incorporating the concepts presented in [113, 116, 144]. These works cover the necessary theory and the derivation process, up to a general expansion order of the response function.

Investigating the interface between chiral-achiral materials, we simply can add a chirality term on the left-hand side of the interface condition to account for the non-centrosymmetric nature of the structure. This term, expressed as $k_0^2\ \mathrm{i}\tilde{\kappa}(k_0)\mathbf{E}\times\mathbf{n}$, is crucial in deriving interface conditions for inversion-asymmetric metamaterials. The complete set of interface conditions for inversion-asymmetric structures can be obtained by following a similar methodology as for centrosymmetric structures and incorporating the extra term.

First Interface Condition

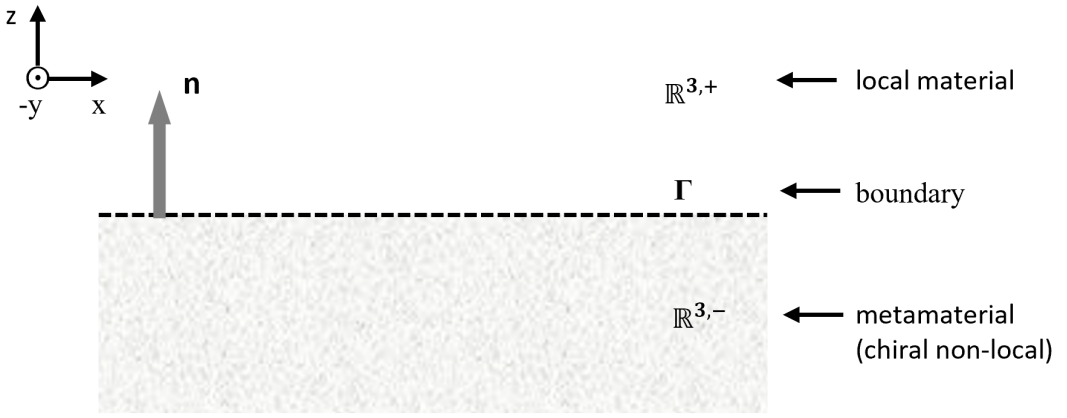

Figure C.3.: The figure depicts the region in which light propagates, where the upper half-space is filled with a homogeneous local medium and the lower half-space is filled with a chiral metamaterial (MM). The surface that separates the two half-spaces is represented by the symbol Γ. The normal vector $\mathbf{n}$ is directed outward from the homogenized metamaterial.

We can define the distribution action of the curl operator $(\nabla\times\mathbf{E})$ on a test function $\boldsymbol{\phi}$ in a weaker sense by incorporating $\boldsymbol{\phi}\in\mathcal{D}(\Omega)$ and $\mathbf{E}\in\mathcal{H}(curl,\Omega)$ for $\Omega\in\mathbb{R}^3$. This distribution action can be expressed as:

$$\int_{\mathbb{R}^3}(\nabla\times\mathbf{E})\cdot\boldsymbol{\phi}\ \mathrm{d}\mathbf{r}=\int_{\mathbb{R}^3}\mathbf{E}\cdot(\nabla\times\boldsymbol{\phi})\ \mathrm{d}\mathbf{r}. \tag{C.1}$$

Assuming two half-spaces, namely $\mathbb{R}^{3+}$ and $\mathbb{R}^{3-}$, depicted in Fig. C.3, where the upper half-space contains a homogeneous local medium described by constant material parameters $\varepsilon^{(\mathrm{loc})}$ and $\mu^{(\mathrm{loc})} = 1$, and the lower half-space contains a chiral nonlocal metamaterial (MM), the region of light propagation can be observed. The interface between these two half-spaces is denoted by the symbol Γ, with the normal vector $\mathbf{n}$ directed outward from the homogenized metamaterial.

When using the integration by parts on Eq. (C.1) in each half-space, we can separate the terms into a volume integral along the domain Ω and a surface integral along the boundary Γ.

$$\begin{aligned}\int_{\mathbb{R}^3} (\nabla \times \mathbf{E}) \cdot \boldsymbol{\phi} \, \mathrm{d}\mathbf{r} &= \int_{\mathbb{R}^{3+}} (\nabla \times \mathbf{E}) \cdot \boldsymbol{\phi} \, \mathrm{d}\mathbf{r} + \int_{\mathbb{R}^{3-}} (\nabla \times \mathbf{E}) \cdot \boldsymbol{\phi} \, \mathrm{d}\mathbf{r} \\ &= \int_{\mathbb{R}^{3+}} \varepsilon^{\mathrm{loc}} \mathbf{E} \cdot (\nabla \times \boldsymbol{\phi}) \, \mathrm{d}\mathbf{r} + \int_{\mathbb{R}^{3-}} \varepsilon(k_0) \mathbf{E} \cdot (\nabla \times \boldsymbol{\phi}) \, \mathrm{d}\mathbf{r} \\ &\quad + \int_{\Gamma} \Big(\mathbf{E}^{+} \times \mathbf{n} - \mathbf{E}^{-} \times \mathbf{n} \Big) \cdot \boldsymbol{\phi} \mathrm{d}\mathbf{s}, \end{aligned} \tag{C.2}$$

denoting the surface element on Γ as $\mathrm{d}\mathbf{s} = \mathrm{d}x\mathrm{d}y$, where $\Gamma = \partial\Omega$ is the boundary between the chiral MM and the surrounding medium, the electric field $\mathbf{E}$ satisfies certain smoothness conditions as discussed in [113]. Here, we use the notation $\mathbf{E}^{\pm} \coloneqq \mathbf{E} \,|_{\mathbb{R}^{\pm}}$ to represent the electric field in each half-space.

The first interface condition Eq. (c-IC 1) follows from Eq. (C.1) and Eq. (C.2) requiring the integral at the boundary to vanish. This argument remains true for any arbitrary choice of $\boldsymbol{\phi}$.

Additional Interface Condition

By assuming that the regularity condition

$$\Big\{ \mathbf{E},\ \nabla \times \mathbf{E},\ \nabla \times \nabla \times \mathbf{E},\ \mathbb{o}_{n,m} (\nabla \times)^{(2n-m)} \mathbf{E} \Big\} \ \in\ \mathbf{L}^2_{\mathrm{loc}}(\Omega), \tag{C.3}$$

holds and using the definition of the generalized derivative, we can write the weak form of the wave equation for a nonlocal chiral MM governed by the general constitutive relation,

$$\begin{aligned}\int_{\mathbb{R}^3} (\nabla \times \mathbf{E}) \cdot (\nabla \times \boldsymbol{\phi}) \mathrm{d}\mathbf{r} = k_0^2 \int_{\mathbb{R}^+} \varepsilon^{\mathrm{loc}} \mathbf{E} \cdot \boldsymbol{\phi} \mathrm{d}\mathbf{r} + k_0^2 \int_{\mathbb{R}^-} \tilde{\varepsilon} \mathbf{E} \cdot \boldsymbol{\phi} \mathrm{d}\mathbf{r} \\ + \int_{\mathbb{R}^-} k_0^2 (\mathrm{i}\ \tilde{\kappa}\ \mathbf{E}) \cdot (\nabla \times \boldsymbol{\phi}) \mathrm{d}\mathbf{r} \\ + \int_{\mathbb{R}^-} \sum_{n=1}^{N} \sum_{m=0}^{2n} \mathbb{o}_{n,m} (\nabla\times)^{(2n-m)} \mathbf{E} \cdot ((\nabla\times)^m \boldsymbol{\phi}) \mathrm{d}\mathbf{r}. \end{aligned} \tag{C.4}$$

For readability, the explicit arguments on the material parameters and electric field components are often omitted. However, it should be noted that all material parameters carry the argument (k_0), while the fields carry $(\mathbf{k}, k_0)$.

To establish the remaining interface condition, we can decompose the integral on the left-hand side of Eq. (C.4) into a sum of integrals over the half-spaces $\mathbb{R}^{3+}$ and $\mathbb{R}^{3-}$. By using integration by parts, as presented in Eq. (C.1), we can move all instances of $(\nabla\times)$ from the test function $\boldsymbol{\phi}$ to the electric field in each term of Eq. (C.4). This yields the following expression:

$$\begin{aligned}&\int_{\mathbb{R}^{3+}} \left(\nabla \times \nabla \times \mathbf{E} - k_0^2\ \varepsilon^{\mathrm{loc}} \mathbf{E}\right) \cdot\ \boldsymbol{\phi}\ \mathrm{d}\mathbf{r} \\ &\quad + \int_{\mathbb{R}^{3-}} \left(\nabla \times \nabla \times \mathbf{E} - k_0^2 \varepsilon \mathbf{E} + k_0^2\ \mathrm{i}\ \tilde{\kappa}\ \nabla \times \mathbf{E}\right) \cdot\ \boldsymbol{\phi}\ \mathrm{d}\mathbf{r} \\ &\quad\quad + \int_{\mathbb{R}^{3-}} \left(k_0^2 \sum_{n=1}^{N} \sum_{m=0}^{2n} (\nabla\times)^m \mathbb{o}_{n,m} (\nabla\times)^{(2n-m)} \mathbf{E}\right) \cdot\ \boldsymbol{\phi}\ \mathrm{d}\mathbf{r} \\ &= \int_{\Gamma} \left(\left(\nabla \times \mathbf{E}^- - \nabla \times \mathbf{E}^+\right) \times \mathbf{n}\right) \cdot\ \boldsymbol{\phi}\ \mathrm{d}\mathbf{s} + \int_{\Gamma} \left(\left(k_0^2\ \mathrm{i}\ \tilde{\kappa}\ \mathbf{E}^-\right) \times \mathbf{n}\right) \cdot \boldsymbol{\phi}\ \mathrm{d}\mathbf{s} \\ &\quad + k_0^2 \sum_{n=1}^{N} \sum_{m=1}^{2n} \sum_{k=0}^{m-1} \int_{\Gamma} \left(\left((\nabla\times)^k \mathbb{o}_{n,m} (\nabla\times)^{(2n-m)} \mathbf{E}^-\right) \times \mathbf{n}\right) \cdot \left((\nabla\times)^{(m-k-1)}\ \boldsymbol{\phi}\right) \mathrm{d}\mathbf{s}. \end{aligned} \tag{C.5}$$

Furthermore, due to the constitutive relation and the corresponding dispersion relation in the pertinent half-spaces, the left-hand side of Eq. (C.5) evaluates to zero. As a result, the right-hand side of the equation also evaluates to zero. We can reorganize the summation

order and write the equation in the following form:

$$\int_\Gamma \Big(\Big(\nabla \times \mathbf{E}^+ - \nabla \times \mathbf{E}^- + k_0^2 \ \mathrm{i} \ \tilde{\kappa} \ \mathbf{E}^- \Big) \times \mathbf{n} \Big) \cdot \boldsymbol{\phi} \ \mathrm{d}\mathbf{s}$$

$$+ \sum_{k=0}^{2N-1} \int_\Gamma \left(\mathcal{L}_k \mathbf{E}^- \times \mathbf{n} \right) \cdot \Big((\nabla \times)^k \boldsymbol{\phi} \Big) \mathrm{d}\mathbf{s} = 0. \tag{C.6}$$

where the $\mathcal{L}_k$ are defined by Eq. (3.15). Finally, we can conclude by writing down the general form of the interface condition for the chiral-achiral interface,

$$\Big(\mathbf{E}^+ - \mathbf{E}^- \Big) \times \mathbf{n} = 0,$$

$$\delta_{k,0} \Big(\nabla \times \mathbf{E}^+ - \nabla \times \mathbf{E}^- \Big) \times \mathbf{n} + \Big(k_0^2 \ \mathrm{i} \ \tilde{\kappa} \ \mathbf{E}^- \Big) \times \mathbf{n} + \mathbb{L}_k \mathbf{E}^- \times \mathbf{n} = 0. \tag{C.7}$$

for $k \in \{0, \ldots, 2N-1\}$. Setting $N = 2$ finally reveals the interface condition (c-IC 1) - (c-IC 3) for the SSD-γ model.

Notice that, setting the chirality parameter κ to zero immediately transforms the general interface conditions Eq. (C.7) to the interface condition Eq. (3.14) for an interface having a centrosymmetric material on either side.

C.2. Field Modelings

In a chiral medium, the polarization of eigenmodes can exhibit right or left-circular polarization, depending on the magnitude and handedness of the material's chirality. As a result, the electric and magnetic fields in the medium are coupled, and their orientations change as the wave propagates through it. Circularly polarized light features fixed angular velocity rotation of the electric and magnetic fields around the direction of propagation. The magnitude and direction of this rotation are influenced by the chirality of the material, which is quantified by the chirality parameter.

A forward propagating circularly polarized plane wave in the z-direction can be described mathematically as

$$\mathbf{E}(\mathbf{r}, t) = \frac{E_0}{\sqrt{2}} \begin{pmatrix} 1, & \pm \mathrm{i}, & 0 \end{pmatrix} \mathrm{e}^{\mathrm{i}(k_z z - k_0 t)} \tag{C.8}$$

where E_0 is the magnitude of the electric field, $\mathbf{k}$ is the wave vector, k_0 is the angular frequency, $\mathbf{r}$ is the position vector, and t is time. The $\pm\mathrm{i}$ term indicates the two possible

handednesses of circular polarization

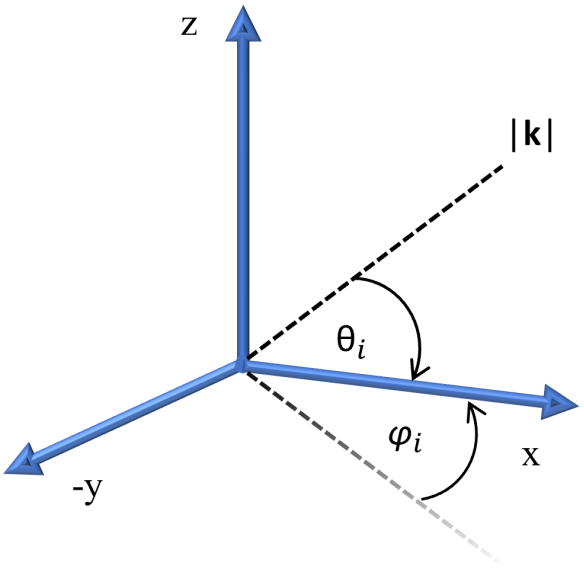

Figure C.4.: Spherical polar coordinate system, where the position of a point in space is described by the radial distance $|\mathbf{k}|$, the polar angle ϑ, and the azimuthal angle φ. The x, y, z axes are defined accordingly, with the origin at the center of the sphere.

To write the eigenmodes of circularly polarized plane wave in cartesian coordinates, one can first express the Cartesian coordinates in terms of the radial, azimuthal, and polar components,see Fig. C.4. Further, to connect these eigen modes with the incident field, we can modify the wave vector $\mathbf{k}$ to account for the angle of incidence θ_i and ϕ_i between the wave vector and the parallel coordinate to the incident plane. Therefore, the corresponding wave vector components

$$\begin{pmatrix} k_x \\ k_y \\ k_z \end{pmatrix} = k \begin{pmatrix} -\cos\theta_i \cos\phi_i \\ -\cos\theta_i \sin\phi_i \\ \sin\theta_i \end{pmatrix}, \tag{C.9}$$

where $k = |\mathbf{k}|$ is the magnitude of the wave vector along the $[\hat{\mathrm{r}}, \hat{\theta}, \hat{\phi},]$. In this setting, ϕ_i is the azimuthal angle of incidence (measured relative to some reference direction), and we have assumed that the interface is in the XZ plane.

Substituting this expression for $\mathbf{k}$ into the equation for $\mathbf{E}(\mathbf{r}, t)$, we obtain [*chapter 2, section 2.24*, [206]]:

$$\mathbf{E}(\mathbf{r},t) = \frac{E_0}{\sqrt{2}} \begin{pmatrix} \pm\cos\theta_i \cos\phi_i + i\sin\phi_i \\ \pm\cos\theta_i \sin\phi_i - i\cos\phi_i \\ \sin\theta_i \end{pmatrix} \mathrm{e}^{\mathrm{i}(k_x x + k_y y + k_z z - k_0 t)}. \tag{C.10}$$

This represents a forward propagating circularly polarized plane wave with oblique incidence, where the direction of polarization is determined by the angle of incidence and the handedness is determined by the sign of the phase difference between the two orthogonal components of $\mathbf{E}_0$. Note that the $\pm$ sign in the expression for the polarization components depends on the choice of handedness.

C.3. Fresnel Expressions: Calculating Reflection and Transmission Coefficients

To compute the transmission and reflection coefficients from the slab, interface conditions are necessary to establish the continuity of the fields at interfaces Γ_1 and Γ_2. The situation is sketched in figure Fig. C.5 Here, we denote the angle of incidence, and the corresponding angles made by the wave vectors inside the MM are henceforth given as

$$\theta_0 = \arcsin\left(k_x/k_0\right), \quad \theta_{\mathrm{RC}} = \arctan\left(k_x/\left|k_{z,i,\mathrm{RC}}\right|\right), \quad \theta_{\mathrm{LC}} = \arctan\left(k_x/\left|k_{z,i,\mathrm{LC}}\right|\right). \tag{C.11}$$

Assuming the surrounding medium in $\Omega^{\pm}$ are identical, then angle of transmittance, denoted by θ_t, is equal to the angle of incidence θ_0. The incident, transmitted, and reflected fields in a circular basis are given by omitting the complex phase.

$$\mathbf{E}_{\mathrm{RC}}^{\mathrm{inc/T}} = \frac{1}{\sqrt{2}} \begin{pmatrix} -\cos\theta_0 \\ -\mathrm{i} \\ \sin\theta_0 \end{pmatrix} E_{\mathrm{RC}}^{\mathrm{inc/T}}, \qquad \mathbf{E}_{\mathrm{LC}}^{\mathrm{inc/T}} = \frac{1}{\sqrt{2}} \begin{pmatrix} \cos\theta_0 \\ -\mathrm{i} \\ -\sin\theta_0 \end{pmatrix} E_{\mathrm{LC}}^{\mathrm{inc/T}}, \tag{C.12}$$

$$\mathbf{E}_{\mathrm{LC}}^{\mathrm{R}} = \frac{1}{\sqrt{2}} \begin{pmatrix} -\cos\theta_0 \\ -\mathrm{i} \\ -\sin\theta_0 \end{pmatrix} E_{\mathrm{LC}}^{\mathrm{R}}, \qquad \mathbf{E}_{\mathrm{RC}}^{\mathrm{R}} = \frac{1}{\sqrt{2}} \begin{pmatrix} \cos\theta_0 \\ -\mathrm{i} \\ \sin\theta_0 \end{pmatrix} E_{\mathrm{RC}}^{\mathrm{R}}. \tag{C.13}$$

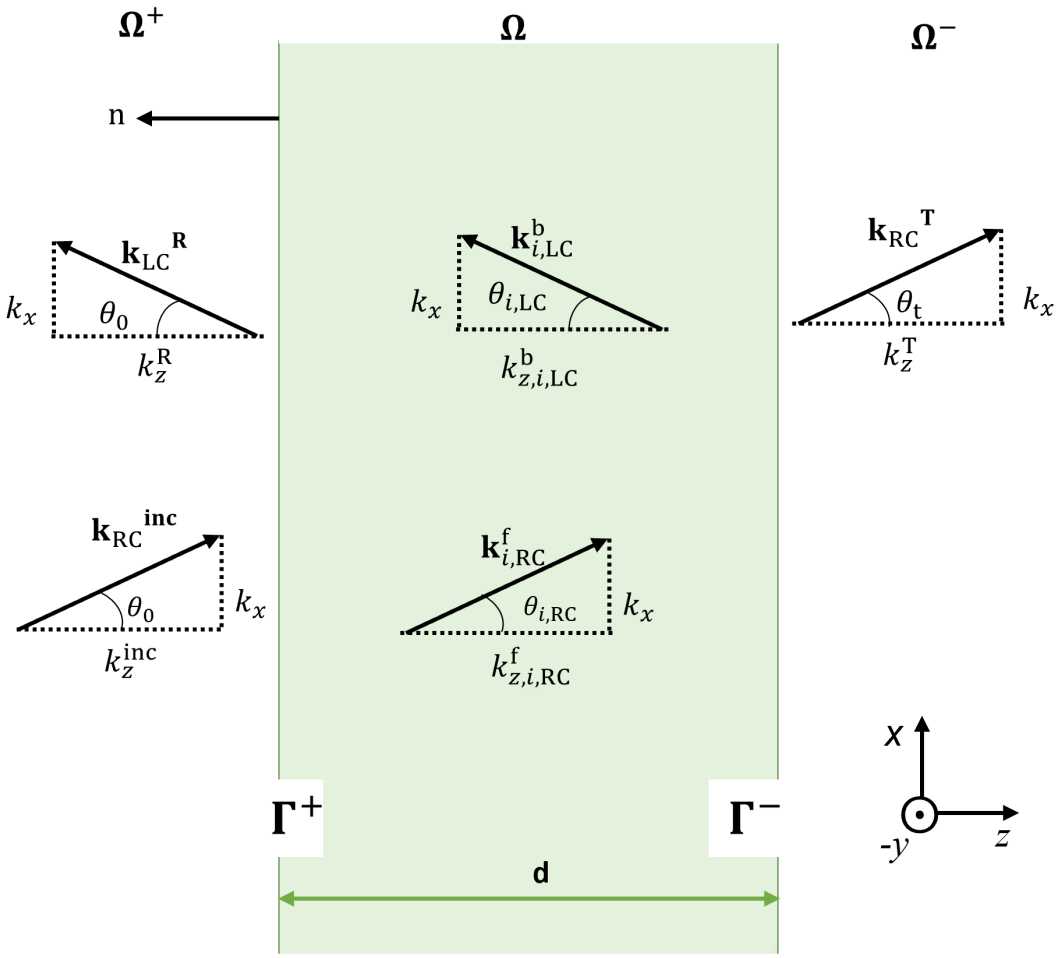

Figure C.5.: Sketch of a geometry where we consider a homogeneous nonlocal chiral slab of thickness 'd' with two interfaces labeled as Γ^+ and Γ^-. The incident wave is a right-handed circularly polairzed plane wave with a wave vector denoted as $\mathbf{k}_{\mathrm{RC}}^{\mathrm{inc}}$. The corresponding transmitted wave is denoted as $\mathbf{k}_{\mathrm{RC}}^{\mathrm{T}}$, and the reflected wave is given by the wave vector $\mathbf{k}_{\mathrm{LC}}^{\mathrm{R}}$. Inside the chiral homogeneous slab volume, there are expected to be $i = 2N$ roots of the wave vector component k_z corresponding to the N^{th} order polynomial dispersion relation. These roots correspond to both forward and backward propagating waves with the corresponding wave vectors denoted as $\mathbf{k}_{\mathrm{RC}}^{\mathrm{f}}$ and $\mathbf{k}_{\mathrm{LC}}^{\mathrm{b}}$, respectively.

As the reflected wave travels in the opposite direction, it maintains its sense of rotation with respect to the incident wave, causing a reversal of its handedness. This effect can also be seen by noting that the x- and y-components of both the incident field $\mathbf{E}_{\mathrm{RC}}^{\mathrm{inc}}$ and the reflected field $\mathbf{E}_{\mathrm{LC}}^{\mathrm{R}}$ are identical. The third component is determined by the first Maxwell equation, which mandates that the divergence of the displacement field is zero,

$$\nabla \cdot \mathbf{D} = 0 \quad \Longrightarrow \nabla \cdot \mathbf{RE} \Longrightarrow \quad \mathbf{k} \cdot \varepsilon \mathbf{E} = 0 \quad \overset{k_y=0}{\Longrightarrow} \quad E_z = -\frac{\varepsilon_x}{\varepsilon_z}\frac{k_x}{k_z}E_x. \tag{C.14}$$

For the sake of readability, the arguments for the fields and material parameters are omitted

in the following equations.

Similarly, the fields propagating in both directions inside the slab can be described by

$$\mathbf{E}^{\mathrm{f}}_{\mathrm{RC}} = \frac{1}{\sqrt{2}} \begin{pmatrix} -\cos\theta_{\mathrm{RC}} \\ -\mathrm{i} \\ \sin\theta_{\mathrm{RC}} \end{pmatrix} E^{\mathrm{f}}_{\mathrm{RC}}, \qquad \mathbf{E}^{\mathrm{f}}_{\mathrm{LC}} = \frac{1}{\sqrt{2}} \begin{pmatrix} \cos\theta_{\mathrm{LC}} \\ -\mathrm{i} \\ -\sin\theta_{\mathrm{LC}} \end{pmatrix} E^{\mathrm{f}}_{\mathrm{LC}}, \tag{C.15}$$

$$\mathbf{E}^{\mathrm{b}}_{\mathrm{RC}} = \frac{1}{\sqrt{2}} \begin{pmatrix} \cos\theta_{\mathrm{RC}} \\ -\mathrm{i} \\ \sin\theta_{\mathrm{RC}} \end{pmatrix} E^{\mathrm{b}}_{\mathrm{RC}}, \qquad \mathbf{E}^{\mathrm{b}}_{\mathrm{LC}} = \frac{1}{\sqrt{2}} \begin{pmatrix} -\cos\theta_{\mathrm{LC}} \\ -\mathrm{i} \\ -\sin\theta_{\mathrm{LC}} \end{pmatrix} E^{\mathrm{b}}_{\mathrm{LC}}. \tag{C.16}$$

Furthermore, we present the components of the IC Vectors(c-IC 1)-(c-IC 3) for a material that follows the SSD-γ model. The complete SSD Fresnel matrix is given in Eq. (C.22). The incident field is expressed as:

$$\begin{aligned} \underline{\mathbf{I}} = \big(&\cos\theta_0 \,(-E^{\mathrm{inc}}_{\mathrm{RC}} + E^{\mathrm{inc}}_{\mathrm{LC}}),\, 0,\, -E^{\mathrm{inc}}_{\mathrm{RC}} - E^{\mathrm{inc}}_{\mathrm{LC}},\, 0, \\ &g_{51}\,(-E^{\mathrm{inc}}_{\mathrm{RC}} + E^{\mathrm{inc}}_{\mathrm{LC}}),\, 0,\, \mu\, k_{0,z}\,(E^{\mathrm{inc}}_{\mathrm{RC}} + E^{\mathrm{inc}}_{\mathrm{LC}}),\, 0,\, 0,\, 0,\, 0,\, 0\big)^{\mathrm{T}}. \end{aligned} \tag{C.17}$$

and the electric field

$$\begin{aligned} \mathbf{E} = (&E^{\mathrm{R}}_{\mathrm{RC}},\, E^{\mathrm{R}}_{\mathrm{LC}},\, E^{\mathrm{f}}_{\mathrm{RC},1},\, E^{\mathrm{f}}_{\mathrm{RC},2},\, E^{\mathrm{f}}_{\mathrm{LC},3},\, E^{\mathrm{f}}_{\mathrm{LC},4}, \\ &E^{\mathrm{b}}_{\mathrm{RC},1},\, E^{\mathrm{b}}_{\mathrm{RC},2},\, E^{\mathrm{b}}_{\mathrm{LC},3},\, E^{\mathrm{b}}_{\mathrm{LC},4},\, E^{\mathrm{T}}_{\mathrm{RC}},\, E^{\mathrm{T}}_{\mathrm{LC}})^{\mathrm{T}}. \end{aligned} \tag{C.18}$$

relating the unknown fields $\underline{\mathbf{E}}$ and the input vector $\underline{\mathbf{I}}$ via the equation

$$\mathbf{F}^{\mathrm{SSD}} \cdot \underline{\mathbf{E}} = \underline{\mathbf{I}}, \tag{C.19}$$

Finally, the complex reflection and transmission amplitudes from the slab are calculable according to

$$\mathbf{R}^{\mathrm{SSD}-\gamma} = \left[\left(\mathbf{F}^{\mathrm{SSD}}\right)^{-1} \cdot \underline{\mathbf{I}} \right]_1 \tag{C.20}$$

$$\mathbf{T}^{\mathrm{SSD}-\gamma} = \left[\left(\mathbf{F}^{\mathrm{SSD}}\right)^{-1} \cdot \underline{\mathbf{I}} \right]_{12}. \tag{C.21}$$

$$
\mathbf{F}^{\mathrm{SSD}} = \begin{pmatrix}
-\cos\theta_0 & \cos\theta_0 & -\cos\theta_{\mathrm{RC},1} & -\cos\theta_{\mathrm{RC},2} \\
0 & 0 & -\cos\theta_{\mathrm{RC},1}\,\mathrm{e}^{\left(\mathrm{i}k^{\mathrm{f}}_{z,1,\mathrm{RC}}d\right)} & -\cos\theta_{\mathrm{RC},2}\,\mathrm{e}^{\left(\mathrm{i}k^{\mathrm{f}}_{z,1,\mathrm{RC}}d\right)} \\
1 & 1 & -1 & -1 \\
0 & 0 & -\mathrm{e}^{\left(\mathrm{i}k^{\mathrm{f}}_{z,1,\mathrm{RC}}d\right)} & -\mathrm{e}^{\left(\mathrm{i}k^{\mathrm{f}}_{z,2,\mathrm{RC}}d\right)} \\
g_{51} & -g_{51} & g_{53} & g_{54} \\
0 & 0 & g_{53}\,\mathrm{e}^{\left(\mathrm{i}k^{\mathrm{f}}_{z,1,\mathrm{RC}}d\right)} & g_{54}\,\mathrm{e}^{\left(\mathrm{i}k^{\mathrm{f}}_{z,2,\mathrm{RC}}d\right)} \\
\mu\,k_{0,z} & \mu\,k_{0,z} & g_{73} & g_{74} \\
0 & 0 & g_{73}\,\mathrm{e}^{\left(\mathrm{i}k^{\mathrm{f}}_{z,1,\mathrm{RC}}d\right)} & g_{74}\,\mathrm{e}^{\left(\mathrm{i}k^{\mathrm{f}}_{z,2,\mathrm{RC}}d\right)} \\
0 & 0 & g_{93} & g_{94} \\
0 & 0 & g_{93}\,\mathrm{e}^{\left(\mathrm{i}k^{\mathrm{f}}_{z,1,\mathrm{RC}}d\right)} & g_{94}\,\mathrm{e}^{\left(\mathrm{i}k^{\mathrm{f}}_{z,2,\mathrm{RC}}d\right)} \\
0 & 0 & (k_{\mathrm{RC},1})^2 & (k_{\mathrm{RC},2})^2 \\
0 & 0 & (k_{\mathrm{RC},2})^2\,\mathrm{e}^{\left(\mathrm{i}k^{\mathrm{f}}_{z,1,\mathrm{RC}}d\right)} & (k_{\mathrm{RC},2})^2\,\mathrm{e}^{\left(\mathrm{i}k^{\mathrm{f}}_{z,2,\mathrm{RC}}d\right)}
\end{pmatrix} \cdot \cdot
$$

$$
\begin{pmatrix}
\cos\theta_{\mathrm{LC},1} & \cos\theta_{\mathrm{LC},2} & \cos\theta_{\mathrm{RC},1} & \cos\theta_{\mathrm{RC},2} \\
\cos\theta_{\mathrm{LC},1}\,\mathrm{e}^{\left(\mathrm{i}k^{\mathrm{f}}_{z,1,\mathrm{LC}}d\right)} & \cos\theta_{\mathrm{LC},2}\,\mathrm{e}^{\left(\mathrm{i}k^{\mathrm{f}}_{z,2,\mathrm{LC}}d\right)} & \cos\theta_{\mathrm{RC},1}\,\mathrm{e}^{\left(\mathrm{i}k^{\mathrm{f}}_{z,1,\mathrm{RC}}d\right)} & \cos\theta_{\mathrm{RC},2}\,\mathrm{e}^{\left(\mathrm{i}k^{\mathrm{f}}_{z,1,\mathrm{RC}}d\right)} \\
-1 & -1 & -1 & -1 \\
-\mathrm{e}^{\left(\mathrm{i}k^{\mathrm{f}}_{z,1,\mathrm{LC}}d\right)} & -\mathrm{e}^{\left(\mathrm{i}k^{\mathrm{f}}_{z,2,\mathrm{LC}}d\right)} & -\mathrm{e}^{\left(\mathrm{i}k^{\mathrm{f}}_{z,1,\mathrm{RC}}d\right)} & -\mathrm{e}^{\left(\mathrm{i}k^{\mathrm{f}}_{z,2,\mathrm{RC}}d\right)} \\
g_{55} & g_{56} & g_{53} & g_{54} \\
g_{55}\,\mathrm{e}^{\left(\mathrm{i}k^{\mathrm{f}}_{z,1,\mathrm{LC}}d\right)} & g_{56}\,\mathrm{e}^{\left(\mathrm{i}k^{\mathrm{f}}_{z,2,\mathrm{LC}}d\right)} & g_{53}\,\mathrm{e}^{\left(\mathrm{i}k^{\mathrm{f}}_{z,1,\mathrm{RC}}d\right)} & g_{54}\,\mathrm{e}^{\left(\mathrm{i}k^{\mathrm{f}}_{z,2,\mathrm{RC}}d\right)} \\
g_{75} & g_{76} & -g_{73} & -g_{74} \\
g_{75}\,\mathrm{e}^{\left(\mathrm{i}k^{\mathrm{f}}_{z,1,\mathrm{LC}}d\right)} & g_{76}\,\mathrm{e}^{\left(\mathrm{i}k^{\mathrm{f}}_{z,2,\mathrm{LC}}d\right)} & -g_{73}\,\mathrm{e}^{\left(\mathrm{i}k^{\mathrm{f}}_{z,1,\mathrm{RC}}d\right)} & -g_{74}\,\mathrm{e}^{\left(\mathrm{i}k^{\mathrm{f}}_{z,2,\mathrm{RC}}d\right)} \\
g_{95} & g_{96} & -g_{93} & -g_{94} \\
g_{95}\,\mathrm{e}^{\left(\mathrm{i}k^{\mathrm{f}}_{z,1,\mathrm{LC}}d\right)} & g_{96}\,\mathrm{e}^{\left(\mathrm{i}k^{\mathrm{f}}_{z,2,\mathrm{LC}}d\right)} & -g_{93}\,\mathrm{e}^{\left(\mathrm{i}k^{\mathrm{f}}_{z,1,\mathrm{RC}}d\right)} & -g_{94}\,\mathrm{e}^{\left(\mathrm{i}k^{\mathrm{f}}_{z,2,\mathrm{RC}}d\right)} \\
(k_{\mathrm{LC},1})^2 & (k_{\mathrm{LC},2})^2 & (k_{\mathrm{RC},1})^2 & (k_{\mathrm{RC},2})^2 \\
(k_{\mathrm{LC},1})^2\,\mathrm{e}^{\left(\mathrm{i}k^{\mathrm{f}}_{z,1,\mathrm{LC}}d\right)} & (k_{\mathrm{LC},2})^2\,\mathrm{e}^{\left(\mathrm{i}k^{\mathrm{f}}_{z,2,\mathrm{LC}}d\right)} & (k_{\mathrm{RC},2})^2\,\mathrm{e}^{\left(\mathrm{i}k^{\mathrm{f}}_{z,1,\mathrm{RC}}d\right)} & (k_{\mathrm{RC},2})^2\,\mathrm{e}^{\left(\mathrm{i}k^{\mathrm{f}}_{z,2,\mathrm{RC}}d\right)}
\end{pmatrix}
$$

$$
\cdot \cdot \begin{pmatrix}
-\cos\theta_{\mathrm{LC},1} & -\cos\theta_{\mathrm{LC},2} & 0 & 0 \\
-\cos\theta_{\mathrm{LC},1}\,\mathrm{e}^{\left(\mathrm{i}k^{\mathrm{f}}_{z,1,\mathrm{LC}}d\right)} & -\cos\theta_{\mathrm{LC},1}\,\mathrm{e}^{\left(\mathrm{i}k^{\mathrm{f}}_{z,2,\mathrm{LC}}d\right)} & \cos\theta_0 & -\cos\theta_0 \\
-1 & -1 & 0 & 0 \\
-\mathrm{e}^{\left(\mathrm{i}k^{\mathrm{f}}_{z,1,\mathrm{LC}}d\right)} & -\mathrm{e}^{\left(\mathrm{i}k^{\mathrm{f}}_{z,2,\mathrm{LC}}d\right)} & 1 & 1 \\
g_{55} & g_{56} & 0 & 0 \\
g_{55}\,\mathrm{e}^{\left(\mathrm{i}k^{\mathrm{f}}_{z,1,\mathrm{LC}}d\right)} & g_{56}\,\mathrm{e}^{\left(\mathrm{i}k^{\mathrm{f}}_{z,2,\mathrm{LC}}d\right)} & g_{51} & -g_{51} \\
-g_{75} & -g_{76} & 0 & 0 \\
-g_{75}\,\mathrm{e}^{\left(\mathrm{i}k^{\mathrm{f}}_{z,a,\mathrm{LC}}d\right)} & -g_{76}\,\mathrm{e}^{\left(\mathrm{i}k^{\mathrm{f}}_{z,2,\mathrm{LC}}d\right)} & -\mu(k_0)\,k_{0,z} & -\mu(k_0)\,k_{0,z} \\
-g_{95} & -g_{96} & 0 & 0 \\
-g_{95}\,\mathrm{e}^{\left(\mathrm{i}k^{\mathrm{f}}_{z,1,\mathrm{LC}}d\right)} & -g_{96}\,\mathrm{e}^{\left(\mathrm{i}k^{\mathrm{f}}_{z,2,\mathrm{LC}}d\right)} & 0 & 0 \\
(k^{\mathrm{LC},1})^2 & (k^{\mathrm{LC},2})^2 & 0 & 0 \\
(k^{\mathrm{LC},1})^2\,\mathrm{e}^{\left(\mathrm{i}k^{\mathrm{f}}_{z,1,\mathrm{LC}}d\right)} & (k^{\mathrm{LC},2})^2\,\mathrm{e}^{\left(\mathrm{i}k^{\mathrm{f}}_{z,2,\mathrm{LC}}d\right)} & 0 & 0
\end{pmatrix} . \quad \text{(C.22)}
$$

with the corresponding terms,

$$
\begin{aligned}
g_{51} &= \frac{\mu(k_0)\, k_0^2\, \cos\theta_0}{k_{0,z}} \\
g_{53} &= 2\tilde{\kappa}(k_0)\, k_0 - \frac{(k_{\mathrm{RC},1})^2 \left(1 - k_0^2\, \mu(k_0)\gamma(k_0)\, (k_{\mathrm{RC},1})^2\right) \cos\theta_{\mathrm{RC},1}}{k^{\mathrm{RC}}_{\mathrm{f},z,2}}, \\
g_{54} &= 2\tilde{\kappa}(k_0)\, k_0 - \frac{(k_{\mathrm{RC},2})^2 \left(1 - k_0^2\, \mu(k_0)\gamma(k_0)\, (k_{\mathrm{RC},2})^2\right) \cos\theta_{\mathrm{RC},2}}{k^{\mathrm{RC}}_{\mathrm{f},z,2}}, \\
g_{55} &= 2\tilde{\kappa}(k_0)\, k_0 + \frac{(k^{\mathrm{LC},1})^2 \left(1 - k_0^2\, \mu(k_0)\gamma(k_0)\, (k_{\mathrm{LC},1})^2\right) \cos\theta_{\mathrm{LC},1}}{k^{\mathrm{LC}}_{\mathrm{f},z,1}}, \\
g_{56} &= 2\tilde{\kappa}(k_0)\, k_0 + \frac{(k_{\mathrm{LC},2})^2 \left(1 - k_0^2\, \mu(k_0)\gamma(k_0)\, (k^{\mathrm{LC},2})^2\right) \cos\theta_{\mathrm{LC},2}}{k^{\mathrm{LC}}_{\mathrm{f},z,2}},
\end{aligned}
$$

$$
\begin{aligned}
g_{73} &= -2\tilde{\kappa}(k_0)\, k_0\, \cos\theta_{\mathrm{RC},1} + k^{\mathrm{f}}_{,z,1,\mathrm{RC}} \left(1 - k_0^2\, \mu(k_0)\gamma(k_0)\, (k_{\mathrm{RC},1})^2\right), \\
g_{74} &= -2\tilde{\kappa}(k_0)\, k_0\, \cos\theta_{\mathrm{RC},2} + k^{\mathrm{f}}_{,z,2,\mathrm{RC}} \left(1 - k_0^2\, \mu(k_0)\gamma(k_0)\, (k_{\mathrm{RC},2})^2\right), \\
g_{75} &= 2\tilde{\kappa}(k_0)\, k_0\, \cos\theta_{\mathrm{LC},1} + k^{\mathrm{f}}_{,z,1,\mathrm{LC}} \left(1 - k_0^2\, \mu(k_0)\gamma(k_0)\, (k_{\mathrm{LC},1})^2\right), \\
g_{75} &= 2\tilde{\kappa}(k_0)\, k_0\, \cos\theta_{\mathrm{LC},2} + k^{\mathrm{f}}_{,z,2,\mathrm{LC}} \left(1 - k_0^2\, \mu(k_0)\gamma(k_0)\, (k_{\mathrm{LC},2})^2\right),
\end{aligned}
$$

$$
\begin{aligned}
g_{93} &= -(k_{\mathrm{RC},1})^2\, \cos\theta_{\mathrm{RC},1}, \\
g_{94} &= -(k_{\mathrm{RC},2})^2\, \cos\theta_{\mathrm{RC},2}, \\
g_{95} &= (k_{\mathrm{LC},1})^2\, \cos\theta_{\mathrm{LC},1}, \\
g_{96} &= (k_{\mathrm{LC},2})^2\, \cos\theta_{\mathrm{LC},2}.
\end{aligned}
$$

D. Deriving Effective Material Parameters from $\mathbf{T}_{\text{eff}}$-matrix

In this section of the appendix, we show the derivation for extracting the effective material parameters from a $\mathbf{T}_{\text{eff}}$-matrix for a given MM. For this, we consider a periodic lattice surrounded by a homogeneous host medium with permittivity ε_{h} and permeability μ_{h}. As before, we set the natural constants ε_0 and μ_0 as unity, making the frequency $\omega = k_0$.

Please note, throughout the derivation, we assume a plane wave ansatz for the fields. Also, we presume that all quantities, except for purely geometric factors, depend on frequency k_0.

To start our derivation, we calculate the induce effective electric $\mathbf{P}_{\text{eff,e}}$ and magnetic polarizations $\mathbf{P}_{\text{eff,m}}$ in a scatterer located at the center of the 3D lattice caused by all other fields present in the medium. We obtain the effective polarizations of the scatterer by using the effective T-matrix ($\mathbf{T}_{\text{eff}}$) of the lattice. the relation can be written as

By focusing solely on the dipolar component of $\mathbf{T}_{\text{eff}}$ $\mathbf{T}_{\text{eff}}^{\text{dip}}$, we can express the polarizations as follows:

$$\begin{pmatrix} \mathbf{P}_{\text{eff,e}} \\ \mathbf{P}_{\text{eff,m}} \end{pmatrix} = nq \begin{pmatrix} \mathbf{T}_{\text{eff,EE,cart}}^{j,j'=1,1} & \mathrm{i}Z_{\text{h}}\mathbf{T}_{\text{eff,EM,cart}}^{j,j'=1,1} \\ -\mathrm{i}Z_{\text{h}}\mathbf{T}_{\text{eff,ME,cart}}^{j,j'=1,1} & Z_{\text{h}}^2\mathbf{T}_{\text{eff,MM,cart}}^{j,j'=1,1} \end{pmatrix} \begin{pmatrix} \mathbf{E}_{\text{ext}} \\ \mathbf{H}_{\text{ext}} \end{pmatrix}, \tag{D.1}$$

where Externally applied electric $\mathbf{E}_{\text{ext}}$ and magnetic $\mathbf{H}_{\text{ext}}$ fields in a scatterer in the lattice, n is the concentration of the scatterers per unit cell, $Z_{\text{h}} = \sqrt{\mu_0/\varepsilon_{\text{h}}} = 1$ the wave impedance of the host medium, $q = \frac{-\mathrm{i}6\pi}{c_{\text{h}} Z_{\text{h}} k_{\text{h}}^3}$ [207], $c_{\text{h}} = 1/\sqrt{\varepsilon_{\text{h}}\mu_0} = 1$ is the speed of light in the host medium, and k_{h} the wave number in the host medium. The $\mathbf{T}_{\text{eff},\nu\nu',\text{cart}}^{j,j'=1,1}$ are block matrices building $\mathbf{T}_{\text{eff}}^{\text{dip}}$ in the Cartesian basis:

$$\mathbf{T}_{\text{eff}}^{\text{dip}} \equiv \begin{pmatrix} \mathbf{T}_{\text{eff,EE,cart}}^{j,j'=1,1} & \mathbf{T}_{\text{eff,EM,cart}}^{j,j'=1,1} \\ \mathbf{T}_{\text{eff,ME,cart}}^{j,j'=1,1} & \mathbf{T}_{\text{eff,MM,cart}}^{j,j'=1,1} \end{pmatrix}. \tag{D.2}$$

In the frequency domain, the Condon-Tellegen constitutive relation can be used to relate the electric displacement $\mathbf{D}$ and magnetic flux density $\mathbf{B}$ to the fields inside a material consisting of the lattice read

$$\begin{pmatrix} \mathbf{D} \\ \mathbf{B} \end{pmatrix} = \begin{pmatrix} \boldsymbol{\varepsilon}_{\text{eff}} & \mathrm{i}\boldsymbol{\kappa}_{\text{eff}} \\ -\mathrm{i}\boldsymbol{\kappa}_{\text{eff}} & \boldsymbol{\mu}_{\text{eff}} \end{pmatrix} \begin{pmatrix} \mathbf{E} \\ \mathbf{H} \end{pmatrix}. \tag{D.3}$$

Here the $\boldsymbol{\varepsilon}_{\text{eff}}$ is the effective tensorial permittivity, $\boldsymbol{\mu}_{\text{eff}}$ the permeability, and $\boldsymbol{\kappa}_{\text{eff}}$ is the chirality parameter. Notice that, here the fields $\mathbf{E}$ and $\mathbf{B}$ are the internal fields in a unit volume of the homogenized MM.

In order to relate this field to the internal fields of the actual MM (in-homogeneous medium), we must take care of the depolarization field, that arises due to the induced polarization. However, the depolarization tensor in Equation (D.6) accounts for the depolarization of a unit cell by external fields and doesn't include the interaction between scatterers within the lattice. The interactions between scatterers modify the dipolar terms in $\mathbf{T}_{\text{eff}}^{\text{dip}}$ and, therefore, the effective material parameters.

Borrowing the expression for the depolarization factor for a cuboid, $\mathbf{L} = (1/3)\mathbf{I}_3$ found in [208, 209] we can write the internal fields as

$$\begin{pmatrix} \mathbf{E} \\ \mathbf{H} \end{pmatrix} = \begin{pmatrix} \mathbf{E}_{\text{ext}} \\ \mathbf{H}_{\text{ext}} \end{pmatrix} - \begin{pmatrix} \frac{1}{\varepsilon_{\text{h}}}\mathbf{L} & 0 \\ 0 & \frac{1}{\mu_0}\mathbf{L} \end{pmatrix} \begin{pmatrix} \mathbf{P}_{\text{eff,e}} \\ \mathbf{P}_{\text{eff,m}} \end{pmatrix}, \tag{D.4}$$

where $\mathbf{T}_{\text{eff}}^{\text{dip}}$ and the polarizations are considered at the origin of the lattice.

Alternatively, we know that, the electric displacement$\mathbf{D}$ and the magnetic flux $\mathbf{B}$ can be written in terms of the polarization $\mathbf{P}_{\text{eff,e}}$ and $\mathbf{P}_{\text{eff,m}}$ [115] as

$$\begin{pmatrix} \mathbf{D} \\ \mathbf{B} \end{pmatrix} = \begin{pmatrix} \varepsilon_{\text{h}}\mathbf{I}_3 & 0 \\ 0 & \mu_0\mathbf{I}_3 \end{pmatrix} \begin{pmatrix} \mathbf{E} \\ \mathbf{H} \end{pmatrix} + \begin{pmatrix} \mathbf{P}_{\text{eff,e}} \\ \mathbf{P}_{\text{eff,m}} \end{pmatrix}. \tag{D.5}$$

Finally, using Eq. (D.1),Eq. (D.4) in Eq. (D.5)) we obtain an expression of ($\mathbf{D}$,$\mathbf{B}$) as a function of $\mathbf{T}_{\text{eff}}^{\text{dip}}$.

Comparison of the result with Equation (D.3) gives the material parameters

$$\begin{aligned} \begin{pmatrix} \boldsymbol{\varepsilon}_{\text{eff}} & \mathrm{i}\boldsymbol{\kappa}_{\text{eff}} \\ -\mathrm{i}\boldsymbol{\kappa}_{\text{eff}} & \boldsymbol{\mu}_{\text{eff}} \end{pmatrix} = & \begin{pmatrix} \varepsilon_{\text{h}}\mathbf{I}_3 & 0 \\ 0 & \mu_0\mathbf{I}_3 \end{pmatrix} + \\ & + n \left(\mathbf{I}_6 - n \cdot q \begin{pmatrix} \frac{1}{\varepsilon_{\text{h}}}\mathbf{T}_{\text{eff,EE,cart}}^{j,j'=1,1}\mathbf{L} & \mathrm{i}c_{\text{h}}\mathbf{T}_{\text{eff,EM,cart}}^{j,j'=1,1}\mathbf{L} \\ -\mathrm{i}\frac{Z_{\text{h}}}{\varepsilon_{\text{h}}}\mathbf{T}_{\text{eff,ME,cart}}^{j,j'=1,1}\mathbf{L} & c_{\text{h}}Z_{\text{h}}\mathbf{T}_{\text{eff,MM,cart}}^{j,j'=1,1}\mathbf{L} \end{pmatrix} \right)^{-1} \\ & \times q \begin{pmatrix} \mathbf{T}_{\text{eff,EE,cart}}^{j,j'=1,1} & \mathrm{i}Z_{\text{h}}\mathbf{T}_{\text{eff,EM,cart}}^{j,j'=1,1} \\ -\mathrm{i}Z_{\text{h}}\mathbf{T}_{\text{eff,ME,cart}}^{j,j'=1,1} & Z_{\text{h}}^2\mathbf{T}_{\text{eff,MM,cart}}^{j,j'=1,1} \end{pmatrix}. \end{aligned} \tag{D.6}$$

E. Analysis on the Impact of the Number of Multipoles N on the Accuracy of $\mathbf{T}_{\text{eff}}$

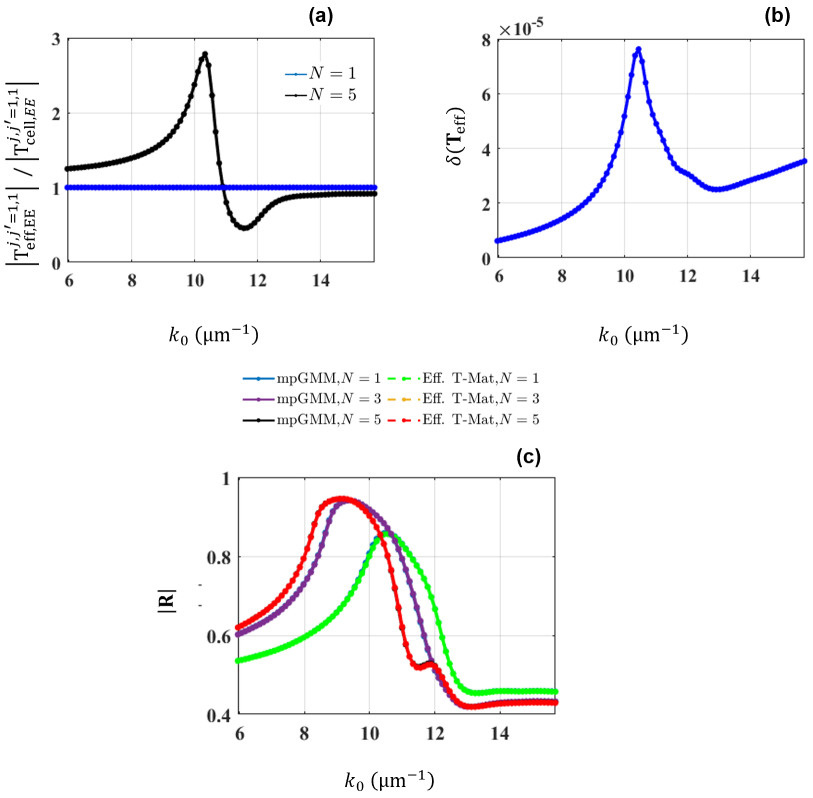

Figure E.6.: (a) The electric dipolar entry of the effective T-matrix of a 3D lattice of gold spheres is compared to the T-matrix of a single isolated sphere for calculations that include only dipoles $N = 1$, or up to $N = 5$ multipoles. The ratio between these quantities is presented. (b) The dipolar entry of the effective T-matrix is strongly modified by the interaction with higher order multipoles inside the lattice. However, the direct contribution of higher multipoles to the effective T-matrix is negligible. This implies that the effective dipolar entries alone can be safely used to describe the homogeneous medium. (c) The reflection coefficient of a slab of gold spheres is presented. The predicted response of the slab is significantly modified when higher-order multipoles are included in the calculations.

The gold example discussed in Section 4.3.1 involves placing gold spheres with a radius of 1 nm in a cubic lattice with a lattice constant of 2.05 nm and a medium with a relative permittivity of 2.25. The effective T-matrix is calculated up to the $N = 5$ multipolar order„as shown in Figure Fig. E.6**(a)**. We notice a large influence of the higher-order multipoles on the dipolar entry of the T-matrix.

Figure E.6**(b)** shows the plot of $\delta(\mathbf{T}_{\text{eff}})$ as defined in Eq. (4.14), which determines the significance of the non-dipolar components of the $\mathbf{T}_{\text{eff}}$-matrix on the optical response. Based on this figure, we can conclude that the direct contribution of higher-order multipoles to the

final effective T-matrix is negligible, and thus, the higher-order terms can be disregarded for the homogenization process.

In Fig. E.6**(c)**, the results obtained from the $\mathbf{T}_{\text{eff}}$ method are compared to the results from a full wave simulation (mpGMM). The comparison shows that the results obtained from both methods agree well. Additionally, the inclusion of higher multipolar orders is crucial, as they introduce a shift towards smaller frequencies, which is not observed when restricting to $N = 1$ as seen in Fig. E.6**(c)**.

We also noticed that, including multipoles higher than $N = 5$ leads to higher numerical errors, so the number of included multipoles is limited to $N = 5$.

Bibliography

[1] Victor G Veselago. Electrodynamics of substances with simultaneously negative electrical and magnetic permeabilities. *Soviet Physics Uspekhi*, 10(4):504–509, 1968.

[2] E. Shamonina and L. Solymar. Metamaterials: How the subject started. *Metamaterials*, 1(1):12–18, 2007.

[3] David R Smith, Willie J Padilla, DC Vier, Syrus C Nemat-Nasser, and Seldon Schultz. Composite medium with simultaneously negative permeability and permittivity. *Physical review letters*, 84(18):4184, 2000.

[4] M Kafesaki, I Tsiapa, N Katsarakis, Th Koschny, CM Soukoulis, and EN Economou. Left-handed metamaterials: The fishnet structure and its variations. *Physical Review B*, 75(23):235114, 2007.

[5] John B Pendry, Anthony J Holden, David J Robbins, and WJ Stewart. Magnetism from conductors and enhanced nonlinear phenomena. *IEEE transactions on microwave theory and techniques*, 47(11):2075–2084, 1999.

[6] Muamer Kadic, Tiemo Bückmann, Robert Schittny, and Martin Wegener. Metamaterials beyond electromagnetism. *Reports on Progress in physics*, 76(12):126501, 2013.

[7] Jung-Hwan Song, Jorik van de Groep, Soo Jin Kim, and Mark L Brongersma. Non-local metasurfaces for spectrally decoupled wavefront manipulation and eye tracking. *Nature Nanotechnology*, 16(11):1224–1230, 2021.

[8] Chihhui Wu, Burton Neuner III, Jeremy John, Andrew Milder, Byron Zollars, Steve Savoy, and Gennady Shvets. Metamaterial-based integrated plasmonic absorber/emitter for solar thermo-photovoltaic systems. *Journal of Optics*, 14(2):024005, 2012.

[9] Andrei Andryieuski and Andrei V Lavrinenko. Graphene metamaterials based tunable terahertz absorber: effective surface conductivity approach. *Optics express*, 21(7):9144–9155, 2013.

[10] D Yu Shchegolkov, AK Azad, JF O'hara, and EI Simakov. Perfect subwavelength fishnetlike metamaterial-based film terahertz absorbers. *Physical review B*, 82(20):205117, 2010.

[11] Cristian Della Giovampaola and Nader Engheta. Digital metamaterials. *Nature materials*, 13(12):1115–1121, 2014.

[12] Tie Jun Cui, Mei Qing Qi, Xiang Wan, Jie Zhao, and Qiang Cheng. Coding metamaterials, digital metamaterials and programmable metamaterials. *Light: science & applications*, 3(10):e218–e218, 2014.

[13] Ari Sihvola. Electromagnetic emergence in metamaterials. In *Advances in electromagnetics of complex media and metamaterials*, pages 3–17. Springer, 2002.

[14] M Lapine and S Tretyakov. Contemporary notes on metamaterials. *IET microwaves, antennas & propagation*, 1(1):3–11, 2007.

[15] Sergei A Tretyakov. A personal view on the origins and developments of the metamaterial concept. *Journal of Optics*, 19(1):013002, 2016.

[16] Carsten Rockstuhl and Toralf Scharf. *Amorphous nanophotonics*. Nano-Optics and Nanophotonics. Springer Science & Business Media, 1 edition, 2013.

[17] John Brian Pendry. Negative refraction makes a perfect lens. *Physical review letters*, 85(18):3966, 2000.

[18] Kan Yao and Yongmin Liu. Plasmonic metamaterials. *Nanotechnology Reviews*, 3(2):177–210, 2014.

[19] N I Landy, S Sajuyigbe, Jack J Mock, David R Smith, and Willie J Padilla. Perfect metamaterial absorber. *Physical review letters*, 100(20):207402, 2008.

[20] Na Liu, Martin Mesch, Thomas Weiss, Mario Hentschel, and Harald Giessen. Infrared perfect absorber and its application as plasmonic sensor. *Nano letters*, 10(7):2342–2348, 2010.

[21] Rasoul Alaee, Mohammad Albooyeh, and Carsten Rockstuhl. Theory of metasurface based perfect absorbers. *Journal of Physics D: Applied Physics*, 50(50):503002, 2017.

[22] Nader Engheta. Thin absorbing screens using metamaterial surfaces. In *IEEE Antennas and Propagation Society International Symposium (IEEE Cat. No. 02CH37313)*, volume 2, pages 392–395. IEEE, 2002.

[23] Rasoul Alaee, Christoph Menzel, Carsten Rockstuhl, and Falk Lederer. Perfect absorbers on curved surfaces and their potential applications. *Optics express*, 20(16):18370–18376, 2012.

[24] Mohammad Albooyeh, Dmitry Morits, and SA Tretyakov. Effective electric and magnetic properties of metasurfaces in transition from crystalline to amorphous state. *Physical Review B*, 85(20):205110, 2012.

[25] Koray Aydin, Vivian E Ferry, Ryan M Briggs, and Harry A Atwater. Broadband polarization-independent resonant light absorption using ultrathin plasmonic super absorbers. *Nature communications*, 2(1):517, 2011.

[26] Yicheng Wang, Kunlin Chen, Yu-Sheng Lin, and Bo-Ru Yang. Plasmonic metasurface with quadrilateral truncated cones for visible perfect absorber. *Physica E: Low-dimensional Systems and Nanostructures*, 139:115140, 2022.

[27] Patrick Rufangura and Cumali Sabah. Dual-band perfect metamaterial absorber for solar cell applications. *Vacuum*, 120:68–74, 2015.

[28] Aimi Abass, Khai Q Le, Andrea Alu, Marc Burgelman, and Bjorn Maes. Dual-interface gratings for broadband absorption enhancement in thin-film solar cells. *Physical Review B*, 85(11):115449, 2012.

[29] Shobhit K Patel, Juveriya Parmar, and Vijay Katkar. Ultra-broadband, wide-angle plus-shape slotted metamaterial solar absorber design with absorption forecasting using machine learning. *Scientific Reports*, 12(1):10166, 2022.

[30] Niels Gieseler, Aso Rahimzadegan, and Carsten Rockstuhl. Self-stabilizing curved metasurfaces as a sail for light-propelled spacecrafts. *Optics Express*, 29(14):21562–21575, 2021.

[31] Adam C Overvig, Sajan Shrestha, Stephanie C Malek, Ming Lu, Aaron Stein, Changxi Zheng, and Nanfang Yu. Dielectric metasurfaces for complete and independent control of the optical amplitude and phase. *Light: Science & Applications*, 8(1):1–12, 2019.

[32] Stéphane Larouche, Yu-Ju Tsai, Talmage Tyler, Nan M Jokerst, and David R Smith. Infrared metamaterial phase holograms. *Nature materials*, 11(5):450–454, 2012.

[33] Zi-Lan Deng, Mingke Jin, Xuan Ye, Shuai Wang, Tan Shi, Junhong Deng, Ningbin Mao, Yaoyu Cao, Bai-Ou Guan, Andrea Alù, et al. Full-color complex-amplitude vectorial holograms based on multi-freedom metasurfaces. *Advanced Functional Materials*, 30(21):1910610, 2020.

[34] Ke Chen, Yijun Feng, Francesco Monticone, Junming Zhao, Bo Zhu, Tian Jiang, Lei Zhang, Yongjune Kim, Xumin Ding, Shuang Zhang, et al. A reconfigurable active huygens' metalens. *Advanced materials*, 29(17):1606422, 2017.

[35] Andrea Alu, Mário G Silveirinha, Alessandro Salandrino, and Nader Engheta. Epsilon-near-zero metamaterials and electromagnetic sources: Tailoring the radiation phase pattern. *Physical review B*, 75(15):155410, 2007.

[36] Aso Rahimzadegan, Dennis Arslan, David Dams, Achim Groner, Xavi Garcia-Santiago, Rasoul Alaee, Ivan Fernandez-Corbaton, Thomas Pertsch, Isabelle Staude, and Carsten Rockstuhl. Beyond dipolar huygens' metasurfaces for full-phase coverage and unity transmittance. *Nanophotonics*, 9(1):75–82, 2020.

[37] Siyuan Shen, Zhaohui Ruan, Suning Li, Yuan Yuan, and Heping Tan. The influence of periodicity on the optical response of cube silicon metasurfaces. *Results in Physics*, 23:104057, 2021.

[38] Th Koschny, P Markoš, Eleftherios N Economou, DR Smith, DC Vier, and CM Soukoulis. Impact of inherent periodic structure on effective medium description of left-handed and related metamaterials. *Physical Review B*, 71(24):245105, 2005.

[39] Christoph Menzel, Carsten Rockstuhl, and Falk Lederer. Advanced jones calculus for the classification of periodic metamaterials. *Physical Review A*, 82(5):053811, 2010.

[40] Muamer Kadic, Graeme W Milton, Martin van Hecke, and Martin Wegener. 3d metamaterials. *Nature Reviews Physics*, 1(3):198–210, 2019.

[41] K Busch, G Von Freymann, S Linden, SF Mingaleev, L Tkeshelashvili, and M Wegener. Periodic nanostructures for photonics. *Physics reports*, 444(3-6):101–202, 2007.

[42] Viktoriia E Babicheva and Andrey B Evlyukhin. Resonant lattice kerker effect in metasurfaces with electric and magnetic optical responses. *Laser & Photonics Reviews*, 11(6):1700132, 2017.

[43] VI Zakomirnyi, AE Ershov, VS Gerasimov, SV Karpov, Hans Ågren, and IL Rasskazov. Collective lattice resonances in arrays of dielectric nanoparticles: a matter of size. *Optics letters*, 44(23):5743–5746, 2019.

[44] Yeong Hwan Ko and Robert Magnusson. Wideband dielectric metamaterial reflectors: Mie scattering or leaky bloch mode resonance? *Optica*, 5(3):289–294, 2018.

[45] Alessio Monti, Andrea Alù, Alessandro Toscano, and Filiberto Bilotti. Design of high-q passband filters implemented through multipolar all-dielectric metasurfaces. *IEEE Transactions on Antennas and Propagation*, 69(8):5142–5147, 2020.

[46] Ramón Paniagua-Domínguez, Ye Feng Yu, Andrey E Miroshnichenko, Leonid A Krivitsky, Yuan Hsing Fu, Vytautas Valuckas, Leonard Gonzaga, Yeow Teck Toh, Anthony Yew Seng Kay, Boris Luk'yanchuk, et al. Generalized brewster effect in dielectric metasurfaces. *Nature communications*, 7(1):10362, 2016.

[47] Costas M Soukoulis. *Photonic band gap materials*, volume 315. Springer Science & Business Media, 2012.

[48] Vincent Hahn, Frederik Mayer, Michael Thiel, and Martin Wegener. 3-d laser nanoprinting. *Optics and Photonics News*, 30(10):28–35, 2019.

[49] Liang Yang, Frederik Mayer, Uwe HF Bunz, Eva Blasco, and Martin Wegener. Multi-material multi-photon 3d laser micro-and nanoprinting. *Light: Advanced Manufacturing*, 2(3):296–312, 2021.

[50] Stuart L James. Metal-organic frameworks. *Chemical Society Reviews*, 32(5):276–288, 2003.

[51] Jin-Liang Zhuang, Andreas Terfort, and Christof Wöll. Formation of oriented and patterned films of metal–organic frameworks by liquid phase epitaxy: A review. *Coordination Chemistry Reviews*, 307:391–424, 2016.

[52] Lifeng Li. New formulation of the fourier modal method for crossed surface-relief gratings. *JOSA A*, 14(10):2758–2767, 1997.

[53] Jian-Ming Jin. *The finite element method in electromagnetics*. John Wiley & Sons, 2015.

[54] Allen Taflove, Susan C Hagness, and Melinda Piket-May. Computational electromagnetics: the finite-difference time-domain method. *The Electrical Engineering Handbook*, 3:629–670, 2005.

[55] Constantin R Simovski. On electromagnetic characterization and homogenization of nanostructured metamaterials. *Journal of Optics*, 13(1):013001, 2010.

[56] Philippe Lalanne and Dominique Lemercier-Lalanne. On the effective medium theory of subwavelength periodic structures. *Journal of Modern Optics*, 43(10):2063–2085, 1996.

[57] DR Smith, DC Vier, Th Koschny, and CM Soukoulis. Electromagnetic parameter retrieval from inhomogeneous metamaterials. *Physical review E*, 71(3):036617, 2005.

[58] Vladimir M Agranovich and Vitaly Ginzburg. Spatial dispersion in crystal optics. In *Crystal Optics with Spatial Dispersion, and Excitons*, pages 136–270. Springer, 1984.

[59] Christoph Menzel Dr. rer. nat. *Characterisation of optical metamaterials: effective parameters and beyond*. Phd thesis, Friedrich-Schiller-Universität Jena, 2011. Jena, Univ., Diss., 2011.

[60] Guy Bouchitté and Ben Schweizer. Homogenization of maxwell's equations in a split ring geometry. *Multiscale Modeling & Simulation*, 8(3):717–750, 2010.

[61] MW Klein, C Enkrich, M Wegener, CM Soukoulis, and S Linden. Single-slit split-ring resonators at optical frequencies: limits of size scaling. *Optics letters*, 31(9):1259–1261, 2006.

[62] WN Hardy and LA Whitehead. Split-ring resonator for use in magnetic resonance from 200–2000 mhz. *Review of Scientific Instruments*, 52(2):213–216, 1981.

[63] Y Zhou, XY Chen, YH Fu, G Vienne, AI Kuznetsov, and B Luk'Yanchuk. Fabrication of large-area 3d optical fishnet metamaterial by laser interference lithography. *Applied Physics Letters*, 103(12):123116, 2013.

[64] Ari Sihvola. *Electromagnetic Mixing Formulas and Applications*. Electromagnetic Waves. Institution of Engineering and Technology, 1999.

[65] Karim Mnasri, Fatima Z. Goffi, Michael Plum, and Carsten Rockstuhl. Homogenization of wire media with a general purpose nonlocal constitutive relation. *Journal of the Optical Society of America B*, 36(8):F99–F108, Aug 2019.

[66] Eli Yablonovitch. Photonic crystals. *Journal of Modern Optics*, 41(2):173–194, 1994.

[67] Theodosios D Karamanos, Alexandros I Dimitriadis, et al. Polarizability matrix extraction of a bianisotropic metamaterial from the scattering parameters of normally incident plane waves. *Advanced Electromagnetics*, 1(3):64–70, 2012.

[68] Y Battie, A Resano-Garcia, N Chaoui, Y Zhang, and A En Naciri. Extended maxwell-garnett-mie formulation applied to size dispersion of metallic nanoparticles embedded in host liquid matrix. *The Journal of chemical physics*, 140(4):044705, 2014.

[69] Jiangfeng Zhou, Jianfeng Dong, Bingnan Wang, Thomas Koschny, Maria Kafesaki, and Costas M Soukoulis. Negative refractive index due to chirality. *Physical Review B*, 79(12):121104, 2009.

[70] S Bassiri and CH Papas. Electromagnetic wave propagation through a dielectric–chiral interface and through a chiral slab. *JOSA A*, 5(9):1450–1459, 1988.

[71] Peter B Johnson and R-WJPrB Christy. Optical constants of the noble metals. *Physical review B*, 6(12):4370, 1972.

[72] Cheng Zhang, Nina Hong, Chengang Ji, Wenqi Zhu, Xi Chen, Amit Agrawal, Zhong Zhang, Tom E Tiwald, Stefan Schoeche, James N Hilfiker, et al. Robust extraction of hyperbolic metamaterial permittivity using total internal reflection ellipsometry. *ACS photonics*, 5(6):2234–2242, 2018.

[73] Johann Toudert. Spectroscopic ellipsometry for active nano-and meta-materials. *Nanotechnology Reviews*, 3(3):223–245, 2014.

[74] Ivan Ivanov, Mischa Bonn, Zoltán Mics, and Dmitry Turchinovich. Perspective on terahertz spectroscopy of graphene. *Europhysics Letters*, 111(6):67001, 2015.

[75] AM Nicolson and GF Ross. Measurement of the intrinsic properties of materials by time-domain techniques. *IEEE Transactions on instrumentation and measurement*, 19(4):377–382, 1970.

[76] William B Weir. Automatic measurement of complex dielectric constant and permeability at microwave frequencies. *Proceedings of the IEEE*, 62(1):33–36, 1974.

[77] DR Smith, DC Vier, Th Koschny, and CM Soukoulis. Electromagnetic parameter retrieval from inhomogeneous metamaterials. *Physical review E*, 71(3):036617, 2005.

[78] Taavi Repän, Ramakrishna Venkitakrishnan, and Carsten Rockstuhl. Artificial neural networks used to retrieve effective properties of metamaterials. *Optics Express*, 29(22):36072–36085, 2021.

[79] Siqi Huang, Zilong Cao, Helin Yang, Zhaoyang Shen, and Xiaoxia Ding. An electromagnetic parameter retrieval method based on deep learning. *Journal of Applied Physics*, 127(22):224902, 2020.

[80] Cristhianne FL Vasconcelos, Saulo L Rêgo, and Rossana MS Cruz. The use of artificial neural network in the design of metamaterials. In *Intelligent Data Engineering and Automated Learning-IDEAL 2012: 13th International Conference, Natal, Brazil, August 29-31, 2012. Proceedings 13*, pages 532–539. Springer, 2012.

[81] Dana Bishara, Yuxi Xie, Wing Kam Liu, and Shaofan Li. A state-of-the-art review on machine learning-based multiscale modeling, simulation, homogenization and design of materials. *Archives of computational methods in engineering*, 30(1):191–222, 2023.

[82] SI Maslovski, SA Tretyakov, and PA Belov. Wire media with negative effective permittivity: A quasi-static model. *Microwave and Optical Technology Letters*, 35(1):47–51, 2002.

[83] Mário G Silveirinha. Nonlocal homogenization model for a periodic array of ε-negative rods. *Physical Review E*, 73(4):046612, 2006.

[84] VM Agranovich and VE Kravtsov. Notes on crystal optics of superlattices. *Solid State Communications*, 55(1):85–90, 1985.

[85] Igor Tsukerman, ANM Shahriyar Hossain, and YD Chong. Homogenization of layered media: Intrinsic and extrinsic symmetry breaking. *Europhysics Letters*, 133(1):17003, 2021.

[86] AV Chebykin, AA Orlov, AV Vozianova, Stanislav I Maslovski, Yu S Kivshar, and Pavel A Belov. Nonlocal effective medium model for multilayered metal-dielectric metamaterials. *Physical Review B*, 84(11):115438, 2011.

[87] Tao Geng, Songlin Zhuang, Jie Gao, and Xiaodong Yang. Nonlocal effective medium approximation for metallic nanorod metamaterials. *Physical Review B*, 91(24):245128, 2015.

[88] Ricardo Marqués, Francisco Mesa, Jesus Martel, and Francisco Medina. Comparative analysis of edge-and broadside-coupled split ring resonators for metamaterial design-theory and experiments. *IEEE Transactions on antennas and propagation*, 51(10):2572–2581, 2003.

[89] S Anantha Ramakrishna. Physics of negative refractive index materials. *Reports on progress in physics*, 68(2):449, 2005.

[90] Vadim A Schotland. Homogenization of maxwell's equations in periodic composites. *Phys. Rev. E*, 85(arXiv: 1010.6246):066603, 2010.

[91] Alain Bensoussan, Jacques-Louis Lions, and George Papanicolaou. Asymptotic analysis for periodic structures, vol. 374. *American Mathematical Soc*, 81, 2011.

[92] Graeme W Milton. *The theory of composites*. SIAM, 2022.

[93] Ouail Ouchetto, C-W Qiu, Saıd Zouhdi, L-W Li, and Adel Razek. Homogenization of 3-d periodic bianisotropic metamaterials. *IEEE Transactions on Microwave Theory and Techniques*, 54(11):3893–3898, 2006.

[94] Doina Cioranescu and Jeannine Saint Jean Paulin. *Homogenization of reticulated structures*, volume 136. Springer Science & Business Media, 2012.

[95] Andrei Andryieuski, Sangwoo Ha, Andrey A Sukhorukov, Yuri S Kivshar, and Andrei V Lavrinenko. Bloch-mode analysis for retrieving effective parameters of metamaterials. *Physical Review B*, 86(3):035127, 2012.

[96] Constantin R Simovski. Bloch material parameters of magneto-dielectric metamaterials and the concept of bloch lattices. *Metamaterials*, 1(2):62–80, 2007.

[97] Andrei Andryieuski, Christoph Menzel, Carsten Rockstuhl, Radu Malureanu, Falk Lederer, and Andrei Lavrinenko. Homogenization of resonant chiral metamaterials. *Physical Review B*, 82(23):235107, 2010.

[98] David R Smith and John B Pendry. Homogenization of metamaterials by field averaging. *JOSA B*, 23(3):391–403, 2006.

[99] Mário G Silveirinha and Carlos A Fernandes. Transverse-average field approach for the characterization of thin metamaterial slabs. *Physical Review E*, 75(3):036613, 2007.

[100] MG Silveirinha, JD Baena, L Jelinek, and R Marques. Nonlocal homogenization of an array of cubic particles made of resonant rings. *Metamaterials*, 3(3-4):115–128, 2009.

[101] Andrea Alù. Restoring the physical meaning of metamaterial constitutive parameters. *Physical Review B*, 83(8):081102, 2011.

[102] Mark L Brongersma. Flat optics for dynamic wavefront manipulation. In *Metamaterials XIII*, page PC1213003. SPIE, 2022.

[103] Kunal Shastri and Francesco Monticone. Nonlocal flat optics. *Nature Photonics*, pages 1–12, 2022.

[104] Farzad Zangeneh-Nejad, Dimitrios L Sounas, Andrea Alù, and Romain Fleury. Analogue computing with metamaterials. *Nature Reviews Materials*, 6(3):207–225, 2021.

[105] Vladislav Popov, Badreddine Ratni, Shah Nawaz Burokur, and Fabrice Boust. Nonlocal reconfigurable sparse metasurface: Efficient near-field and far-field wavefront manipulations. *Advanced Optical Materials*, 9(4):2001316, 2021.

[106] Giampiero Lovat, Rodolfo Araneo, George W Hanson, and Paolo Burghignoli. Nonlocal models and effects in graphene nanointerconnects. In *2013 International Symposium on Electromagnetic Compatibility*, pages 937–942. IEEE, 2013.

[107] Satoshi Ishii and Evgenii Narimanov. Non-local optical topological transitions and critical states in electromagnetic metamaterials. *Scientific Reports*, 5(1):1–8, 2015.

[108] Vladimir M Agranovich and Yu N Gartstein. Spatial dispersion and negative refraction of light. *Physics-Uspekhi*, 49(10):1029, 2006.

[109] AI Căbuz, D Felbacq, and David Cassagne. Spatial dispersion in negative-index composite metamaterials. *Physical Review A*, 77(1):013807, 2008.

[110] Alessandro Ciattoni and Carlo Rizza. Nonlocal homogenization theory in metamaterials: Effective electromagnetic spatial dispersion and artificial chirality. *Physical Review B*, 91(18):184207, 2015.

[111] Alexander V Chebykin, Maxim A Gorlach, and Pavel A Belov. Spatial-dispersion-induced birefringence in metamaterials with cubic symmetry. *Physical Review B*, 92(4):045127, 2015.

[112] Andrii Khrabustovskyi, Karim Mnasri, Michael Plum, Christian Stohrer, and Carsten Rockstuhl. Interface conditions for a metamaterial with strong spatial dispersion. *arXiv preprint arXiv:1710.03676*, 2017.

[113] Fatima Z Goffi, Andrii Khrabustovskyi, Ramakrishna Venkitakrishnan, Carsten Rockstuhl, and Michael Plum. Higher order constitutive relations and interface conditions for metamaterials with strong spatial dispersion. *Physics Letters A*, 412:127570, 2021.

[114] David J. Griffiths. *Introduction to Electrodynamics*. Pearson, 3 edition, 1999.

[115] J. D. Jackson. *Classical Electrodynamics*. John Wiley & Sons, 3 edition, 1999.

[116] Fatima Z Goffi, Karim Mnasri, Michael Plum, Carsten Rockstuhl, and Andrii Khrabustovskyi. Towards more general constitutive relations for metamaterials: A checklist for consistent formulations. *Physical Review B*, 101(19):195411, 2020.

[117] Roger E Raab and Owen L De Lange. *Multipole theory in electromagnetism: classical, quantum, and symmetry aspects, with applications*, volume 128. OUP Oxford, 2004.

[118] Karim Mnasri. *Modeling Optical Metamaterials with Strong Spatial Dispersion*. Phd thesis, Karlsruher Institut für Technologie (KIT), 2020.

[119] Hans Bremermann. *Distributions, complex variables, and Fourier transforms*. Addison-Wesley Publishing Company, 1965.

[120] Edward J Beltrami and M Ronald Wohlers. *Distributions and the boundary values of analytic functions*. Academic Press, 2014.

[121] Peter Monk et al. *Finite element methods for Maxwell's equations*. Oxford University Press, 2003.

[122] Richard L Bishop and Samuel I Goldberg. *Tensor analysis on manifolds*. Courier Corporation, 2012.

[123] Mikhail Itskov et al. *Tensor algebra and tensor analysis for engineers*. Springer, 2007.

[124] Richard L Bishop and Richard J Crittenden. *Geometry of manifolds*. Academic press, 2011.

[125] Karim Achouri and Olivier JF Martin. Extension of lorentz reciprocity and poynting theorems for spatially dispersive media with quadrupolar responses. *Physical Review B*, 104(16):165426, 2021.

[126] Theodore Frankel. *The geometry of physics: an introduction*. Cambridge university press, 2011.

[127] Gerd Rudolph and Matthias Schmidt. *Differential geometry and mathematical physics: Part ii. fibre bundles, topology and gauge fields*. Springer, 2017.

[128] George B Arfken and Hans J Weber. Mathematical methods for physicists, 1999.

[129] Harley Flanders. *Differential forms with applications to the physical sciences*, volume 11. Courier Corporation, 1963.

[130] Pierre Comon, Gene Golub, Lek-Heng Lim, and Bernard Mourrain. Symmetric tensors and symmetric tensor rank. *SIAM Journal on Matrix Analysis and Applications*, 30(3):1254–1279, 2008.

[131] Yaroslav Shitov. A counterexample to comon's conjecture. *SIAM Journal on Applied Algebra and Geometry*, 2(3):428–443, 2018.

[132] Jerome Brachat, Pierre Comon, Bernard Mourrain, and Elias Tsigaridas. Symmetric tensor decomposition. *Linear Algebra and its Applications*, 433(11-12):1851–1872, 2010.

[133] María López Quijorna. *Symmetric Tensor Decomposition and Algorithms*. Master thesis, Universidad Complutense de Madrid, 2011.

[134] Chris Doran, Anthony Lasenby, and Joan Lasenby. *Geometric algebra for physicists*. Cambridge University Press, 2003.

[135] Marc Olive and Nicolas Auffray. Symmetry classes for even-order tensors. *Mathematics and Mechanics of Complex Systems*, 1(2):177–210, 2013.

[136] Ramakrishna Venkitakrishnan, Timon Höß, Taavi Repän, Fatima Z Goffi, Michael Plum, and Carsten Rockstuhl. Lower limits for the homogenization of periodic metamaterials made from electric dipolar scatterers. *Physical Review B*, 103(19):195425, 2021.

[137] Justyna K Gansel, Michael Thiel, Michael S Rill, Manuel Decker, Klaus Bade, Volker Saile, Georg von Freymann, Stefan Linden, and Martin Wegener. Gold helix photonic metamaterial as broadband circular polarizer. *science*, 325(5947):1513–1515, 2009.

[138] Johannes Kaschke and Martin Wegener. Gold triple-helix mid-infrared metamaterial by sted-inspired laser lithography. *Optics letters*, 40(17):3986–3989, 2015.

[139] D Bruce Burckel, Joel R Wendt, Gregory A Ten Eyck, James C Ginn, A Robert Ellis, Igal Brener, and Michael B Sinclair. Micrometer-scale cubic unit cell 3d metamaterial layers. *Advanced Materials*, 22(44):5053–5057, 2010.

[140] Karim Achouri, Ville Tiukuvaara, and Olivier JF Martin. Spatial symmetries in multipolar metasurfaces: From asymmetric angular transmittance to multipolar extrinsic chirality. *arXiv preprint arXiv:2208.12504*, 2022.

[141] Joshua Feis, Dominik Beutel, Julian Köpfler, Xavier Garcia-Santiago, Carsten Rockstuhl, Martin Wegener, and Ivan Fernandez-Corbaton. Helicity-preserving optical cavity modes for enhanced sensing of chiral molecules. *Physical review letters*, 124(3):033201, 2020.

[142] Richard JD Tilley. *Crystals and crystal structures*. John Wiley & Sons, 2020.

[143] Raymond G Ayoub. Paolo ruffini's contributions to the quintic. *Archive for history of exact sciences*, pages 253–277, 1980.

[144] Karim Mnasri, Andrii Khrabustovskyi, Christian Stohrer, Michael Plum, and Carsten Rockstuhl. Beyond local effective material properties for metamaterials. *Physical Review B*, 97(7):075439, 2018.

[145] Xavier Garcia-Santiago, Sven Burger, Carsten Rockstuhl, and Ivan Fernandez-Corbaton. Measuring the electromagnetic chirality of 2d arrays under normal illumination. *Optics letters*, 42(20):4075–4078, 2017.

[146] D Beutel, P Scott, M Wegener, C Rockstuhl, and I Fernandez-Corbaton. Enhancing the optical rotation of chiral molecules using helicity preserving all-dielectric metasurfaces. *Applied Physics Letters*, 118(22):221108, 2021.

[147] Linguo Xie, Xiaodong Qiu, Lan Luo, Xiong Liu, Zhaoxue Li, Zhiyou Zhang, Jinglei Du, and Deqiang Wang. Quantitative detection of the respective concentrations of

chiral compounds with weak measurements. *Applied Physics Letters*, 111(19):191106, 2017.

[148] Ivan Fernandez-Corbaton, Carsten Rockstuhl, Patrick Ziemke, Peter Gumbsch, Almut Albiez, Ruth Schwaiger, Tobias Frenzel, Muamer Kadic, and Martin Wegener. New twists of 3d chiral metamaterials. *Advanced Materials*, 31(26):1807742, 2019.

[149] Anatoly Serdyukov, Igor Semchenko, Sergei Tretyakov, and Ari Sihvola. *Electromagnetics of bi-anisotropic materials: Theory and applications*. Gordon and Breach Science Publishers, United States, 2001.

[150] John Lekner. Optical properties of isotropic chiral media. *Pure and Applied Optics: Journal of the European Optical Society Part A*, 5(4):417, 1996.

[151] Martin Schäferling, Daniel Dregely, Mario Hentschel, and Harald Giessen. Tailoring enhanced optical chirality: design principles for chiral plasmonic nanostructures. *Physical Review X*, 2(3):031010, 2012.

[152] Mohsen Rajaei, Jinwei Zeng, Mohammad Albooyeh, Mohammad Kamandi, Mina Hanifeh, Filippo Capolino, and H Kumar Wickramasinghe. Giant circular dichroism at visible frequencies enabled by plasmonic ramp-shaped nanostructures. *ACS Photonics*, 6(4):924–931, 2019.

[153] Euan Hendry, RV Mikhaylovskiy, LD Barron, Malcolm Kadodwala, and TJ Davis. Chiral electromagnetic fields generated by arrays of nanoslits. *Nano letters*, 12(7):3640–3644, 2012.

[154] E Plum, J Zhou, J Dong, VA Fedotov, Th Koschny, CM Soukoulis, and NI Zheludev. Metamaterial with negative index due to chirality. *Physical Review B*, 79(3):035407, 2009.

[155] Michelle L Solomon, Amr AE Saleh, Lisa V Poulikakos, John M Abendroth, Loza F Tadesse, and Jennifer A Dionne. Nanophotonic platforms for chiral sensing and separation. *Accounts of chemical research*, 53(3):588–598, 2020.

[156] Zuojia Wang, Feng Cheng, Thomas Winsor, and Yongmin Liu. Optical chiral metamaterials: a review of the fundamentals, fabrication methods and applications. *Nanotechnology*, 27(41):412001, 2016.

[157] Aso Rahimzadegan, Martin Fruhnert, Rasoul Alaee, Ivan Fernandez-Corbaton, and Carsten Rockstuhl. Optical force and torque on dipolar dual chiral particles. *Physical Review B*, 94(12):125123, 2016.

[158] Katsuya Tanaka, Aso Rahimzadegan, Dennis Arslan, Stefan Fasold, Michael Steinert, Matthias Falkner, Thomas Pertsch, Manuel Decker, Carsten Rockstuhl, and Isabelle Staude. Orientational disorder in chiral bilayer dielectric metasurfaces. In *Integrated Photonics Research, Silicon and Nanophotonics*, pages ITu2A–4. Optica Publishing Group, 2021.

[159] Nader Engheta and Dwight L Jaggard. Electromagnetic chirality and its applications. *IEEE Antennas and Propagation Society Newsletter*, 30(5):6–12, 1988.

[160] Balasubramaniam Shanker and Akhlesh Lakhtakia. Extended maxwell garnett model for chiral-in-chiral composites. *Journal of Physics D: Applied Physics*, 26(10):1746, 1993.

[161] Akhlesh Lakhtakia, Vijay K Varadan, and Vasundara V Varadan. Effective properties of a sparse random distribution of non-interacting small chiral spheres in a chiral host medium. *Journal of Physics D: Applied Physics*, 24(1):1, 1991.

[162] Sassan Bassiri. Electromagnetic waves in chiral media. *Recent Advances in Electromagnetic Theory*, pages 1–30, 1990.

[163] Ivan Fernandez-Corbaton and Gabriel Molina-Terriza. Introduction to helicity and electromagnetic duality transformations in optics. *Photonics: Scientific Foundations, Technology and Applications*, 1:341–362, 2015.

[164] Philippe G Ciarlet, Bernadette Miara, and Jean-Marie Thomas. *Introduction to numerical linear algebra and optimisation*. Cambridge university press, 1989.

[165] Rubin H Landau, Manuel J Páez, and Cristian C Bordeianu. *Computational physics: Problem solving with Python*. John Wiley & Sons, 2015.

[166] Pauli Virtanen, Ralf Gommers, Travis E. Oliphant, Matt Haberland, Tyler Reddy, David Cournapeau, Evgeni Burovski, Pearu Peterson, Warren Weckesser, Jonathan Bright, Stéfan J. van der Walt, Matthew Brett, Joshua Wilson, K. Jarrod Millman, Nikolay Mayorov, Andrew R. J. Nelson, Eric Jones, Robert Kern, Eric Larson, C J Carey, İlhan Polat, Yu Feng, Eric W. Moore, Jake VanderPlas, Denis Laxalde, Josef

Perktold, Robert Cimrman, Ian Henriksen, E. A. Quintero, Charles R. Harris, Anne M. Archibald, Antônio H. Ribeiro, Fabian Pedregosa, Paul van Mulbregt, and SciPy 1.0 Contributors. SciPy 1.0: Fundamental Algorithms for Scientific Computing in Python. *Nature Methods*, 17:261–272, 2020.

[167] James Bradbury, Roy Frostig, Peter Hawkins, Matthew James Johnson, Chris Leary, Dougal Maclaurin, George Necula, Adam Paszke, Jake VanderPlas, Skye Wanderman-Milne, and Qiao Zhang. JAX: composable transformations of Python+NumPy programs, 2018.

[168] PC Waterman. Matrix formulation of electromagnetic scattering. *Proceedings of the IEEE*, 53(8):805–812, 1965.

[169] Michael I Mishchenko, Nadezhda T Zakharova, Nikolai G Khlebtsov, Gorden Videen, and Thomas Wriedt. Comprehensive thematic t-matrix reference database: A 2015–2017 update. *Journal of Quantitative Spectroscopy and Radiative Transfer*, 202:240–246, 2017.

[170] G Gantzounis and N Stefanou. Layer-multiple-scattering method for photonic crystals of nonspherical particles. *Physical Review B*, 73(3):035115, 2006.

[171] Dominik Beutel, Achim Groner, Carsten Rockstuhl, and Ivan Fernandez-Corbaton. Efficient simulation of biperiodic, layered structures based on the t-matrix method. *JOSA B*, 38(6):1782–1791, 2021.

[172] Orval R Cruzan. Translational addition theorems for spherical vector wave functions. *Quarterly of Applied Mathematics*, 20(1):33–40, 1962.

[173] Aso Rahimzadegan, Rasoul Alaee, Carsten Rockstuhl, and Robert W Boyd. Minimalist mie coefficient model. *Optics express*, 28(11):16511–16525, 2020.

[174] Aso Rahimzadegan. *Multipolar Analysis of Ordered and Disordered Metasurfaces*. Phd thesis, Karlsruher Institut für Technologie (KIT), 2022.

[175] Andrey B Evlyukhin, Carsten Reinhardt, Urs Zywietz, and Boris N Chichkov. Collective resonances in metal nanoparticle arrays with dipole-quadrupole interactions. *Physical Review B*, 85(24):245411, 2012.

[176] Karim Mnasri, Andrii Khrabustovskyi, Michael Plum, and Carsten Rockstuhl. Retrieving effective material parameters of metamaterials characterized by nonlocal constitutive relations. *Physical Review B*, 99(3):035442, 2019.

[177] M. Goodarzi and T. Pakizeh. Retrieving effective surface susceptibilities of high-index metasurfaces based on dipole approximation. *Optics Communications*, 483:126659, 2021.

[178] S. A. Tretyakov. On the homogenization of dense planar arrays of scatterers. *Electromagnetics*, 19(2):201–210, 1999.

[179] Takashi Takeuchi and Kazuhiro Yabana. Extremely large third-order nonlinear optical effects caused by electron transport in quantum plasmonic metasurfaces with subnanometer gaps. *Scientific reports*, 10(1):1–9, 2020.

[180] Marios Mattheakis, Constantinos A Valagiannopoulos, and Efthimios Kaxiras. Epsilon-near-zero behavior from plasmonic dirac point: Theory and realization using two-dimensional materials. *Physical Review B*, 94(20):201404, 2016.

[181] Tianji Liu, Rongyang Xu, Peng Yu, Zhiming Wang, and Junichi Takahara. Multipole and multimode engineering in mie resonance-based metastructures. *Nanophotonics*, 9(5):1115–1137, 2020.

[182] Ramakrishna Venkitakrishnan, Yannick Augenstein, Benedikt Zerulla, Fatima Z Goffi, Michael Plum, and Carsten Rockstuhl. On the physical significance of non-local material parameters in optical metamaterials. *New Journal of Physics*, 25(12):123014, 2023.

[183] Aso Rahimzadegan, Theodosios D Karamanos, Rasoul Alaee, Aristeidis G Lamprianidis, Dominik Beutel, Robert W Boyd, and Carsten Rockstuhl. A comprehensive multipolar theory for periodic metasurfaces. *Advanced Optical Materials*, 10(10):2102059, 2022.

[184] C Rockstuhl, T Zentgraf, H Guo, N Liu, C Etrich, I Loa, Kl Syassen, Jürgen Kuhl, F Lederer, and H Giessen. Resonances of split-ring resonator metamaterials in the near infrared. *Applied Physics B*, 84(1):219–227, 2006.

[185] Stefan Linden, Christian Enkrich, Martin Wegener, Jiangfeng Zhou, Thomas Koschny, and Costas M Soukoulis. Magnetic response of metamaterials at 100 terahertz. *Science*, 306(5700):1351–1353, 2004.

[186] Nguyen Thanh Tung, YoungPak Lee, and Vu Dinh Lam. Transmission properties of electromagnetic metamaterials: From split-ring resonator to fishnet structure. *Optical review*, 16(6):578–582, 2009.

[187] Antoine Wegrowski, Wei-Chih Wang, Chileung Tsui, and Prabir Garu. Negative refractive index modified fishnet enhancement by wire shift. *Materials Research Express*, 2022.

[188] Patrick Grahn, Andriy Shevchenko, and Matti Kaivola. Electromagnetic multipole theory for optical nanomaterials. *New Journal of Physics*, 14(9):093033, 2012.

[189] Viktoriia E Babicheva and Andrey B Evlyukhin. Analytical model of resonant electromagnetic dipole-quadrupole coupling in nanoparticle arrays. *Physical Review B*, 99(19):195444, 2019.

[190] E. Prodan and P. Nordlander. Plasmon hybridization in spherical nanoparticles. *The Journal of Chemical Physics*, 120(11):5444–5454, 2004.

[191] P. Nordlander, C. Oubre, E. Prodan, K. Li, and M. I. Stockman. Plasmon hybridization in nanoparticle dimers. *Nano Letters*, 4(5):899–903, 05 2004.

[192] M. Quinten, A. Leitner, J. R. Krenn, and F. R. Aussenegg. Electromagnetic energy transport via linear chains of silver nanoparticles. *Opt. Lett.*, 23(17):1331–1333, Sep 1998.

[193] Stefan A. Maier, Mark L. Brongersma, Pieter G. Kik, and Harry A. Atwater. Observation of near-field coupling in metal nanoparticle chains using far-field polarization spectroscopy. *Phys. Rev. B*, 65:193408, May 2002.

[194] Benedikt Zerulla, Ramakrishna Venkitakrishnan, Dominik Beutel, Marjan Krstić, Christof Holzer, Carsten Rockstuhl, and Ivan Fernandez-Corbaton. At-matrix based approach to homogenize artificial materials. *Advanced Optical Materials*, page 2201564, 2022.

[195] Dominik Beutel, Ivan Fernandez-Corbaton, and Carsten Rockstuhl. Unified lattice sums accommodating multiple sublattices for solutions of the helmholtz equation in two and three dimensions. *Physical Review A*, 107(1):013508, 2023.

[196] Martin Fruhnert, Ivan Fernandez-Corbaton, Vassilios Yannopapas, and Carsten Rockstuhl. Computing the t-matrix of a scattering object with multiple plane wave illuminations. *Beilstein journal of nanotechnology*, 8(1):614–626, 2017.

[197] A Semechko. Suite of functions to perform uniform sampling of a sphere. *MATLAB File Exchange Server*, 2015.

[198] Ari H Sihvola and Ismo V Lindell. Analysis on chiral mixtures. *Journal of electromagnetic waves and applications*, 6(5-6):553–572, 1992.

[199] Akira Ishimaru, Seung-Woo Lee, Yasuo Kuga, and Vikram Jandhyala. Generalized constitutive relations for metamaterials based on the quasi-static lorentz theory. *IEEE Transactions on Antennas and Propagation*, 51(10):2550–2557, 2003.

[200] C Rockstuhl and T Scharf. A metamaterial based on coupled metallic nanoparticles and its band-gap property. *Journal of microscopy*, 229(2):281–286, 2008.

[201] Ivan Fernandez-Corbaton. Helicity and duality symmetry in light matter interactions: Theory and applications. In *Laser Science*, pages LM1H–2. Optica Publishing Group, 2015.

[202] D Schebarchov, EC Le Ru, Johan Grand, and Baptiste Auguié. Mind the gap: testing the rayleigh hypothesis in t-matrix calculations with adjacent spheroids. *Optics express*, 27(24):35750–35760, 2019.

[203] Amos Egel, Lorenzo Pattelli, Giacomo Mazzamuto, Diederik S Wiersma, and Uli Lemmer. Celes: Cuda-accelerated simulation of electromagnetic scattering by large ensembles of spheres. *Journal of Quantitative Spectroscopy and Radiative Transfer*, 199:103–110, 2017.

[204] BC Hall. Lie groups, lie algebras, and representations: An element introduction. *Graduate Texts in Mathematics*, 222:351, 2015.

[205] Loring W Tu. Manifolds. In *An Introduction to Manifolds*, pages 47–83. Springer, 2011.

[206] Ivan Fernandez Corbaton. *Helicity and duality symmetry in light matter interactions: Theory and applications*. Phd thesis, Macquarie University, 2014.

[207] Ivan Fernandez-Corbaton, Dominik Beutel, Carsten Rockstuhl, Ansgar Pausch, and Wim Klopper. Computation of electromagnetic properties of molecular ensembles. *ChemPhysChem*, 21(9):878–887, 2020.

[208] Reto Giannini, Christian V Hafner, and Jörg F Löffler. Scaling behavior of individual nanoparticle plasmon resonances. *The Journal of Physical Chemistry C*, 119(11):6138–6147, 2015.

[209] Amikam Aharoni. Demagnetizing factors for rectangular ferromagnetic prisms. *Journal of applied physics*, 83(6):3432–3434, 1998.

Acknowledgement

I would like to express my deepest gratitude to the following individuals and organizations who have supported me throughout my doctoral journey.

First and foremost, I would like to thank my parents, Venkitakrishnan.K.V (Father) and R.Bagirathi (Mother) for their unwavering love, support, and encouragement. Without their constant guidance and belief in my abilities, I would not have been able to complete this journey. I would also like to thank my brother, Viswanath V, my in-law Anupama Aravind and my nephew kairav Sanvi for their constant support and love during my doctoral journey.

I am also grateful to my beloved wife, Shrinidhi Raman for her patience, understanding, and support during this challenging period. Her love and encouragement have been my anchor, and I am forever grateful for her unwavering support. I also would like to extend my love to my in-law family, Raman P.R (father-in-law), Dhanam N.P(mother-in-law), and Sreeram Raman (brother-in-law) for fully trusting me and encouraging me throughout my doctoral journey.

I extend my sincere appreciation to my supervisor, Prof. Dr. Carsten Rockstuhl for his invaluable guidance, insights, and expertise. His patience, support, and encouragement have been instrumental in shaping my research and academic pursuits. I cannot express my gratitude to you adequately with words.

I would also like to thank my co-supervisor Prof. Dr. Michael Plum for his guidance throughout the mathematical topics and for the fruitful collaboration. I really appreciate that I had the opportunity to work with you.

I would also like to extend my deepest gratitude to my collaborator, Dr. Fatima Z. Goffi, from the Department of Mathematics. Her mathematical rigor and expertise have been invaluable to the completion of this work. I am also grateful for her generous support in

answering my numerous mathematical queries, as well as proofreading my mathematical chapters.

Furthermore, I would like to thank the Collaborative Research Center (CRC) 1173 "Wave phenomena: analysis and numerics" for hiring me and funding my doctoral research. The opportunities and resources provided by the CRC have been essential in the successful completion of my research, and I am grateful for their support. I also thank my colleagues at CRC 1173 for the great discussions during the annual meetings and during the iRTG seminars.

In addition, I would like to thank the "Institute of theoretical solid-state physics (TFP)" for providing me with a beautiful office space during my time at KIT.

Finally, I would like to thank all my friends and colleagues who have provided me with their support and encouragement during this journey. Specifically, I would like to thank, Dr. Ivan Fernandez-Corbaton, Dr. Xavier Garcia-Santiago, Prewrak Dhawan, Yannick Augenstein, Benedikt Zerulla, Maxim Vavilin, Aristeidis Lamprianidis, Maria Paszkiewicz, Dominik Beutel and Lukas Rebholz for all the lively scientific exchange. Your constant support and belief in my abilities have been a source of motivation and inspiration.

Thank you all for being an integral part of my journey.